UNIVERSITY OF TWENTE.

Faculty of Electrical Engineering, Mathematics & Computer Science

Impedimetric analysis of the activity of single fluid cracking catalyst particles

Jordi M. Hendrix

M.Sc. Thesis
24 August 2018

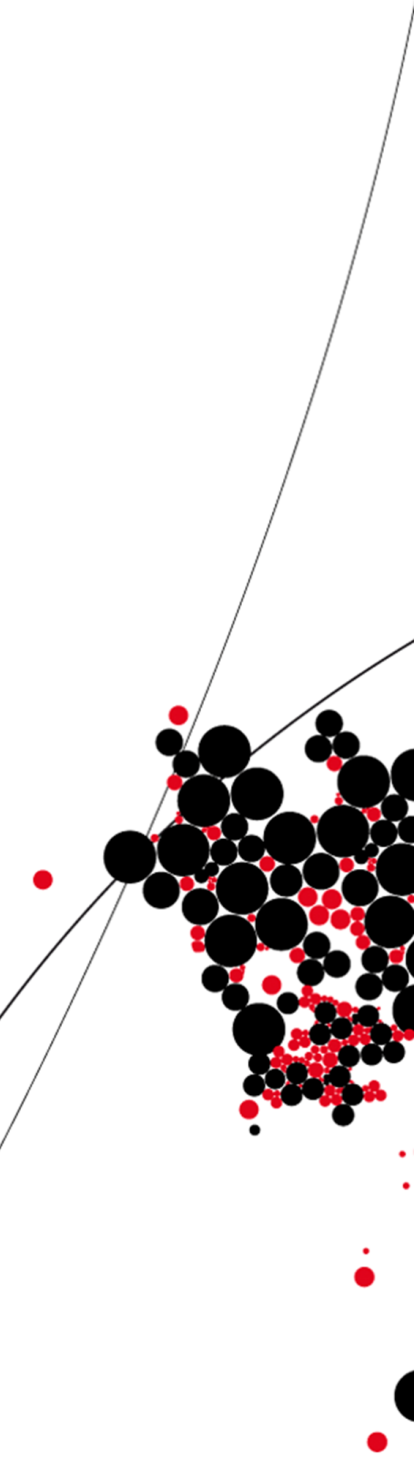

Supervisors:
dr.ir. W. Olthuis
M. Solsona, MSc.
prof.dr.ir. L. Abelmann

BIOS Group
Faculty of Electrical Engineering,
Mathematics and Computer Science
University of Twente
P.O. Box 217
7500 AE Enschede
The Netherlands

Summary

Fluid catalyst cracking (FCC) particles are crucial for the transformation of crude oil into usable products. The particle acts as catalyst to convert large hydrocarbon chains into, for instance, gasoline. During the cracking process, FCC particles become deactivated due to the accumulation of material. This causes a reduced efficiency of the cracking process. In the current cracking process, it is not possible to selectively remove the deactivated particles. The possibility to detect FCC particle activity, by using the electrical impedance, was investigated in this thesis. Literature indicates a relation between the activity of FCC particles and the amount of metal that has been accumulated on the particle. Several models were made to relate this change in metal accumulation to a measurable impedance of a microfluidic sensor. These models show that it is most favourable to measure the high frequency capacitance of the particles, while using anisole as medium. The expected change in capacitance of this system was modelled to be between 7 and 12aF. To measure this change in capacitance, a lock-in architecture was designed with a noise level of 6.3aF. The system was tested, while using anisole as medium, by measuring both air bubbles and polystyrene particles. This resulted in expected system behaviour. During the final experiments, two categories of particles where measured: fresh and deactivated FCC particles. During these measurements, around 40 particles of each group where measured and video analysis was used to estimate the size of the particles. The experimental results were fitted into a cube function with respect to the particle radius. The experiments showed that impedance variations of FCC particles of the same category are more significant than impedance changes due to metal accumulation. Nevertheless, a correlation exists between the activity of a particle and the average impedance. For a particle with a radius of 40 micron, the experimental results showed an average difference in impedance between fresh and deactivated particles of 20.5F, which closely resembles the model results. Although more particles should be measured to verify this difference, the average impedance of Fluid cracking catalyst (FCC) could potentially be used to identify groups of reduced activity.

Contents

List of acronyms

FCC	Fluid cracking catalyst
Fe	Iron
Ni	Nickel
V	Vanadium
LML	low metal loading
MML	medium metal loading
HML	high metal loading
DC	direct current
AC	alternating current
SiO2	Silicon dioxide

Chapter 1

Introduction

FCC particles are used in 40-45% of the gasoline production in the world [1]. The particles are used as a catalyst to cut long chain hydrocarbons into smaller molecules which can then be used in the production of fuels and chemicals. A schematic description of the cracking process is shown in Fig. 1.1. The cracking of oil is an endothermic reaction which takes place in a reactor by using the catalytic properties of FCC particles. When being used, the FCC particles become deactivated due to the accumulation of several metals (Iron (Fe), Nickel (Ni) and Vanadium (V)) and/or coke, mainly on the particle surface [2]–[5]. The accumulated coke is removed by thermal regeneration, after which the FCC particles return into the cracking process. However, the accumulated metals can not be removed, causing deactivation of the particles over time. This deactivation will decrease the efficiency of the gasoline production process and requires the FCC particles to be continuously replaced for fresh ones. An estimated 2.3 million kilogram of particles are used each day [6].

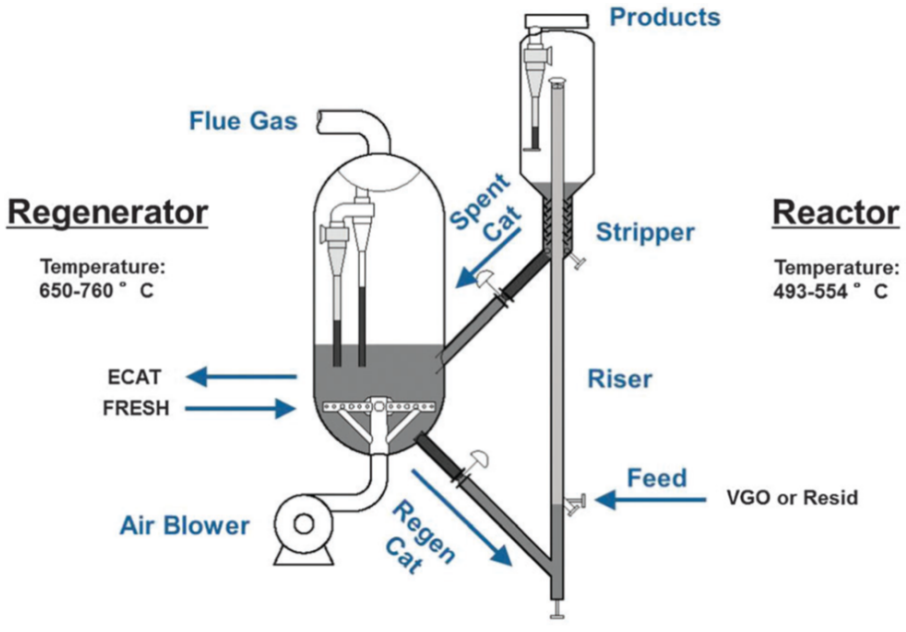

Fig. 1.1: Process flow of oil cracking using FCC particles [6].

In the current cracking process, it is not possible to selectively remove the deactivated catalyst particles. Instead a small percentage of the total FCC particles is removed and replaced with fresh ones at specific intervals. Therefore, some particles that are removed will still be active, while other particles that are deactivated will remain in the process. This will reduce the efficiency of the FCC cracking process and creates an unnecessary waste of usable FCC particles. A method to continuously detect the activity of FCC particles would give rise to the possibility to selectively remove the deactivated FCC particles, reducing these negative effects.

Several methods to detect the activity of FCC particles has been recorded in literature. Meier et al., uses the skeletal density to measure the activity [1]. The density of the particles slowly increase during the cracking process due to the accumulation of material. As the accumulated material causes deactivation of the particle, the density gives an indication for the activity of the particle. The increase in density can be detected by the sink-float density separation method. The limitation of this method is that it cannot be used continuously to separate the FCC particles. Furthermore, this method detects accumulation of any particles and not specifically the accumulation of the materials which causes particle deactivation.

Another method to separate the FCC particles with a difference in activity is based on the magnetic properties, as done by Solsona et al. [7]. The accumulation of iron on the particle, which is partly responsible for the deactivation, makes the particle magnetic. The deactivated particles can thus be separated with the use of magnetic forces. A limitation of this technique is that only the iron accumulation is detected, while this is not the only element responsible for deactivation of FCC particles.

In this thesis, it is determined whether it is possible to detect the activity of FCC particles by using the electrical properties of the particle. An advantage of this technique is that the detection is not limited to one specific metal, like the technique of Solsona [7]. The technique is sensitive to any accumulation in material and not just the activity-reducing elements. However, unlike in the technique of Meier, the sensitivity is dependent on the element. This allows a design were the activity-reducing metals are detected with highest sensitivity [1]. In this research, the following question is answered: *"Can the metal accumulation of fluid catalyst cracking particles during crude oil processes be detected by measuring the particle impedance?"*

The thesis starts with the theory and modelling in Chap. 2 used to characterize the FCC particles. This will result in an expected value for the change in impedance, which will be the basis for the design choices that are made in Chap. 3. Here the design of all the individual system elements is explained. In Chap. 4, a description is given of the materials that are used and a plan of action is presented. Chap. 5 discusses the results of the performed experiments. Finally, Chap. 6 draws conclusions from the results and Chap. 7 gives some recommendations for future research.

Chapter 2

Theory & modelling

In this chapter, the theory and models that are used to describe the designed system are explained. The chapter starts with some basic information about the measurement principle which is used. This includes a description of the detection methods which are used in literature. Hereafter, the relevant information about the FCC particles will be given. Next, the electrical models used to characterize the system will be explained in detail. The results of these models are used in the design of both the microfluidic chip and the measurement circuit which are used in experiments. Finally some information is given about the microfluidics as used in the system.

2.1 Basic measurement principle

The goal of this research is to detect the activity of FCC particles by using the electrical impedance. The impedance of a system is a measure for the ratio between the applied voltage and the current flowing through this conductor. To measure the impedance of FCC particles, two electrodes are used. When the particle is present between the electrodes, the measured impedance will partly be determined by the electrical properties of the particle. The measurement will be performed in a microfluidic chip, where the FCC particles will one by one pass the electrodes by flowing along with the fluid. A simplified schematic of the measurement design is shown in Fig. 2.1.

2.1.1 Impedance elements

The impedance of the system can be subdivided into three basic circuit elements: the resistance, the inductance and the capacitance. When using constant non-changing voltages (direct current (DC)), the impedance of a conductor is completely determined by the resistance. However, when using alternating current (AC) voltages, also the capacitance and inductance are included in the impedance.

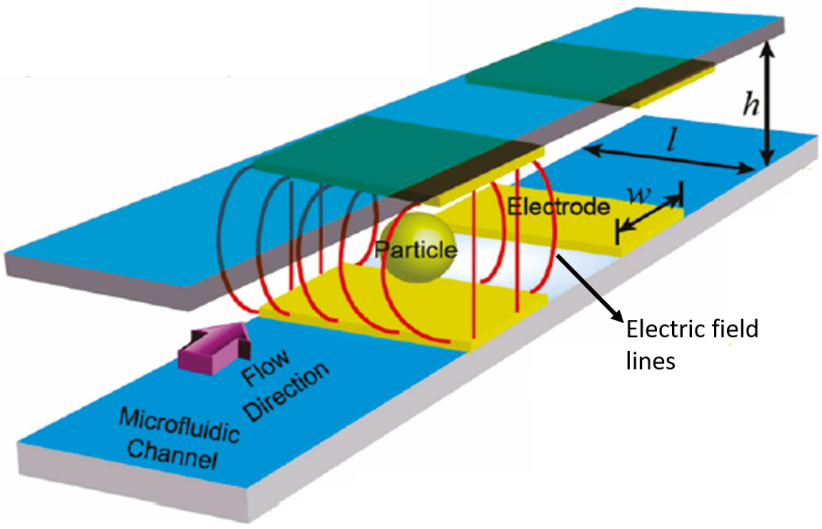

Fig. 2.1: Simplified schematic of the chip design that is used to measure the impedance of FCC particles, modified from [8]

Resistance

The resistance describes how well an element resists the flow of current through this material. For the system of Fig. 2.1, the resistance is determined by both the fluid and FCC particle, which are located in-between the electrodes. During experiments, the choice of liquid is thus important. The fluid resistivity, which is the resistance per unit length, is one of the properties, which determines the liquid choice. The resistance of an element can be determined from the resistivity by:

$$R = \frac{\rho d}{A}, \tag{2.1}$$

where R represents the resistance [Ω], ρ the resistivity [Ωm], d the distance between the electrodes [m] and A the area of the electrodes [m^2].

Inductance

An inductor is an electrical element which is able to store energy in a magnetic field. As a result of a flowing current, a magnetic field is generated. Energy is required to change the strength of the stored magnetic field. An inductive element thus resists the change in magnetic field and therefore a change in current through a material. Inductance is mainly visible in very long wound wires, such as coils. As these wires are not present in the system of Fig. 2.1, the inductance becomes negligible.

Capacitance

A capacitor is an element which can store energy in the form of electrical charge. A typical capacitor consists of a set of conductors separated by a non-conducting

dielectric material. Whenever a voltage difference is applied to the electrodes, charge accumulates on sides of the electrodes. This charge is equal in magnitude on both sides, but is positive on one electrode and negative on the other. For the device of Fig. 2.1, the capacitance dominates the system impedance, whenever the resistance of the fluid and particle is sufficiently large. The capacitance itself depends on the dimensions of the device, in combination with the dielectric properties of both the fluid and the particles:

$$C = \frac{\epsilon_0 \epsilon_r A}{d}, \tag{2.2}$$

where C represents the capacitance [F], ϵ_0 the vacuum permittivity [F/m], ϵ_r the dielectric constant [], A the area of the electrode plates [m^2] and d the distance between the electrodes [m]. The dielectric constant of the fluid is another important property on which the fluid choice is based upon.

2.1.2 Impedance detection in literature

There are several methods which can be used to detect the impedance of a system. As will be shown, small differences in particle electrical properties have to be detected, very sensitive measurements principles are required. Some common detection techniques used in literature are shortly described here.

Resonating circuit

Resonating circuits are based on the series or parallel combination of a capacitor and a inductor as shown in Fig. 2.2 [9]. The impedance of a capacitor and a inductor are as follows:

$$Z_C = -\frac{j}{\omega C} \tag{2.3}$$

$$Z_I = j\omega L, \tag{2.4}$$

where Z indicates the impedance, C the capacitance [F] and L the inductance [H], ω the angular frequency [rad/s] and j the imaginary unit. At the specific angular frequency as shown in Eq. 2.5, both impedances are exactly equal in magnitude but one is positive, while the other is negative. At this frequency, the impedance of a resonance circuit shows a large peak which is relatively easy to detect. In resonating sensing circuits, the capacitor is the sensor with a variable capacitance. The change in capacitance will cause a changing resonance frequency which is detected.

$$\omega = \frac{1}{\sqrt{LC}} \tag{2.5}$$

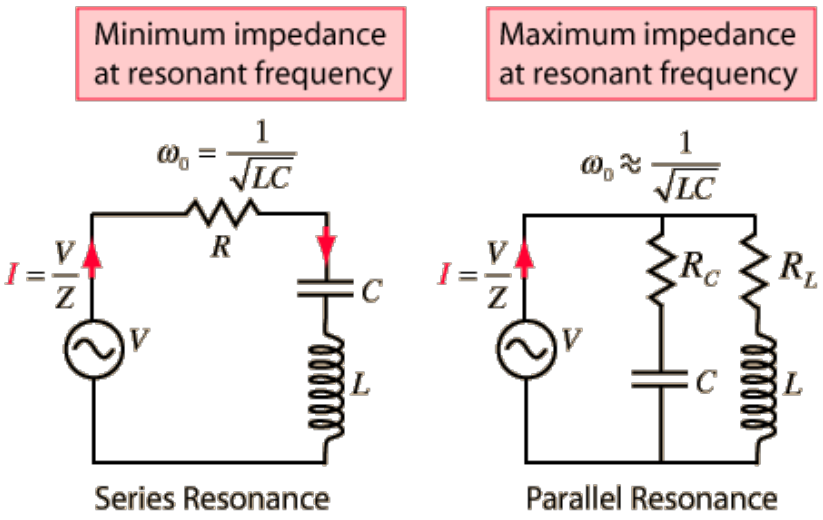

Fig. 2.2: Example of resonance circuits, showing series and parallel resonance [10].

An example of a resonance circuit used in detecting the capacitance of a sensor is shown in Ferrier et al. [11]. By using a cavity resonator, a resolution of 2aF is reached, while detecting yeast cells and polystyrene beads in a microfluidic chip. Another example is the research of Tapson et al., where a resolution of 11aF is reached while detecting the movement of piezoelectric actuators [12].

Lock-in architecture

Another method to accurately measure the impedance of a system is to use a lock-in amplifier. This device is able to detect very small AC signals, even when the noise that is present, is several orders of magnitude higher than this signal. [13] This is possible since a lock-in amplifier is able to measure at a very narrow frequency bandwidth, which can be determined by the user. The basic building blocks of a lock-in amplifier are shown in Fig. 2.3.

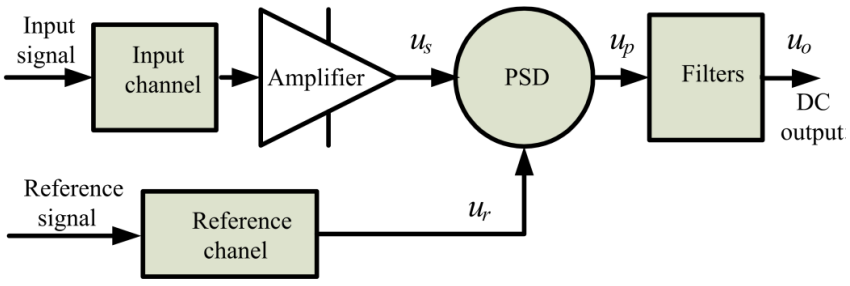

Fig. 2.3: Block diagram showing the basic elements of a lock-in amplifier [14].

The input signal of the lock-in amplifier, as identified in this figure, should be dependent on the impedance which is detected. After amplification, this signal is multiplied with a reference signal, which has a predetermined frequency. The basic working

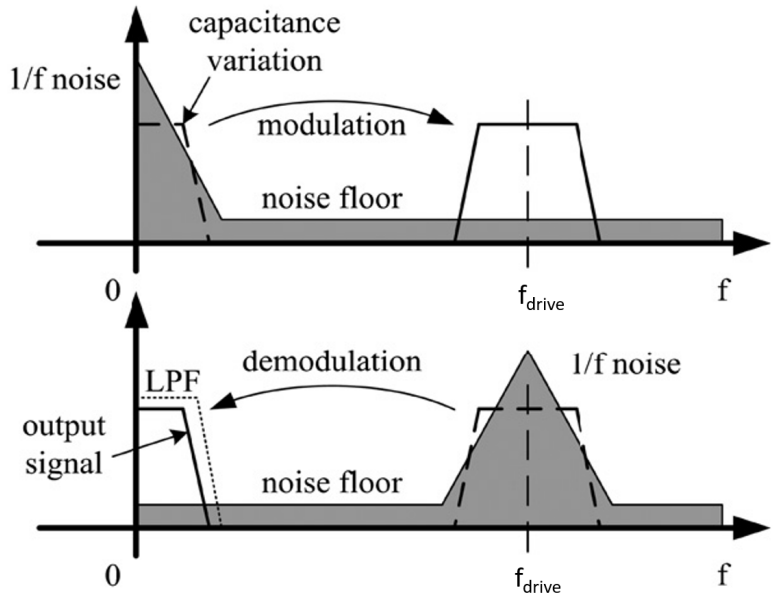

Fig. 2.4: Principle of noise reduction of a lock-in amplifier, modified from [19]

principle of a lock-in amplifier is based on multiplication of two sinusoidal functions. Whenever two sinusoidal signals are multiplied, the result is as shown in Eq. 2.6.

$$Asin(2\pi\omega_1 t) \cdot Bsin(2\pi\omega_2 t) = \frac{1}{2}AB\Big(cos(2\pi t(\omega_1 - \omega_2)) - cos(2\pi t(\omega_1 + \omega_2))\Big) \quad (2.6)$$

Where ω_1 and ω_2 are the frequencies of the two signals in [rad/s]. Whenever the reference frequency is chosen such that frequencies ω_1 and ω_2 are exactly equal, the result of the multiplication is a combination of a DC signal and a signal with twice the frequency. After using a simple low-pass filter, only the DC element will remain. The noise which is present, is a combination of 1/f noise and white noise and will therefore mostly be present at low-frequencies [15]–[18]. This noise is also multiplied with the reference signal, which will not result in a DC signal for all frequencies which are not exactly equal to the reference signal. After low-pass filtering most noise will therefore be removed. Only the noise, which has a frequency very close to the reference signal will thus remain. This principle is shown in Fig. 2.4

Wei et al. uses a lock-in architecture to measure the capacitance of a MEMS suspended blade in-between a set of electrodes [19]. This system is capable of detecting changes in capacitance for a capacitance of 1.2fF, with a resolution of 1aF for using a bandwidth of 100Hz.

Bride circuits

Another common method for the detection of impedances is by using a bridge circuit. The working principle of a bridge circuit is based on null detection. There are several

bridge configurations possible, depending on the measurement requirements. The simplest bridge circuit is the Wheatstone bridge as shown in Fig. 2.5.

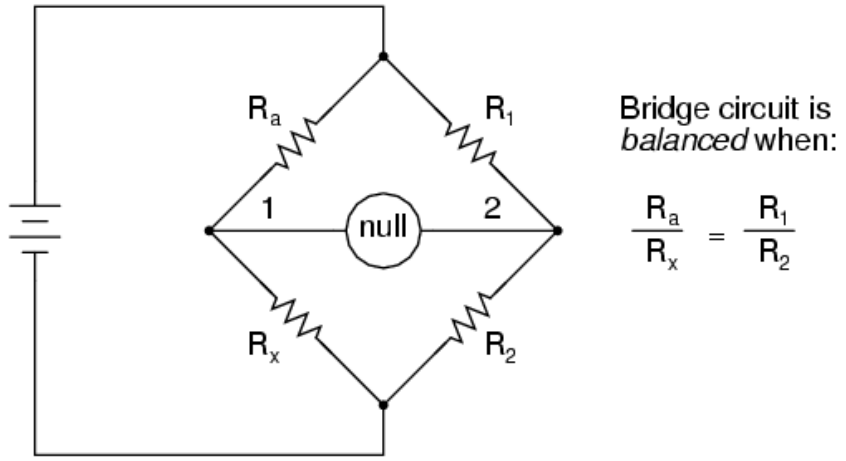

Fig. 2.5: Circuit diagram of a Wheatstone bridge [20].

In this circuit R_x can be the sensor, for which the resistance is dependent on the measurement. Furthermore, R_a is an internal variable resistor of the bridge circuit. In this bridge circuit, the null detector checks whether the potential at both branches of the bridge are exactly equal. In that case the bridge is so-called balanced and the value of the unknown resistor R_x can be expressed as a function of the other, known, resistors R_a, R_1 and R_2. When the resistance of R_x changes, the bridge becomes unbalanced, which is detected by the null detector. The bridge circuit will then change the resistance value of R_a, until the bridge is balanced once again. Whenever balanced, the unknown resistor value can be calculated once again.

Besides the Wheatstone bridge as shown in Fig. 2.5, which is used for resistor calculations, also other bridge configurations are available. For instance, the Schering bridge can be used to measure capacitance values.

The disadvantage of using bridge circuits, is that the system is optimized for null detection, which requires constant calibration of some internal resistors and capacitors, which limits the measurement speed. For the AH2700A Ultra-precision 50Hz-20kHz Capacitance bridge, the resolution is about 0.5aF [21]. However, about 0.4 seconds is required for full precision measurements. This relatively low speed can thus be a problem for continuous flow measurements.

Opacity

The opacity can be used to compensate for the size of particles. This should be used in combination with a technique that is able to measure on two frequencies simultaneously, like the lock-in architecture. Since particles will show a differentiation in size, the measured impedance of the electrodes will likely be influenced by this size

differentiation. The opacity is defined as the ratio between high frequency and low frequency impedance and as found in Gawad et al. this opacity can largely compensate for size differences [22]. The low frequency impedance, which is the resistance will give the information about the particle size, which can be used in the high frequency measurement to allow for size compensation.

2.1.3 Unwanted effects

There are two important effects, which will limit the accuracy of any capacitive measurement system: parasitic capacitance and noise. The effect of these unwanted effects should be limited.

Parasitic capacitance

The parasitic capacitance of the sensor is the unwanted additional capacitance due to electric field lines outside the sensing area. The equation for a capacitor, as shown in Eq. 2.2, is a simplification of the real capacitance and does not include these fringing effects. When the separation of the electrodes is in the same range as the electrode dimensions, the total capacitance can be around 10 times the theoretical capacitance [23]. Parasitic effects can be reduced by shielding the electrodes [24].

Noise

Noise reduction is crucial when measuring small signals. To be able to measure a relevant signal, this signal should not be completely overshadowed by the present noise.

Noise in resistors and capacitors consists of Johnson-Nyquist noise due thermal fluctuations and 1/f noise which has a variety of causes [15]–[18]. As the 1/f noise decreases with frequency, this noise can be avoided by performing measurements at a high frequency. Johnson-Nyquist noise can however not be completely avoided and will thus always limit the accuracy of a measurement. For a resistor, the Johnson-Nyquist noise is:

$$i_n = \sqrt{4k_b T \Delta f R}, \tag{2.7}$$

where i_n is the root mean square of the current [A], k_b is the Boltzmann constant [J/K], T is the temperature [K], R is the resistance [Ω] and Δf is the frequency bandwidth that is used [Hz] [25]. The noise source will act as current noise source which is in parallel with the wanted resistor. When applying a voltage V_{in} to this noisy resistor, the noise current will cause a uncertainty in the measured resistance of:

$$R_n = \frac{V_{in}}{i_r + i_n} - R, \tag{2.8}$$

where R_n is the uncertainty in measured resistance [Ω] and i_r is the current of noiseless resistor with the fixed resistance of R to which a potential V_{in} is applied [A]. The Johnson-Nyquist noise on a capacitor can be described by:

$$Q_n = \sqrt{k_b T C_{meas} \Delta f}, \tag{2.9}$$

where Q_n is the fluctuations in charge due to Johnson-Nyquist noise [C] and C_{meas} is the measured capacitance [F] [26]. From the fluctuations in charge on the capacitor, the change in capacitance can be determined by:

$$C_n = \frac{Q_n}{V_{cap}}, \tag{2.10}$$

where C_n is the capacitance fluctuation due to noise and V_{cap} is the voltage applied to the capacitor. The capacitance noise can be reduced by minimizing the total capacitance, which can be done by avoiding parasitic capacitance. Furthermore, the frequency bandwidth can be reduced and the applied voltage can be increased.

2.2 Particle information

Little is known about the electrical properties of FCC particles, which complicates the modelling process. In order to model the electrical properties of these particles, the information about the composition is used, which is provided by the particle supplier. This information is listed in Tab. 2.1.

Tab. 2.1: Mass percentage of the content of FCC particles as provided by the supplier

Component	SiO_2	Al_2O_3	MgO	TiO_2	Fe_2O_3	P_2O_5	CeO_2
Mass percentage (%)	56.855	40.354	1.96	1.627	0.93	0.343	0.285

Na	V_2O_5	CaO	NiO	K	ZnO	Cu
0.207	0.141	0.132	0.126	0.064	0.06	0.005

In the given information, the total mass percentage obtained by adding all the individual values is larger than 100%. It is unknown why this is the case, but to compensate all the percentages are scaled down.

Another important piece of information used as a starting point, is the change in composition due to the accumulation of material. This composition is obtained by density sorting the FCC particles into 4 categories: fresh, low metal loading (LML), medium metal loading (MML) and high metal loading (HML). For each of these groups, the composition of the molecules responsible for particle deactivation is determined and shown in Tab. 2.2. The table shows that for fresh particles Ni and V are absent, while Fe is already present.

Tab. 2.2: Change in the mass percentages of the molecules responsible for FCC particle deactivation [1].

	Mass percentage (%)			
Molecule	Fresh	LML	MML	HML
Fe_2O_3	0.34	0.79	0.93	0.96
NiO	0.00	0.33	0.49	0.59
V_2O_5	0.00	0.53	0.66	0.74

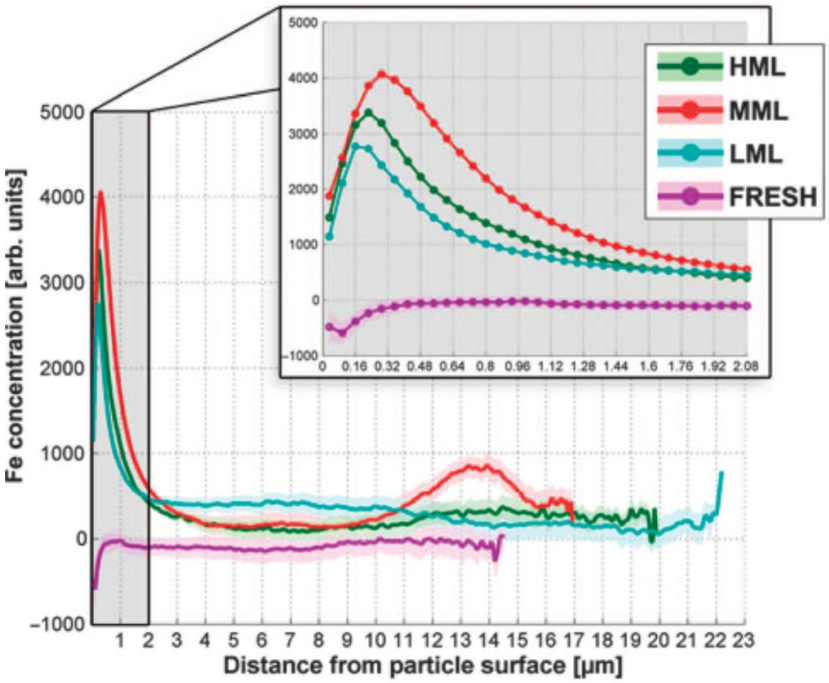

Fig. 2.6: The concentration of iron close to the particle surface for different stages of metal accumulation (adapted from [1]).

Meirer et al. shows that the accumulation of some of the activity-reducing metals, is mainly occurring in the outer layer of the FCC particle [1]. Furthermore, this research shows that the reduction in the activity of FCC particles is mostly caused by the accumulation of metals on this outer layer. For iron, this accumulation is shown in Fig. 2.6. A similar concentration distribution is visible for nickel [1]. For vanadium the information about the concentration distribution is not available and it is assumed that this element is distributed equally over the particle.

In order to model the electrical behaviour of the FCC particle, some important molecule properties are required. The dielectric constant, resistivity and density of the relevant molecules are listed in Tab. 2.3. For difosforpentoxide, the values of the resistivity and dielectric constant are not available. For sodium and potassium, the form in which these elements are present is unknown. Therefore, the dielectric constant and resistivity are also not known. Furthermore, the percentage of copper is negligible. These elements are therefore not included in the table.

Tab. 2.3: Important properties of the FCC content.

Component	Dielectric constant	Resistivity ($\Omega \cdot$ m)	Density (kg/m^3)
SiO_2	3.9 [27]	10^{12} [28]	2650 [27]
Al_2O_3	9.9 [29]	10^{12} [29]	3960 [29]
MgO	9.96 [30]	10^{12} [31]	3580 [31]
TiO_2	63.7 [32]	10^{10} [33]	4230 [33]
Fe_2O_3	20.6 [34]	$2.5 \cdot 10^3$ [35]	5260 [36]
CeO_2	23 [37]	$3.1 \cdot 10^5$ [38]	7110 [39]
V_2O_5	25 [40]	10^2 [40]	3357 [41]
CaO	12.01 [42]	$5 \cdot 10^6$ [43]	3340 [44]
NiO	11.9 [45]	$1.05 \cdot 10^5$ [45]	6800 [45]
ZnO	8.5 [46]	$7.5 \cdot 10^5$ [47]	5660 [46]

Tab. 2.4: The amount of volume occupied by the medium due to the porosity of the FCC particle [1].

	Fresh	LML	MML	HML
Micropore volume (cm^3/g)	0.0605	0.0243	0.0163	0.0140
Skeletal density (g/cm^3)	2.785	2.946	2.953	2.957
Micropore volume fraction (%)	16.85	7.159	4.813	4.140

Because the FCC particle is porous, some volume of the particle will be filled with medium. The amount of porous volume is different in each stage and is calculated by using the micropore volume, in combination with the skeletal density, as found by Meirer [1]. These values are summarized in Tab. 2.4.

Combining the information from Tab. 2.1 until Tab. 2.4, makes it possible to calculate the volume percentages of each element in each accumulation stage. In this calculation, difosforpentoxide, sodium and potassium are left out, due to the lack of knowledge of the electrical properties. These volume percentages are shown in Tab. 2.5.

2.3 Electrical analysis of electrode-particle system

The goal of the research as done in this thesis, is to measure the difference in impedance between particles that are fresh and particles that have accumulated some metal. In order to estimate how large this change in impedance is expected to be, some modelling is done. The models can then be used in the design of the experimental set-up. In this section, at first the theory behind some different models is explained. Hereafter, the results of modelling are shown and finally these results are interpreted in order to optimize the measurements that are performed.

Tab. 2.5: Volume percentage of each stage and layer of the FCC particle.

	Volume percentage (%)						
	Fresh	LML		MML		HML	
Element	Inner/outer	Inner	Outer	Inner	Outer	Inner	Outer
SiO_2	54.50	60.56	58.51	62.02	59.17	62.41	59.25
Al_2O_3	25.88	28.76	27.79	29.46	28.10	29.64	28.14
MgO	1.39	1.54	1.49	1.58	1.51	1.59	1.51
TiO_2	0.98	1.09	1.05	1.11	1.06	1.12	1.06
CeO_2	0.10	0.11	0.11	0.11	0.11	0.12	0.12
CaO	0.10	0.11	0.11	0.11	0.10	0.12	0.11
ZnO	0.03	0.03	0.03	0.03	0.03	0.03	0.03
Fe_2O_3	0.17	0.19	2.18	0.19	2.84	0.19	2.97
NiO	0.00	0.00	1.14	0.00	1.71	0.00	2.07
V_2O_5	0.00	0.45	0.43	0.57	0.54	0.64	0.61
Medium	16.85	7.159	7.159	4.813	4.813	4.140	4.140

2.3.1 Model building

Several models are designed in order to estimate the impedance of FCC particles. An overview of the models that are used, is given in Fig. 2.7. This figure shows the inputs and outputs of each of the models. The 2D electrical network model uses the information about the particle composition, to calculate the average electrical properties of the particle in each of the activity stages. This is used by both the Tao Sun model and COMSOL model A to calculate the total measurable system impedance. COMSOL model B will calculate the total measurable system impedance directly from the particle composition. Several models are used, as some models provide better understanding while other models give more accurate results. Furthermore, each model gives slightly more information as different effects can be taken into account. The COMSOL models are much more time consuming and are therefore not suitable for parameter sweeps.

2D electrical network for particle properties

The first model that is described is the 2D electrical network. This model is used to estimate the average electrical properties of the FCC particle and is based on work by Van der Helm [48]. The model assumes an FCC particle which has a cube shape with dimensions of 80 micron. A cube shape is used because this is the most simple shape for calculation. The exact shape does not matter for the resulting average values. To calculate the average electrical properties, some perfectly conducting electrodes are modelled to be located on both the top and bottom of this cubical particle. By calculating the total resistance and capacitance of this system, an estimate can be

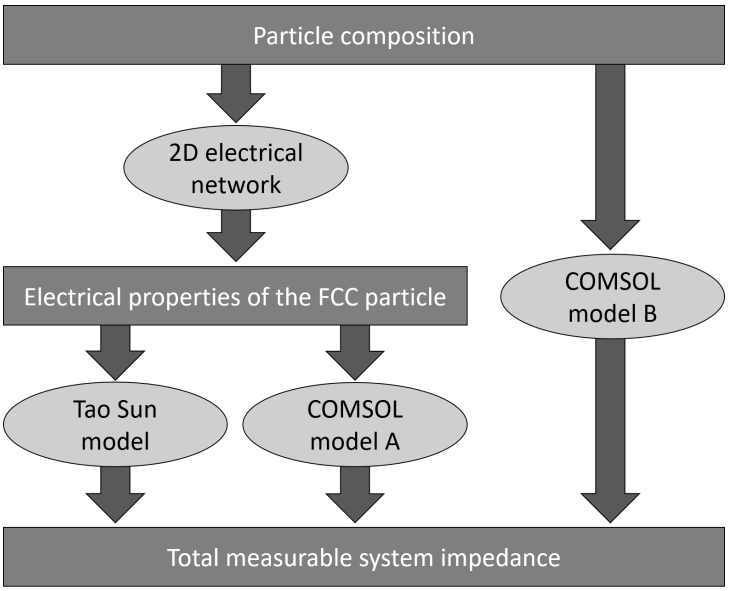

Fig. 2.7: Structure of the models that are used to calculate the impedance change as caused by FCC particles.

made for the resistivity and dielectric constant of the particle.

As the average electrical properties of the particles are unknown, the particle is divided into a large amount of sub-elements. Each of these elements represents a cluster of a pure molecule from Tab. 2.1, for instance Silicon dioxide (SiO2). The electrical properties of these pure molecules are known, therefore the resistance and capacitance of each cluster can be calculated. To make an equivalent circuit model, each cluster is given a square shape and is electrically connected to its direct neighbours.

To make the model as accurate as possible, as many clusters as possible should be used. Furthermore, these clusters should be small 3D structures which are connected to different clusters in all directions. However, due to limitations in calculation power, this is not possible. Therefore, the model that is used only shows material variation in 2 dimensions as shown in Fig. 2.8. Electrodes are placed above and below this particle.

In order to create an equivalent circuit model of the particle as shown in Fig. 2.8, the following steps are taken:

1. The material is divided into a 2D roster of 100 x 100 elements. The total amount of elements is therefore equal to 10000.
2. A random material is assigned to each of the elements in the roster. The total number of elements that belong to one material is related to the percentages as given in Tab. 2.5. As the particle is porous, part of the volume is occupied by the background fluid that is used. The electrical properties of this fluid should therefore be used to include this porosity. The medium that is used in the simulations is anisole, for which the reason will be explained in Chap. 3. Anisole has

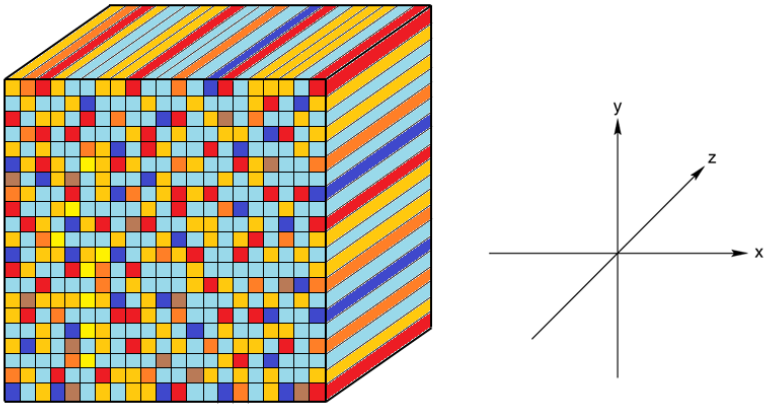

Fig. 2.8: Model of FCC particles as a collection of square clusters. The clusters show variation in the x and y direction, but not in the z-direction, making it a 2D model. Each colour represents a different material for the cluster.

a resistivity of $10^{13}\Omega$m and a dielectric constant of 4.33 [49], [50].

3. Each of the elements is modelled with the circuit as shown in one of the squares in Fig. 2.9. The equivalent circuit model of each element thus consists of four resistors and four capacitors. This connects each element with the four nearest neighbours.
4. The resistivity and dielectric constants used to obtain the resistor and capacitor values of each element depend on the material that is assigned to each element.
5. The total particle is modelled as a square with dimensions of 80 micron. With these dimensions in combination with the resistivity and dielectric constant of each element, all the resistances and capacitances can be calculated. And a large network like Fig. 2.9 is formed.

The next step is to solve this equivalent circuit model to obtain an average value for both the dielectric constant and resistivity of the model. This is done using the nodal voltage method.

In this method each point where multiple electrical components meet, is defined as a node, for instance point V_n in example the circuit of Fig. 2.10. The nodal voltage method starts by defining Kirchhoff's current law for each node. This law indicates that the sum of all currents entering this node is equal to the sum of currents leaving the node. For each node, the equation with Kirchhoff's current law can be written down, giving a set of equations. For node V_n of the example circuit, Kirchhoff's current law becomes:

$$i_1 = i_2 + i_3. \tag{2.11}$$

The next step is to use Ohm's law to convert all currents into equations combining

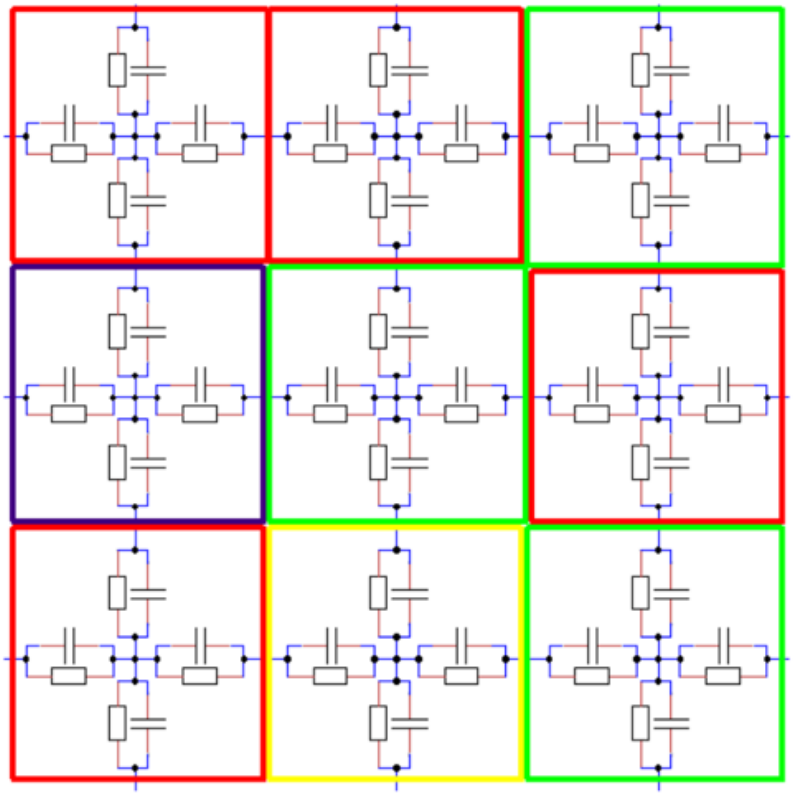

Fig. 2.9: Part of the equivalent circuit diagram used in the 2D electrical network. Each coloured square represents one element in the matrix of 100 x 100 x 1, which contains one specific material.

voltages and impedances:

$$\frac{V_a - V_N}{Z_1} = \frac{V_N - V_b}{Z_2} + \frac{V_N - V_c}{Z_3}. \tag{2.12}$$

The number of nodes that the system contains, is equal to the amount of final equations as the one showed in Eq. 2.12. However, one of the nodes is set to be the reference, or ground node. For this node, the potential is set to zero and no equation is needed to describe its potential. The final equations that are obtained can be solved using linear algebra. This results in solving the voltages present at each node.

To avoid doing all the individual steps of the node voltage method for each node of the large electric network (containing 10000 nodes), some simplified rules can be used. These are explained in the following steps, which are based on literature [51].

6. The nodal voltage method matrix form uses the following equation as starting point:

$$\mathbf{A} \cdot \vec{u}_{nodes} = \vec{z}_{input} \tag{2.13}$$

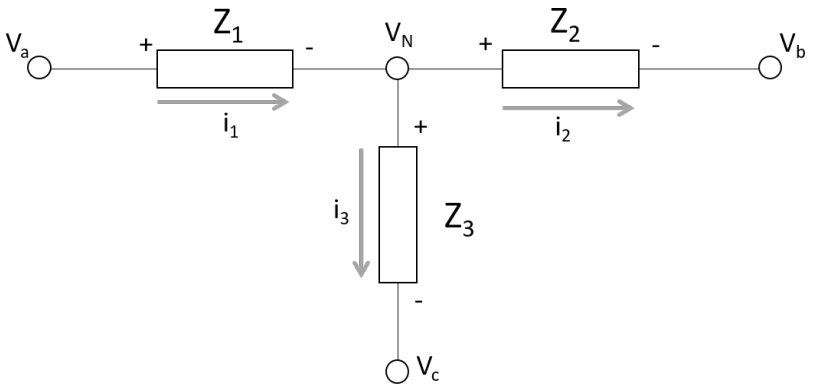

Fig. 2.10: Example of approach in node voltage method.

$$= \begin{bmatrix} a_{1,1} & a_{1,2} & \dots & a_{1,n} \\ a_{2,1} & a_{2,2} & \dots & a_{2,n} \\ \vdots & \vdots & \ddots & \vdots \\ a_{n,1} & a_{n,2} & \dots & a_{n,n} \end{bmatrix} \cdot \begin{bmatrix} v_1 \\ v_2 \\ \vdots \\ v_n \end{bmatrix} = \begin{bmatrix} z_1 \\ z_2 \\ \vdots \\ z_n \end{bmatrix}, \tag{2.14}$$

where **A** represents an impedance matrix which includes the impedances which connect all the nodes together [Ω], $\vec{u}_{nodes}$ represents the voltages at each of the nodes [V] and $\vec{z}_{input}$ represents the known quantities due to voltage or current sources [A]. The indices from 1 till n are used to indicated the node of the element which is used. The number n indicates the total number of nodes, which is in this case equal to 10000. In the matrix, **A**, two indices are used to indicate a relation between these two nodes.

7. Some specific rules are used to obtain the impedance matrix **A**:
   - When 2 nodes (i and j), as shown in Fig. 2.11 are connected, in the matrix at position **A**(i,j) and **A**(j,i) the impedance is equal to $-\frac{1}{Z_{ij}}$, where Z_{ij} is the impedance of the circuit element that is placed between nodes i and j.
   - When 2 nodes are not connected directly by a circuit element in the equivalent circuit model, in the matrix place **A**(i,j) and **A**(j,i) the impedance is equal to 0.
   - On the main diagonal the negative sum of each row is inserted. For the elements that are connected to either the input node (V_{in}) or the ground node, an additional element is added which is equal to $\frac{1}{Z_i}$, to include the connection with the voltage source or ground.
8. The vector $\vec{z}_{input}$ is equal to $\frac{V_{in}}{Z_i}$ for nodes i that are directly connected to the input voltage through an impedance with value Z_i. As in the upper nodes in Fig. 2.11.
9. The voltages at each node can be obtained by:

$$\vec{u}_{nodes} = \mathbf{A}^{-1} \cdot \vec{z}_{input}, \tag{2.15}$$

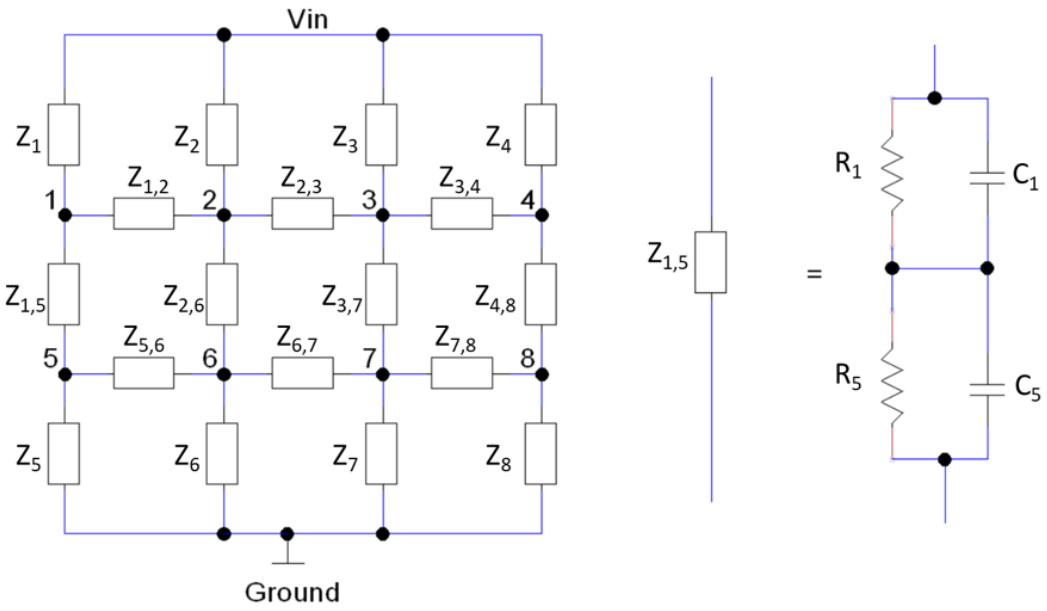

Fig. 2.11: Equivalent circuit model of a system containing 2 x 4 nodes. In the actual calculation a total of 100 x 100 elements is used. The impedance in-between the nodes represent impedances which combines the resistance and capacitance of multiple elements as shown as example for the impedance $Z_{1,5}$.

as the matrix **A** and vector $\vec{z}_{input}$ are completely known.

In order to get the particle properties from the node potentials, some additional calculations are required. As in Fig. 2.11, all the elements on the top row are on one side connected to the input voltage. The total impedance of the complete system is equal to the source voltage divided by the source current. As the source voltage itself can be set and is therefore known, the current is the only requirement to find the impedance. By calculating all the individual currents through the elements on the top row (elements 1 until 4 for the circuit of Fig. 2.11) and the sum of these currents, the total current can be obtained. The total impedance should be separated into a resistance and a capacitance. This is done by first calculating the impedance for a DC input voltage, for which the capacitance is equal to zero: then the impedance is caused completely by the resistance itself. After that an AC voltage is chosen as input and the capacitance is calculated. From the resistance and capacitance, in combination with the dimensions of the element, the average resistivity and dielectric constant of the FCC particle can be obtained.

Tao Sun model: particle between electrodes

The model explained in the previous section, which calculates the average electrical properties of the particle, does not yet give information about the measured impedance

of the complete system of Fig. 2.1. To get from the particle properties to the system impedance that is finally measurable, the properties of the complete system should be taken into account, which includes the dimensioning and the material properties of the fluid. For a spherical particle in-between rectangular electrodes, a model to calculate the final impedance already exists in literature [8]. This model uses Maxwells mixture theory as starting point. This relates the electrical properties of the mixture with the individual properties of the solution and the spherical particle. The Maxwell Mixture equation is defined as:

$$\tilde{\epsilon}_{mix} = \tilde{\epsilon}_{med}\frac{1 + 2\Phi\tilde{f}_{CM}}{1 - \Phi\tilde{f}_{CM}}, \tag{2.16}$$

where $\tilde{f}_{CM}$ represents the unitless complex Clausius Mossotti factor as defined in Eq. 2.17 and Φ the unitless volume ratio between the particle and the medium as defined in Eq. 2.18.

$$\tilde{f}_{CM} = \frac{\tilde{\epsilon}_{par} - \tilde{\epsilon}_{med}}{\tilde{\epsilon}_{par} + 2\tilde{\epsilon}_{med}} \tag{2.17}$$

$$\Phi = \frac{V_{par}}{V_{med}} \tag{2.18}$$

In these equation, $\tilde{\epsilon}_{mix}$, $\tilde{\epsilon}_{med}$ and $\tilde{\epsilon}_{par}$ represent the complex permittivities of the mixture, the medium and the particle respectively. A complex permittivity includes both the resistivity and the dielectric constant of an element:

$$\tilde{\epsilon} = \epsilon - \frac{j\sigma}{\omega} \tag{2.19}$$

where ϵ represents the permittivity, σ the conductivity and ω the angular frequency.

When using a shelled particle, the electrical properties of the particle itself depend on the individual inner and outer shell properties. This is defined as:

$$\tilde{\epsilon}_{par} = \tilde{\epsilon}_{shl} - \frac{\gamma^3 + 2K}{\gamma^3 - K}, \tag{2.20}$$

where K and γ are the following parameters:

$$K = \frac{\tilde{\epsilon}_{inn} - \tilde{\epsilon}_{shl}}{\tilde{\epsilon}_{inn} + 2\tilde{\epsilon}_{shl}} \tag{2.21}$$

$$\gamma = \frac{R + d}{d}. \tag{2.22}$$

In this equation, R represents the diameter of the inner volume of the particle [m] and d the thickness of the outer shell [m]. Combining these equations will give a final equation for the average electrical properties of the complete mixture. This will allow for the calculation of the final impedance, using simple equations, whenever either the resistance or the capacitance is dominant.

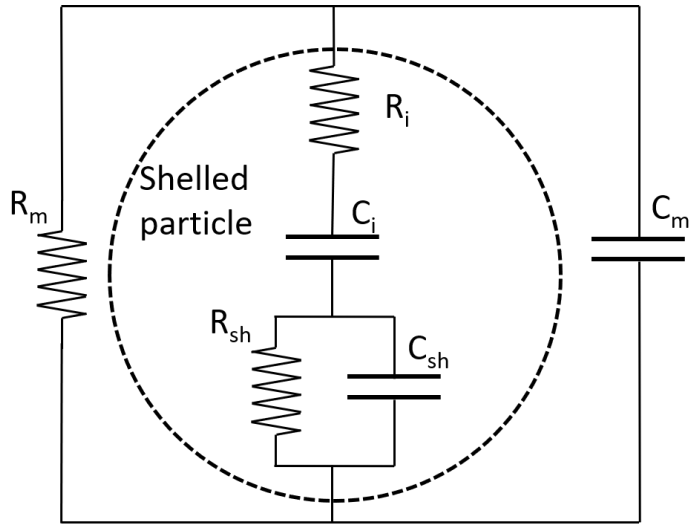

Fig. 2.12: The equivalent circuit used to model a shelled particle in-between electrodes, modified from [8].

Furthermore, as explained in the paper of Sun, an equivalent circuit of the complete system can be made [8]. This equivalent circuit is shown in Fig. 2.12. This circuit can be used to analyse the individual contributions in more depth and to perform frequency analysis. The calculations of the resistor and capacitor elements is explained in detail in the paper of Sun [8].

In the model of the FCC particle, a total radius of 40 micron is used with an outer layer of 2 micron, as the metal mainly accumulates in this region. The resistivity and dielectric constants that are used, originate from the 2D electrical network model. Multiple simulations are performed to optimize the system parameters, like the channel dimensions and the choice of medium.

COMSOL simulations

Besides the previously described simulations which are analytical models, also some finite element models are made in COMSOL [52]. The advantage of using COMSOL, is that it allows for the calculation of the stray capacitance and makes it possible to change the particle position inside the channel. Furthermore, the results of the COMSOL simulations are assumed to be more accurate. However, as these simulations are more time consuming, optimizing a certain parameter is easier to do using the previous described Matlab simulations.

Two different models are made in COMSOL. First of all, a shelled particle is modelled with homogeneous electrical properties. This particle has two dielectric constants, one for the shell and one for the inner part. In this model, the electrical properties of the particle are taken from the 2D electrical network model. This model is thus an alternative for the analytical model using Maxwell's mixture equations.

A simplified rendering of this model in COMSOL is shown in Fig. 2.13. The ma-

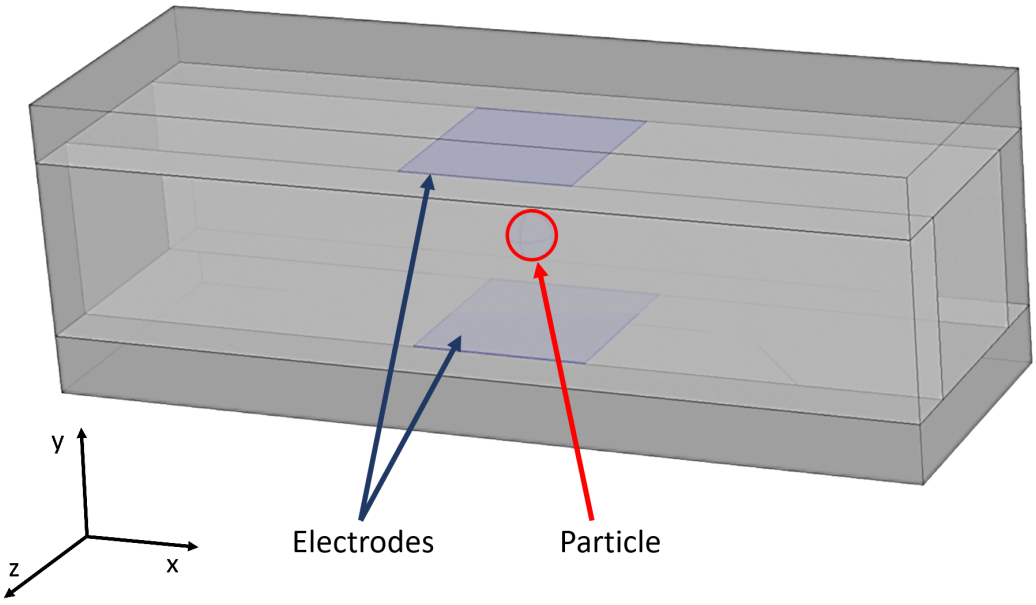

Fig. 2.13: Simplified rendering of the COMSOL simulation showing the channel containing the electrodes in blue together with a shelled particle exactly positioned in between these electrodes. The actual used structure in COMSOL contains a longer channel with thicker walls and includes the connections to the electrodes, which are left out for clarification purposes.

terials used for the channel walls are determined by cleanroom processes which will be explained in Chap. 3. The top and bottom channel walls will be mempax with a dielectric constant of 4.8 [53]. The side walls will be made from SU-8 with a dielectric constant of 4 [54].

In the second model that is made, the distribution of clusters in the particle is incorporated into the model. This model can thus be seen as a alternative for the combination of the 2D electrical network model and the analytical model using Maxwell's mixture equations. In this model a 3D cluster distribution is used with 200 by 200 by 200 elements. This distribution is shown in Fig. 2.14. This block is randomly given a value between 0 and 100. Hereafter, according to the percentages of each molecule that are present, each cluster is assigned to a molecule. For the simulations the same structure as in the first COMSOL model as shown in Fig. 2.13 is used. The electrical properties are however not homogeneous. The randomized cluster locations as shown in Fig. 2.14 is used to make the particle properties inhomogeneous. Metal accumulation mainly occurs on the outer layer of the particle, which is incorporated into the model by assigning more clusters to the metal properties for the outer 2 micron.

The performed simulation of both COMSOL models are electrostatic stationary simulations of the capacitance. The mesh that is used is physics-controlled and extremely fine. Two electrodes are used, of which one is the ground terminal and the other is a normal terminal to which a potential of 1V is applied. The Maxwell capaci-

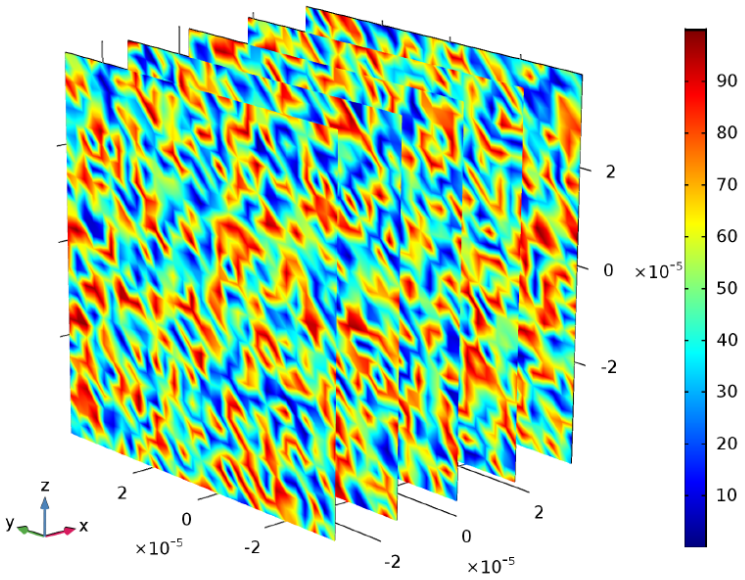

Fig. 2.14: Image showing the randomized position of the clusters. The cube is divided into 200 x 200 x 200 elements which is given a random number between 0 and 100.

tance is hereafter calculated between the two electrodes. A spherical particle with a radius of 40 micron with one shell is placed in-between the electrodes and the dielectric properties of this particle are adapted according to the wanted situation.

2.3.2 Results and discussion

2D electrical network for particle properties

To obtain the average electrical properties of both the particle shell and inner volume in each metallization state, multiple sets of simulations are performed. The percentages used in the simulation relates to the specific situation and layer that is modelled and corresponds to Tab. 2.5. Because the outcome of each simulation is dependent on the exact positioning of the clusters, a total of 20 simulations are performed for each situation and averaging of the results is performed. In the simulations both the resistivity and the dielectric constant are calculated. The resistivity results of the simulations are shown in Fig. 2.15. The dielectric constant results are shown in Fig. 2.16. Both the average value and the standard deviation due to the cluster location differentiation are shown in these figures. A table summarizing the final resistivity and dielectric constant values for each state is shown in Tab. 2.6.

These results show that the most change in resistivity and dielectric constant are in the outer layer of the particle. This is according to expectation as most of the metals accumulate in this region. Furthermore, the metal accumulation causes a drop in the resistivity, while the dielectric constant increases.

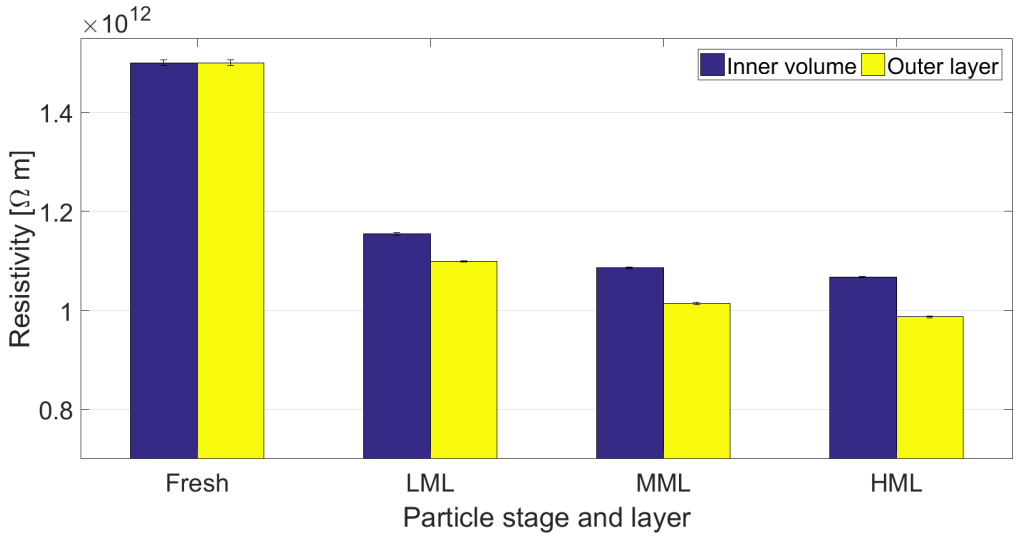

Fig. 2.15: Results of simulations for the resistivity of both the inner and outer volume. The height of the bars represents the average values and the error bars show the standard deviation due to the difference in location of the clusters between the simulations.

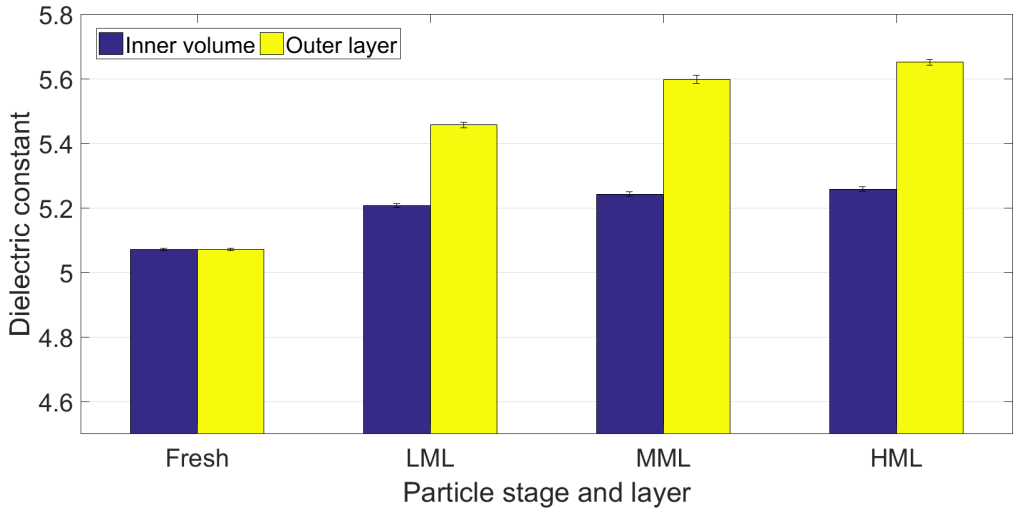

Fig. 2.16: Results of simulations for the dielectric constant of both the inner and outer volume. The height of the bars represents the average values and the error bars show the standard deviation due to the difference in location of the clusters between the simulations.

Tao Sun model: particle between electrodes

Using the results of the electrical properties of the FCC particles, simulations can be done to calculate the expected change in system impedance. With these simulations the influence of multiple parameters on the impedance can be checked. This can be used to optimize each of these parameters. The parameters that are optimized are the measurement frequency, the electrode and channel dimensions and the choice of

Tab. 2.6: Electrical properties of the inner volume and shell for the different metallization states.

Electrical property	Fresh	LML	MML	HML
Resistivity inner volume [$10^{12}\Omega$m]	1.5005	1.1547	1.0858	1.0671
Resisitivity shell [$10^{12}\Omega$m]	1.5005	1.0991	1.0140	0.9872
Dielectric constant inner volume	5.0708	5.2075	5.2425	5.2583
Dielectric constant shell	5.0708	5.4566	5.5977	5.6511

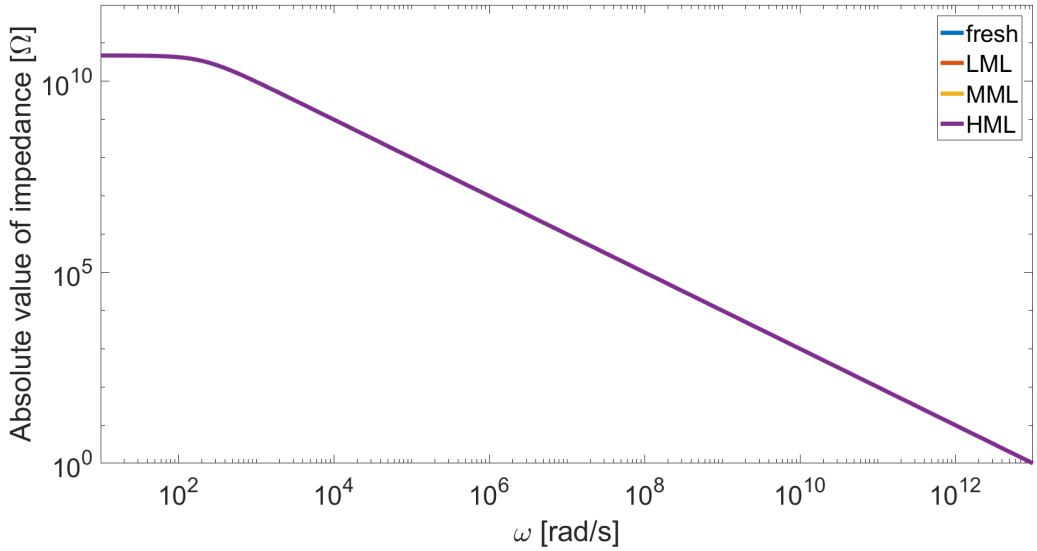

Fig. 2.17: Absolute value of the impedance versus the system driving frequency. The impedance is plotted for the four stages of metal loading. However, as the impedance difference is small. the lines overlap.

liquid.

To check whether it is most suitable to use the particle resistance or dielectric constant, some simulations of the frequency response of the system are done. The channel dimensions as shown in Fig. 2.1 are equal to 300 micron for both the electrode width and length. The channel height which is the spacing between the electrodes is equal to 230 micron. The fluid that is used is demineralized water with a dielectric constant of 29.3 and the resistivity is 18.2M [Ωm] [55], [56].

A bode plot is made for the frequencies between 1 and 10^{13} radians/seconds and the result is shown in figure Fig. 2.17. The result is shown for each of the metal loading stage, but since the differences between these stages are small, this is not visible in the figure. Therefore another plot is made to show the percentual differences between each stage with respect to the fresh particles. This is shown in Fig. 2.18.

The bode plot shows two main features. First, there is the plateau for the frequencies below 100 rad/s. In this range the resistance of the system is dominant. At higher frequencies, the capacitance becomes dominant, which is visible by the -20dB per

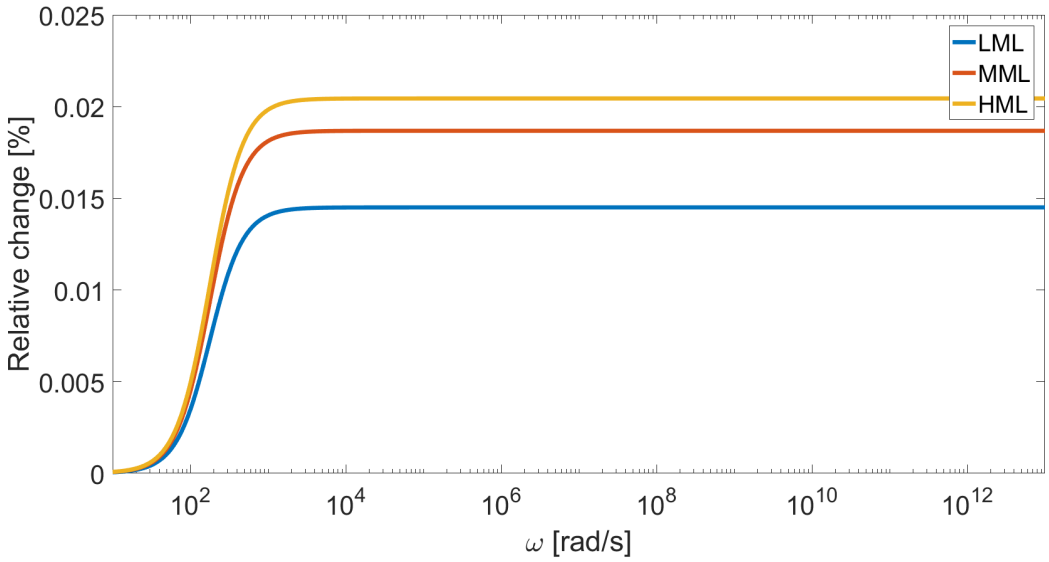

Fig. 2.18: The relative change in impedance between particles at which metal has accumulated (LML, MML or HML) and fresh particles without metal loading.

decade decrease of the impedance. What is not visible in this figure, is the electric double layer capacitance, which is present at the interface between the channel walls and the liquid. As the double layer is not of interest in this research and only present at low frequencies while using a conductive medium, the effects of the double layer capacitance are neglected [57].

Fig. 2.18 shows that the percentual change in impedance is largest at high frequencies. Using a different fluid with a resistivity closer to the particle resistivity would increase the relative change in this regime. However, the frequency at which the resistance of the system is dominant is already low and would only reduce when using a higher fluid resistivity. It is thus most suitable to use the capacitance and therefore the dielectric properties of the FCC particle.

Simulations showing the influence of the channel width and length are shown in App. A.1. This shows that to maximize the relative change in capacitance, the length and width of the electrodes should be as low as possible. However, the absolute change in capacitance remains constant for increasing electrode length and width.

The influence of the electrode spacing is shown in App. A.2. The simulations show that a smaller electrode spacing will result in both a larger relative change in capacitance as well as in a larger absolute change in capacitance.

The dielectric constant of the fluid is also varied to check its influence. The simulation results are shown in App. A.3. From these results can be concluded that the largest absolute change in capacitance is obtained when using a high dielectric constant. However, the largest relative change in capacitance is obtained when using a medium with a dielectric constant of about 2.74, which is about half the FCC dielectric constant.

The capacitance that is measured, is not only affected by the metal content on FCC particles, but also by the size of the particle. In App. A.4, the effect of particle size is shown for multiple fluid dielectric constants. The simulations show that the effect of size variations is smaller whenever the dielectric constant of the fluid is close to the particle dielectric constant. The choice of dielectric constant can thus be used to reduce the effect of size differentiation of FCC particles.

Tab. 2.7: Capacitance of the system for the different metal accumulation stages simulated using the Tao Sun model. Shown for using two different fluids which are of possible interest.

	Capacitance [fF] (change in capacitance with respect to a fresh particle [aF])				
Medium (ϵ_r)	Fresh	LML	MML	HML	No particle
Demineralized water (29.3)	100.0217 (-)	100.0362 (14.5)	100.0403 (18.7)	100.0421 (20.5)	101.5152 (1493.5)
Anisole (4.33)	15.0335 (-)	15.0404 (6.8)	15.0423 (8.8)	15.0431 (9.6)	15.0007 (32.8)

The capacitance value of the system for the different metal accumulation stages are shown in Tab. 2.7. This is shown for both demineralized water and anisole with dielectric constant of 29.3 and 4.33 respectively [55] [50] as these are two potentially interesting fluids. This table shows that the change in capacitance is highest when demi water is used. However, also the difference between no particle and a fresh particle is significantly higher for using demineralized water. This makes it easier to detect the FCC particles itself, but complicates finding the small difference in metal loading.

COMSOL

As explained in Sec. 2.3.1 two types of simulations are done using COMSOL. In the first set of simulations, the dielectric properties of the inner volume and the outer layer are homogeneous, and this is performed as alternative for the Tao Sun model. The system capacitance for the different metal accumulation stages are shown in Tab. 2.8. Comparing these results to Tab. 2.7 shows expected behaviour. In the COMSOL model the stray capacitance is taken into account, which greatly increases the total capacitance. As expected, the change in capacitance due to metal accumulation are comparable for the COMSOL model and the Tao Sun model. The results of these models are thus in agreement.

The position dependence of the particle capacitance is also simulated using this model. This is done for fresh FCC particles which are moved in the 3 axis directions as shown in Fig. 2.13. The results of these simulations are shown in Tab. 2.9. The

Tab. 2.8: Capacitance of the system for the different metal accumulation stages simulated using the first COMSOL model. Shown for using two different fluids which are of possible interest.

	Capacitance [fF] (change in capacitance with respect to a fresh particle [aF])				
Medium (ϵ_r)	Fresh	LML	MML	HML	No particle
Demineralized water (29.3)	363.5812 (-)	363.5958 (14.6)	363.6000 (18.8)	363.6018 (20.6)	365.0898 (1508.6)
Anisole (4.33)	221.4779 (-)	221.4848 (6.9)	221.4868 (8.9)	221.4876 (9.7)	221.4460 (31.9)

Tab. 2.9: Position dependence of system impedance for fresh FCC particles in anisole moving 10, 20 and 50 micron in each direction. The x-direction is the direction along the channel. The y-direction is towards the wall of the channel where the electrodes are located. The z-direction is towards the other wall of the channel

	Capacitance [fF] (change in capacitance w.r.t center position) [aF]			
Movement direction	0 µm	10 µm	25 µm	50 µm
x	221.4779 (-)	221.4781 (0.2)	221.4778 (0.1)	221.4774 (0.5)
y	221.4779 (-)	221.4785 (0.6)	221.4798 (1.9)	221.4813 (3.4)
z	221.4779 (-)	221.4779 (0.0)	221.4780 (0.1)	221.4775 (0.4)

position dependence of the detected capacitance is largest when the particle moves towards one of the electrodes. This capacitance change is smaller than the expected change in capacitance due to metal loading as seen in Tab. 2.8. It can however still have a significant influence on the experimental results.

The second COMSOL model directly incorporates the randomized distribution of molecules. For this model again the capacitance in the different metal accumulation stages are simulated and shown in Tab. 2.10. The total capacitance is as expected in the same range as the first COMSOL model. The change in capacitance however shows a quite significant difference. In this second model, the step between fresh and LML particles is much higher than any of the other steps and is also significantly higher compared to the first COMSOL model.

The cause of this difference might be due to the large number of total elements that is used in the second COMSOL model. The first COMSOL model uses the results of the 2D electrical network which uses in total 10 thousand elements, while the second model uses 80 Million elements. Furthermore, the 2D electrical network model might not be completely accurate due to the simplifications that are made in making the equivalent circuit model.

Nevertheless, both models clearly show that there is a difference between fresh

Tab. 2.10: Capacitance of the system for the different metal accumulation stages simulated using the second COMSOL model. Shown for using two different fluids which are of possible interest.

	Capacitance [fF] (change in capacitance with respect to a fresh particle [aF])				
Medium (ϵ_r)	Fresh	LML	MML	HML	No particle
Demineralized water (29.3)	363.6668 (-)	363.6915 (24.7)	363.6950 (28.2)	363.6958 (29.0)	365.0898 (1423.0)
Anisole (4.33)	221.5167 (-)	221.5269 (10.2)	221.5283 (11.6)	221.5287 (12.0)	221.4460 (70.7)

particles and particles where metal has accumulated. This difference is expected to be between 14.5-29aF for using demineralized water and between 7-12 aF for using anisole. Depending on the amount of metal which has accumulated on the particle.

2.4 Microfluidics

To detect the FCC particles in a continuous way, microfluidics is used. Microfluidics has proven to be very effective in sensing applications [58]. It is therefore being used extensively in combination with impedance spectroscopy [59]–[61]. By flowing the particles one after the other through the chip, the throughput of measuring is greatly increased, while it is still possible to analyse each of the particles individually.

The most important considerations of microfluidics are the choice of medium and the flow that is created. The medium choice is partly made based on the electrical properties, for which the relevance is explained in Sec. 2.3. Furthermore, The fluid density, viscosity and interaction with the channel walls and the particle are also of relevance. For instance, the fluid should not react with the channel walls or the particles.

The flow that is created within the channel will be important for the measurements that are performed. Although a faster flow of particles increases the potential throughput of the device, the particle should not pass the electrodes with too high velocities, otherwise measurements can not be performed accurately. This is partly caused by the limited sample rate which is used, but also due to filtering which is used to greatly reduce the noise that is measured. This filtering will also remove any fast changes in impedance introduced by particles moving with high speed. A trade-off should therefore be made between the speed of the particles and the amount of filtering.

To improve the control over the particle motion and speed, laminar flow is wanted inside the channel. Whether the flow through the micro-channel is laminar or turbulent

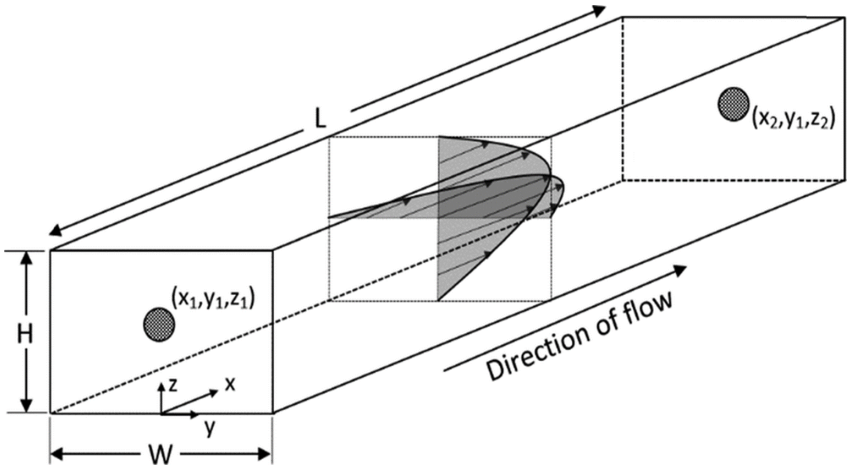

Fig. 2.19: Flow profile in a rectangular channel, modified from [64]

depends on Reynolds number:

$$Re = \frac{D_H v \rho}{\mu}, \tag{2.23}$$

Where Re is the unitless Reynolds number, D_H is the hydraulic diameter in [m], v is the average velocity of the fluid in [m/s], ρ the density of the fluid in [kg/m^3] and μ is the dynamic viscosity in [Pa s] [62]. The hydraulic diameter of a square channel is defined as:

$$D_H = \frac{4wh}{2(w+h)}, \tag{2.24}$$

where w is the width of the channel in [m] and h the height in [m] [62]. Whenever Reynolds number is smaller than 2100, laminar flow is obtained [63]. To ensure that laminar flow is created, the channel dimensions, the medium and the flow speed that are used should be taken into consideration.

For movement of the medium through the channel, a syringe pump will be used. With this pump, the amount of flow per time unit can be set, which can be used to calculate the velocity of the fluid. For laminar flow, the flow profile that is created by the syringe pump will look like Fig. 2.19 [64], where flow will be largest in the exact middle of the channel and will reduce towards the channel walls.

The movement of FCC particles inside the channel is caused by two forces, drag forces and gravitational forces. As the particle will most likely have a higher density compared to fluid, gravitational forces will act on this particle. The gravity force acting on the particles is described in Eq. 2.25 [65].

$$F_{Gp} = (\rho_s - \rho_f) g \frac{\pi d^3}{6} \tag{2.25}$$

In this equation ρ_s represents the density of the particle in [kg/m^3], ρ_f the density of the liquid in [kg/m^3], g the gravitational acceleration in [m/s^2] and d the diameter

of the particle in [m]. The difference in density of the particle and medium will therefore determine the sedimentation speed due to gravity. When the channel is placed horizontally, the particles will sink to the bottom of the channel. Placing the channel vertically is another possibility. The direction of the gravitational forces can then either be in the same or opposite direction to the flow that is created. This will have an effect on the velocity with which the particles passes the electrode.

The second force is the drag force due to the difference in movement of the medium and the particle. As flow is created inside the channel, the medium will move with a certain velocity. This movement will cause the particle to be dragged along the channel. For fluids with low Reynolds number, Stokes drag will be exerted on the particle, for which the force is shown in Eq. 2.26 [66].

$$F_D = 3\pi\mu v_{rel} d \tag{2.26}$$

Where F_D is the drag force in [N], μ the dynamic viscosity in [Pa s], v_{rel} the relative velocity of the fluid with respect to the particle in [m/s] and d the diameter of the particle in [m].

The combination of gravity forces and drag forces and possibly interaction forces with channel walls will determine the speed at which the particle moves through the chip.

Chapter 3

Design

In this chapter the complete design of the experimental set-up is discussed. The design choices that are made are based on literature, experience and on the models as discussed in Chap. 2. In the first section, only the design of a microfluidic chip is discussed. Hereafter, the complete measurement set-up is explained.

3.1 Microfluidic chip design

A simplified drawing of the designed microfluidic chip is shown in Fig. 3.1. The design contains three inlets which are used for flow focus. Furthermore, two sets of electrodes are included, which allows for differential measuring.

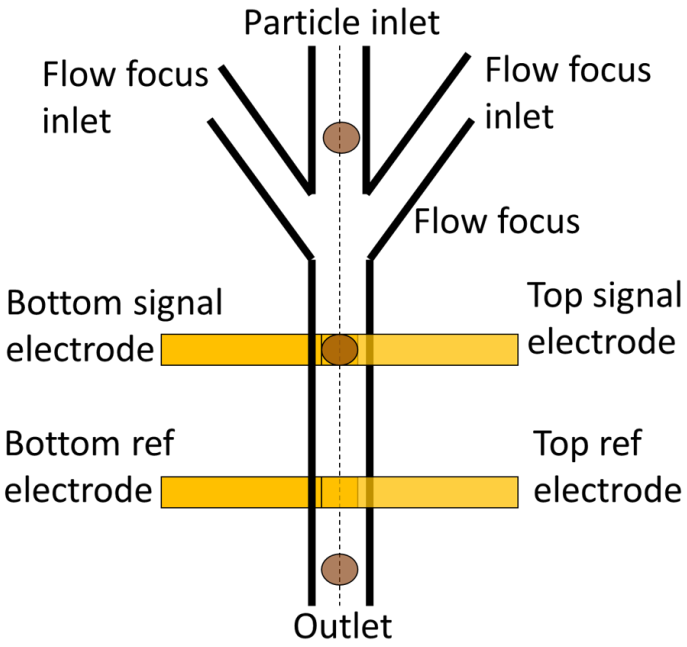

Fig. 3.1: Schematic image of the design of the microfluidic chip used in the sensing of FCC activity

3.1.1 Particle position dependence

Due to the anisotropy in the electric field as generated, caused by the stray field introduced at the edges of the electrodes, the effect which the particle has on the final impedance is dependent on the exact position of the particle. This is also shown in the simulation results of Tab. 2.8. To reduce this effect, some features are added into the design, which will be discussed next.

Flow focus

Flow focus is added to ensure that all particles will cross the electrode at approximately the same position. A simple way to include flow focus is by using two extra inlets besides the particle inlet as shown in Fig. 3.1 [67], [68]. These inlets, combined with the particle inlet with a certain angle, hereby allow for focussing of particles in the centre of the channel. The design will thus only focus the particles position in one dimension.

Ground planes

Another method to reduce the position dependence of the measured capacitance is the addition of ground planes. This method counters the direct cause of the position dependence, which is the non-uniform electric field due to edge effects of capacitors [69]. By adding some grounding planes around the electrode, the electric field becomes more uniform. This is made visible in Fig. 3.2. In Fig. 3.2a the electric field between the channel is shown without the addition of ground planes. In Fig. 3.2b, the ground planes are included and the electric field is shown again. This shows that, around the position of the particle which is indicated, the uniformity of the electric field is increased by the addition of ground planes. The location of the ground planes in the design is shown in Fig. 3.3.

Besides the improvement of the uniformity of the electric field, the grounding electrodes are also added to shield the sensitive electrodes. Shielding reduces coupling between the system and noise sources that are present around the set-up [70]. Without shielding, the electrodes and the wires of the system could act as an antenna and pick up signals from the surrounding. The grounded electrodes create a barrier for the electric field lines from the noisy surrounding. These field lines will therefore no longer reach the sensitive circuit elements, hereby significantly reducing the amount of noise as present in the system.

3.1.2 Differential measuring

The total capacitance of the system is not relevant for the purpose of detecting the FCC particle activity. Only the capacitance change caused by the particle is important.

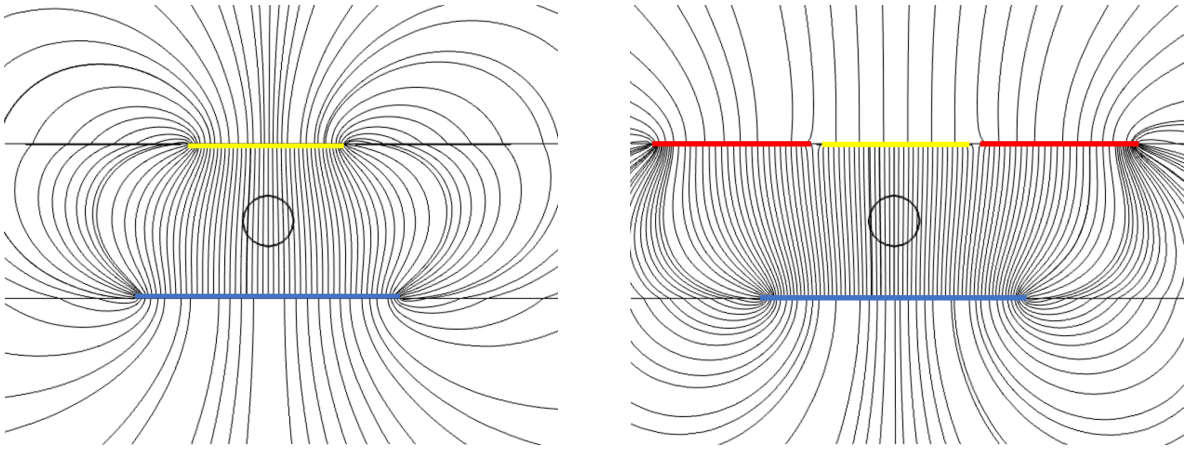

(a) Electric field inside the channel without the addition of groundplanes.

(b) Electric field inside the channel with groundplanes included.

Fig. 3.2: Comparison of the electric field generated inside the channel, without and with added ground planes. In the figures, the yellow line represent the top electrode, the blue line the bottom electrode and the red lines the added ground electrodes.

To be able to only measure this capacitance change introduced by the FCC particle, a differential measurement is performed. For this differential measurement, two identical capacitors are used as shown in Fig. 3.1. The capacitance detection system can be adapted to only measure the difference between these capacitor values:

$$C_{meas} = C_1 - C_2. \tag{3.1}$$

Whenever no particle is located between both of the capacitors, only the medium will be present. Because both the dimensions and the dielectric constants of both sets of electrodes are identical, the measured capacitance should be zero. Whenever a FCC particle is present between the electrodes of C_1, the capacitance of this capacitor will change, due to the dielectric properties of the particle, which is different from the medium dielectric constant. One of the advantages of differential measuring is the reduction of parasitic effects [71]. Since the parasitic capacitance should be identical for both capacitance, the parasitic effects will almost completely be cancelled out. Furthermore, also the influence of changes over time, for instance changes in temperature, will be reduced as the change is equal for both capacitors C_1 and C_2.

3.1.3 Design considerations

Some of the design choices that are made, are partly based on simulations as can be seen in Chap. 2. The discussion of these results are explained in this section. First the dimensions of the device that are used are explained. Thereafter, the choice of medium is substantiated. The final choices that are made are listed in Tab. 3.1.

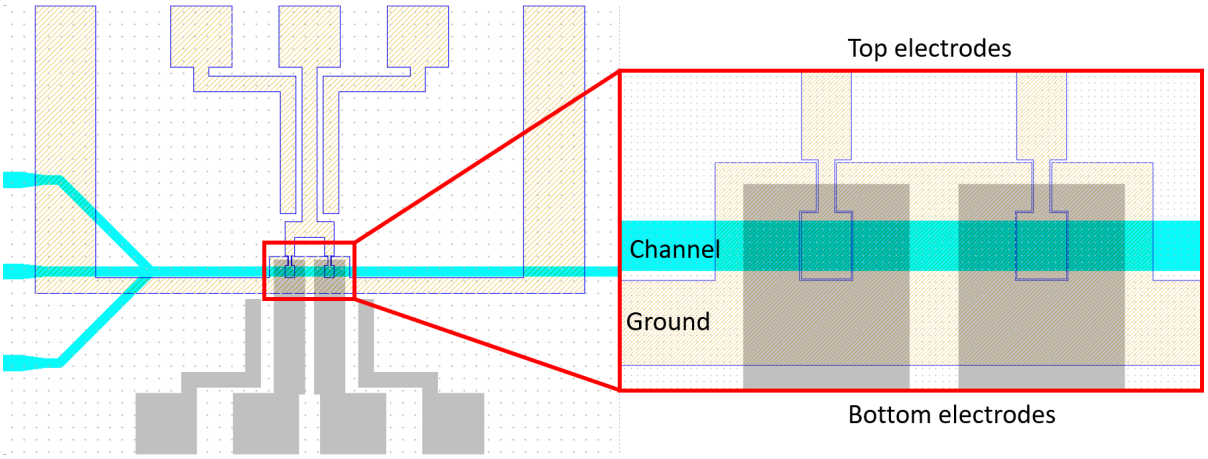

Fig. 3.3: Simplified image of the masks used in the fabrication of the microfluidic chip. In cyan the mask for the channel is shown, the grey mask shows the bottom electrodes and the light yellow mask shows the top electrodes.

Tab. 3.1: Summary of the design choices that are made in the microfluidic chip design.

Parameter	Value
Electrode length	300 µm
Electrode width	300 µm
Electrode spacing	230 µm
Distance between sensing capacitors	1000 µm
Medium choice	Anisole
Medium dielectric constant	4.33
Medium resistivity	$10^{13}\Omega$m
Medium viscosity	0.778-1.52 cP
Medium density	995.6 kg/m^3

Device dimensions

The length and width of the electrode are both chosen to be 300 µm. This value is the result of a trade-off. For smaller dimensions, the relative change in capacitance created by the FCC particle is larger. However the absolute change will not become larger. Furthermore, smaller channel dimensions will increase the change of particle clogging and will reduce the time for which the particles are in between the electrodes. This is caused by the decreased length of the electrodes.

As found during modelling, the electrode spacing should be as small as possible to maximize the change in measured capacitance due to metal accumulation. Whenever the spacing is too small, there is an increased change of particle clogging. As trade-off, an electrode spacing is chosen to be 230 µm.

The distance between the two sensing capacitors, the signal and reference electrodes in Fig. 3.1, is chosen such that they do not influence each other. The distance

should however also not be too large, else small differences in temperature or fluid properties can arise. The value of $1000\,\mu m$ is chosen as a trade-off.

Medium

The medium that is chosen is anisole. This choice is based mostly on the dielectric constant of 4.33 [50], [72]. Although the absolute change in capacitance caused by metal accumulation is smaller for anisole in comparison to demineralized water, as shown in Tab. 2.8 and Tab. 2.10, the effect of particle size differentiation is greatly reduced when using anisole, which is shown in App. A.4. The dielectric constant of the medium should be as close to the FCC particle dielectric constant to reduce the size effects. When using demineralized water, the effect of $1\,\mu m$ radius differentiation would increase the measured capacitance with 100aF which would completely overshadow the change in capacitance due to metal accumulation. For anisole the change in capacitance is lower than 2.5aF for a $1\,\mu m$ radius differentiation.

Another relevant property of anisole is the resistivity, which is $10^{13}\Omega$m [49]. This resistance is high enough for the capacitance to be dominant, even at low frequencies.

The viscosity of anisole is 1.52 centipoise at 15 degrees Celsius and 0.778 centipoise at 30 deg Celsius and therefore similar to the viscosity of water [73]. The density of anisole is 995.6 kg/m^3 and is thus also very similar to water [73].

3.2 Measurement set-up design

An overview of the measurement set-up used in the detection of the FCC particle activity is shown in Fig. 3.4. This design makes use of a lock-in architecture similar to the one used by Wei [19]. From the options of impedance detection as given in Sec. 2.1.2, the lock-in architecture was chosen for several reasons. First of all, the measurements using the lock-in amplifier are fast and sensitive, due to the high frequency and small bandwidth at which the measurement can be performed [13], [14], [74]. Furthermore, the set-up is relatively easy to build and it is possible to incorporate differential measurements. The complete set-up is divided into several elements, which are discussed next.

3.2.1 Function generation

To be able to perform differential measurements, both sensing capacitors are driven by a sinusoidal signal which has the same amplitude and frequency, but a phase difference of exactly 180 degrees. The two sensing capacitors are connected on the other end as can be seen in Fig. 3.4. By connecting the capacitors this way, the current at

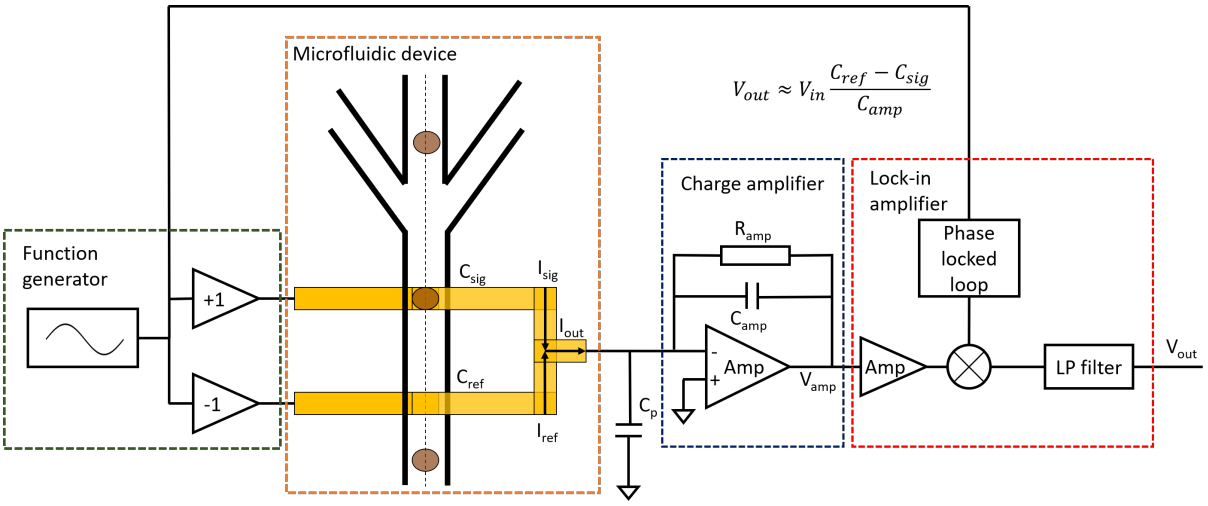

Fig. 3.4: Overview of the measurement set-up design using a lock-in architecture.

this node will only be dependent on the difference in the two capacitances. The current through this node will thus be defined by:

$$I_{out} = I_{sig} + I_{ref} = j\omega V_{in} C_{sig} - j\omega V_{in} C_{ref} = j\omega V_{in}(C_{sig} - C_{ref}). \tag{3.2}$$

Due to imperfections in the fabrication of the device, the capacitances C_{sig} and C_{ref} will not be exactly the same. This will result in an offset of the output current of the microfluidic device. To counter this, the amplitude with which both capacitors are driven can be adjusted.

For the measurement frequency a value of 300 kHz is used. At this frequency, the capacitance of the system is dominant with the used medium of anisole.

3.2.2 Charge amplifier

In order to measure the capacitance difference of the microfluidic device, the current which is the output of the system should first be converted into a voltage. This is done using a simple charge amplifier. The output of this amplifier is formulated as:

$$V_{amp} = -I_{out} \frac{1}{\frac{1}{R_{amp}} + j\omega C_{amp}}. \tag{3.3}$$

The value of the resistor R_{amp} is chosen to be $1 M\Omega$, which is relatively high, such that the amplifying behaviour is dominated by the capacitor. The output of the amplifier then becomes as:

$$V_{amp} = -I_{out} \frac{1}{j\omega C_{amp}}. \tag{3.4}$$

Combining Eq. 3.2 and Eq. 3.4 gives the total expression for the input voltage of

the lock-in-amplifier indicated as:

$$V_{amp} = j\omega V_{in}(C_{ref} - C_{sig})\frac{1}{j\omega C_{amp}} = V_{in}\frac{C_{ref} - C_{sig}}{C_{amp}}. \tag{3.5}$$

These calculations assume a perfect operational amplifier with infinite gain. In reality, this is however not the case. Therefore, some noise is generated by the reading circuit:

$$V_{no}^2 = V_{nA}^2\left(1 + \frac{C_p}{C_{amp}}\right)^2 + I_{nR}^2\frac{1}{j\omega C_F}, \tag{3.6}$$

where V_{no} is the generated noise [V], V_{nA} the voltage noise at the input of the operational amplifier [V], C_p is the parasitic capacitance as indicated in Fig. 3.4 [F] and I_{nR} is the thermal noise density of the amplifier resistance R_{amp} [A]. To minimize the noise, an amplifier should be chosen with minimum input noise density. Furthermore, the parasitic capacitance C_p should be as small as possible.

The capacitor used in the amplification circuit has a value of 3.3pF. This value is chosen as a trade-off between signal and noise amplification and based on experience. Choosing lower values would result in higher signal amplification. However, the noise that is present would also increase which is not wanted.

3.2.3 Lock-in amplifier

In order to perform high accuracy measurements of the output voltage of the charge amplifier, a lock-in amplifier is used. This device is capable of measuring at a specific frequency, hereby removing the noise that is present on other frequencies. The lock-in amplifier measures the amplitude of the signal V_{amp} at the specific frequency of the input signal as explained in Sec. 2.1.2. The output of the lock-in amplifier are an in-phase and out-of phase voltage representing the amplitude of the measured voltage (V_{amp}) at the specific frequency. Only the in-phase output of the lock-in amplifier is of interest, as this represents voltage as indicated in Eq. 3.5. The out-of phase voltage of the lock-in amplifier represents the resistance of the electrodes of the microfluidic device.

The main settings of the lock-in amplifier that are of importance are the sample rate and the bandwidth. The bandwidth that is required, depends on the velocity of the particles. A lower bandwidth results in a larger reduction of noise. To ensure that the passage of particles are not removed by filtering, a bandwidth of 100Hz is used. The sample rate should be high enough to capture the complete curve. To achieve this, a sample rate of 899 samples per second is used.

3.2.4 Shielding compartment

As explained in Sec. 3.1.1 ground planes are added to the device in order to shield the sensitive electrodes from noisy signals around the set-up. For the same reason, all the sensitive element of the system are placed in a grounded box. This box contains two compartments, one for the microfluidic device and one for the charge amplifier. The currents that run through the conductors in these sections are very small and therefore extremely sensitive to noise. The other segments are less sensitive to noise and therefore not included in the grounded box.

3.2.5 Remaining set-up elements

A camera is used during measurements to get a size-estimation of the particles. The camera is zoomed in to the electrode elements of the chip and checks whether the peaks from the lock-in architecture are corresponding to a single particle. When clusters or dirt passes by the chip instead, the data is ignored.

A syringe pump is used to flow the medium with particles through the microfluidic chip. The used amount of flow determines how fast the particles pass the electrodes. This should be sufficiently low to allow for accurate measurements.

Chapter 4

Materials & methods

This chapter first discusses the materials that are used to perform the experiments. Hereafter, the section methods discusses the fabrication of the microfluidic chip and the plan of action of the performed experiments.

4.1 Materials

The materials that are used can be subdivided into fluids, particles, measurement equipment and software. These will be discussed in this section.

4.1.1 Fluids

The experiments were performed using two different fluids, demineralized water and anisole. The demineralized water is obtained from the Elga Purelab® Flex providing water with a resistivity of 18.2Ω [75]. Anisole is obtained from Sigmaaldrich [76].

4.1.2 Particles

In the experiments, two types of particles are used: polystyrene particles and FCC particles. Plain organic 80 micron polystyrene particles where obtained from microspheres-nanospheres [77]. The different metallization stages of FCC particles where obtained by density sorting into 4 categories: fresh, LML, MML and HML [1], [78]. In the experiments, only the fresh and HML stages where used.

4.1.3 Equipment

The signal generation and the lock in amplifier functionality are performed by the HF2IS Impedance Spectroscope. The impedance spectroscope is capable of generating two anti-phase signals, while simultaneously measuring the system output with high accuracy [79]. A NEMESYS syringe pump from Cetoni GMBH is used with one

base module and three 290N modules are used [80]. As power supply the Delta electronics Dual power supply E018-0.6D is used. For the video capture, the point grey grashopper 3, gs3-u3-23s6m-c is used [81]. The Schott KL1600 LED is used as light source [82]. The microfluidic chip is placed in a side-connect chipholder designed by micronit [83]. For the current amplifying circuit the OPA 2107 is used as operational amplifier [84]. For the cyclic voltammetry, the sp-300 potentiostat by biologic is used [85].

4.1.4 Software

Modelling is done using Matlab R2016a and COMSOL multiphysics 5.3 [52], [86]. To control the syringe pump, the software neMESYS UserInterface is used [80]. For video capture, the program grey flycapture2 is used [81]. Data analysis is done using Matlab R2016a and ImageJ [86], [87]. Th program to control the potentiostat is EC-LAB V11.16 [88].

4.2 Methods

4.2.1 Chip fabrication

The microfluidic chip is fabricated using standard microfabrication processes in the MESA+ Nanolab cleanroom facilities. The design of the chip is based on the available technology and previous work. A detailed process flow is included in App. B. The masks that were used in this process are shown in App. C.

The general production steps are summarized in Fig. 4.1. As starting point of the manufacturing process, a Borofloat glass wafer is used. First, electrodes have to be deposited on top of this wafer, as done in steps 1-6. To be able to pattern the metallic layer, the lift-off process is used. This requires that, before the metal is deposited, first a layer of Olin photoresist is deposited. This layer is then patterned using photolithography by the EV620 Mask aligner. After development the patterns are present in the photoresist layer. On top of this layer the metal can be deposited by sputtering using the Tcoathy. Lift-off will then ensure the patterning of the deposited electrodes. These steps are done for both the top and bottom wafer, with a different pattern for each wafer.

To create side-walls of the microfluidic channel, a layer of SU-8 is deposited. This is only done for the bottom wafers in steps 7-9. Due to the large height of the channel, a thick layer of SU-8 is required. In order to create a flat surface of the SU-8, which is required for the bonding process, two separate layers of SU-8 are deposited after another. First a thick layer of around 200 micron is deposited and pre-baked, hereafter

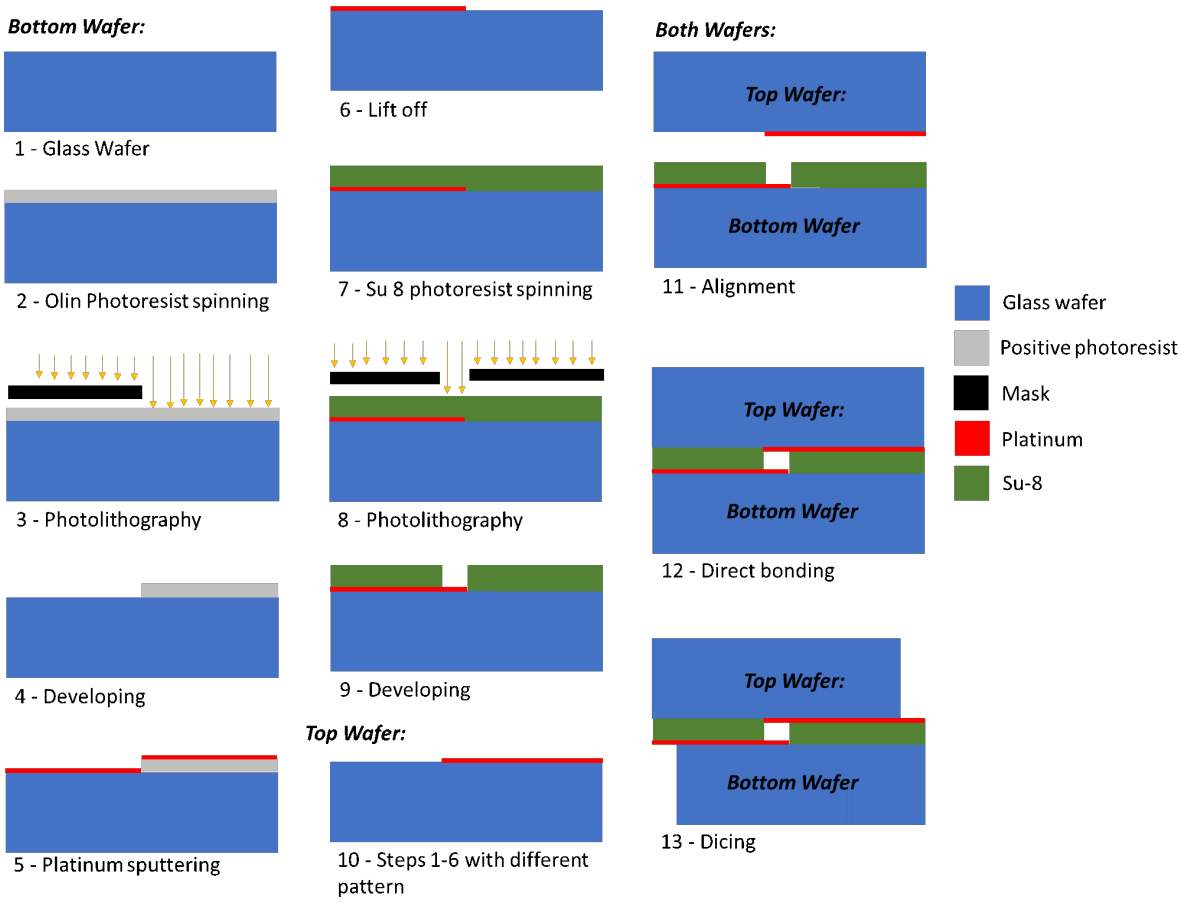

Fig. 4.1: Simplified manufacturing steps that are used in the process of the microfluidic chip

a layer of approximately 30 micron is deposited. The SU-8 is also patterned by photolithography and hereafter developed to form the channels.

The next step is to bond the bottom and upper wafer to enclose the channel. After mask alignment in the EV620 Mask aligner in step 11, the bonding is done is done by the Anodic bonder EV-501. Finally, dicing is performed to separate the chips on the mask and to create connections to the electrodes. For this, the Dicing Saw Disco DAD 321 is used.

4.2.2 Plan of action

Before the system can be used in the detection of the impedance of FCC particles, the system behaviour is verified. First, optimum driving voltage of the system is determined while using anisole as medium. This is done by connecting both ends of the capacitor C_{sig} to the SP300 potentiostat. A cyclic voltammogram is made by sweeping the applied voltage and measuring the resulting current. This is done to check at whether electrochemical reactions will occur, and at which applied potential.

Hereafter, the complete lock-in architecture system is connected to the chip and

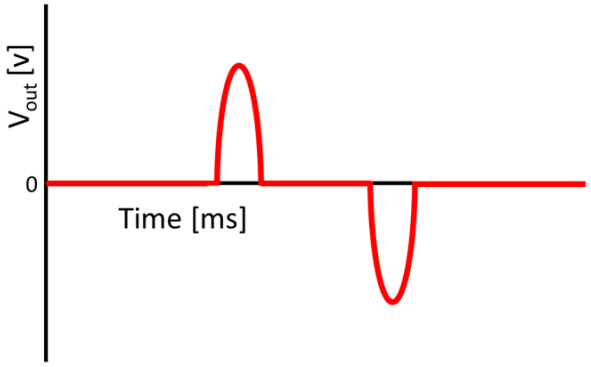

Fig. 4.2: The expected signal whenever a bubble or polystyrene particle passes capacitor C_{sig} first and shortly hereafter capacitor C_{ref}.

the stability of the output is tested. This is done by flowing pure anisole through the microfluidic channels. When this fluid continuously flows through the chip, the electrical properties of the fluid should not change and the measured system impedance should be constant. However, due to several effects, like noise in the system and small dielectric variations in the fluid, the output will not be exactly stable. From the variation in output signal, an indication is given for the resolution of the experiments. The potential at which the measured noise is lowest, is used in following experiments.

The next step is to let the chip generate air bubbles and check whether these bubbles are measured by the system. This is done by adding some air to the syringes. Due to the differential measurement, the peaks when the bubble passes the first and second set of electrodes will be different. The expected signal whenever a bubble passes the electrodes is shown in Fig. 4.2. As a bubble has a dielectric constant of 1, which is lower than the dielectric constant of anisole, it will reduce the capacitance of the electrode it passes, as can be derived from Eq. 2.2.

When the bubble passes the first capacitor of Fig. 3.4, the capacitance C_{sig} decreases. According to Eq. 3.5, this will result in an increase in measured voltage. When the bubble passes the second capacitor, C_{sig} decreases and a negative peak can be expected.

The next step is to flow particles through the chip. First, some 40 micron polystyrene particles are measured with the system. This is done for further system verification. The medium as used in this experiment is again anisole. The dielectric constant of polystyrene is 2.56 and the dielectric constant of anisole is 4.33 [50], [89]. The particles will thus lower the capacitance of the electrodes whenever they pass by. The observed peaks should therefore again look like Fig. 4.2. By using the model of Tao Sun, an estimation can be made for the expected capacitance change. Using Eq. 3.5 it can be checked whether the observed peak meets the expectations. The same particles are also tested with demineralized water as medium for further characterization. Again, the measured capacitance can be compared to theory.

Finally, the capacitance of FCC particles is measured. A comparison is made between the capacitance of fresh and deactivated particles, for which HML particles are used as they show the largest difference in impedance. To do this, a large amount of particles from each group is measured. As the size of the particle has a large influence on the measured capacitance, this size is measured during experiments by video analysis. The total measured capacitance of a particle is expected to be linearly related to the particle volume. As the particles are assumed to be spherical, the volume is related to the cube of the radius. Therefore, a fitting of the measured data is made with respect to the cube of the radius. Separate fits will be made for fresh and aged particles, which will be compared to theory.

Chapter 5

Results and discussion

In this chapter, the results of experiments are discussed. An image of the microfluidic chip, which is used for experiments, is shown in Fig. 5.1. This shows the electrodes that are used for the differential measurements and a microfluidic channel in the horizontal direction. The chip is placed inside a microfluidic holder and electrical connections are soldered to the chip.

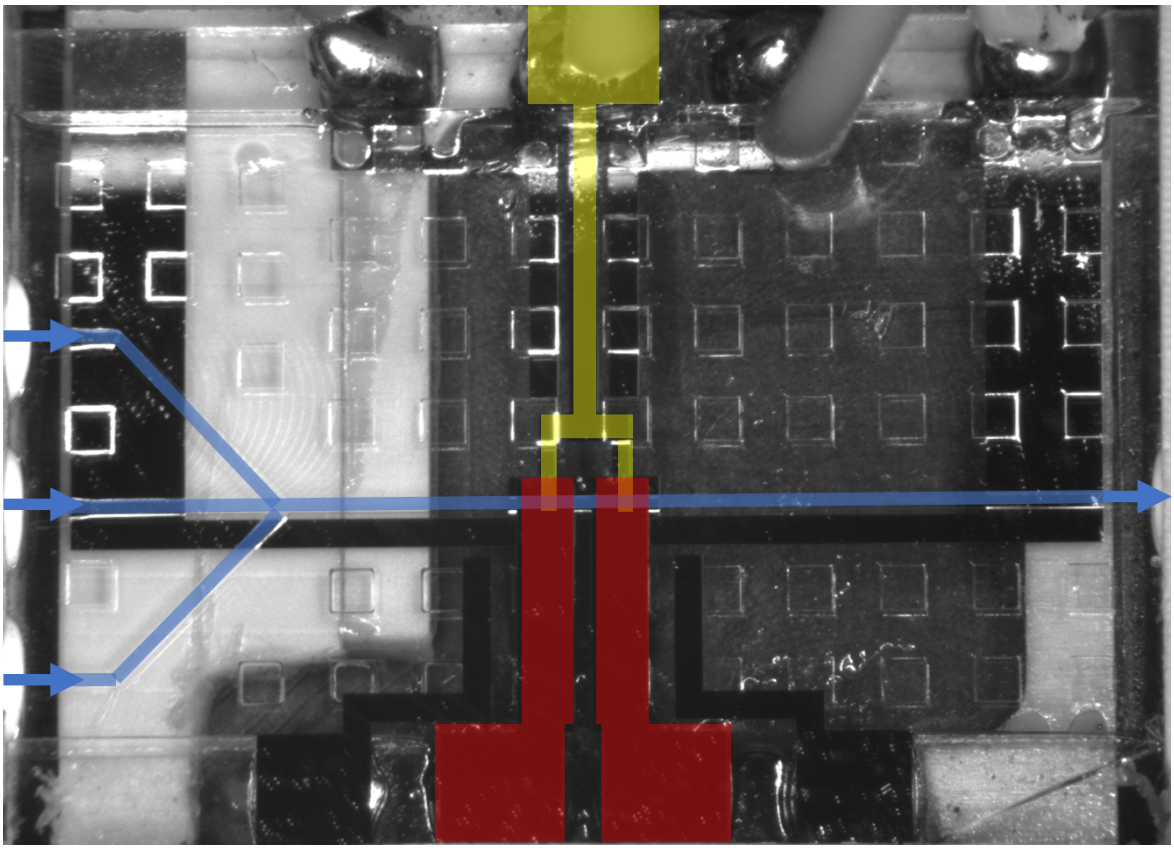

Fig. 5.1: Image of the chip made using the Point Grey Flycapture2. The most important chip elements are marked. In red the input electrodes are shown, in yellow the output electrode and in blue the microfluidic channel is indicated. The arrows indicate the direction of the flow.

A cyclic voltammogram is made of the chip with anisole as medium to check the current-voltage relation. This gives an indication of electrochemical reactions that are occurring at certain potentials. The result of the cyclic voltammetry is presented in Fig. 5.2. This shows that there is some small peak at a potential of 1.5V. This indicates that there might be some reaction happening when the potential is 1.5V and higher. This reaction could increase the amount of noise that is measured by the system. However, since measuring with a higher potential decreases the influence of noise in the electronics, measuring at high potentials could still be optimal.

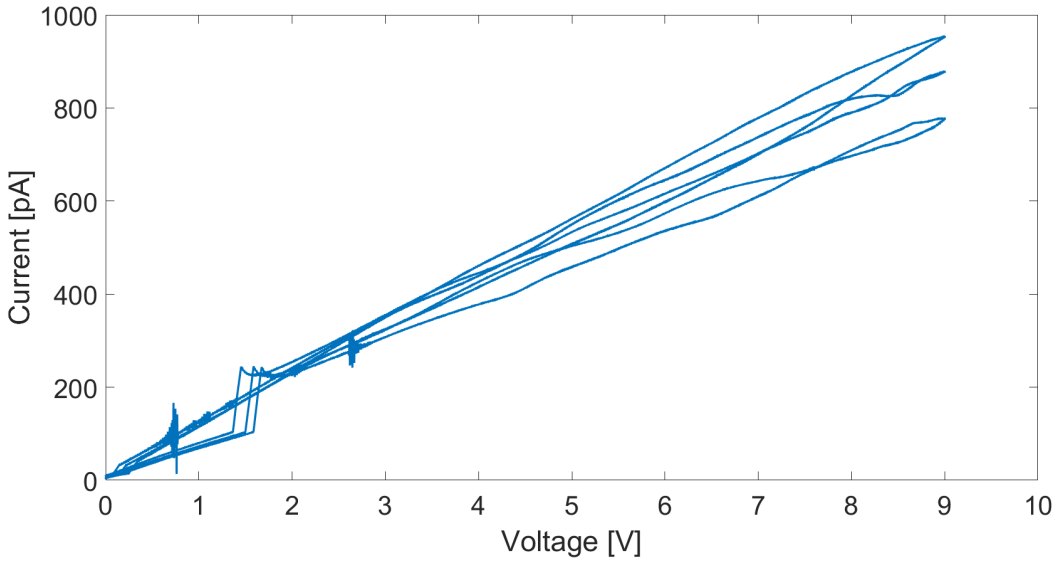

Fig. 5.2: Cyclic voltammogram of anisole showing the measured current, while applying voltage sweeps from 0 till 9 Volts.

The next step is to check the optimum driving potential of the measurement set-up. For this, the complete set-up is connected and used to analyse the amount of noise that is present in the system. This noise is caused by thermal fluctuation, small system variations over time, other unwanted effects and possibly by electrochemical reactions. These measurements show that the amount of noise is minimum when using a high potential. Therefore 9 volts will be used in experiments. A measurement made with the system, while pure anisole, without any particles, is flowing through the channel. The result is shown in Fig. 5.3. This shows that fluctuations of about 0.02mV are present in the measurement. With the maximum amount of fluctuations of the output voltage, the theoretical resolution can be calculated by using Eq. 3.5. According to these calculations, the noise level of the system, while using anisole as medium, is 6.3aF. This value is slightly lower than the expected change in impedance, due to FCC ageing, which is between 7-12aF according to Sec. 2.3.2.

The second system verification step is to measure air bubbles in anisole. The results of such a measurement is shown in Fig. 5.4. The input signal voltage for this experiment is again 9V. The passing of air bubbles results in a large peaks in

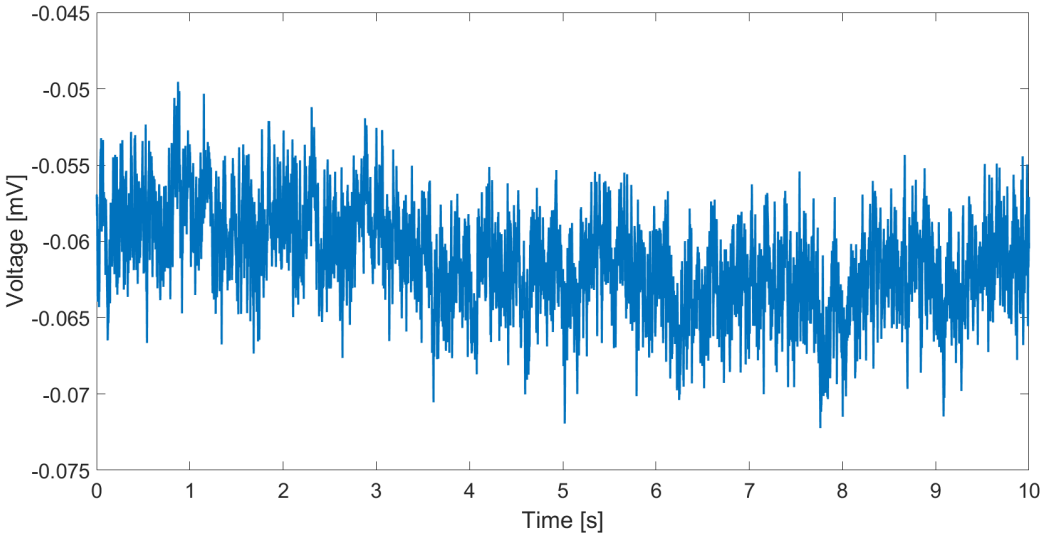

Fig. 5.3: Result of noise analysis measurement, where anisole without particles is flown though the chip. The variations in measured voltage are caused by noise. The estimate noise level from this measurement is 6.3aF.

output voltage. The peaks have the expected shape of Fig. 4.2. As expected, the positive peak is observed first and some time hereafter, a negative peak appears. This experiment shows that the system works as expected for large bubbles which result in a high change in system properties. Using Eq. 3.5, the expected change in impedance due to the bubbles is 5.885fF. This is much larger than the expected change as caused by FCC particles and the bubbles are much larger in size as well. Therefore, a second system verification measurement is performed with polystyrene particles.

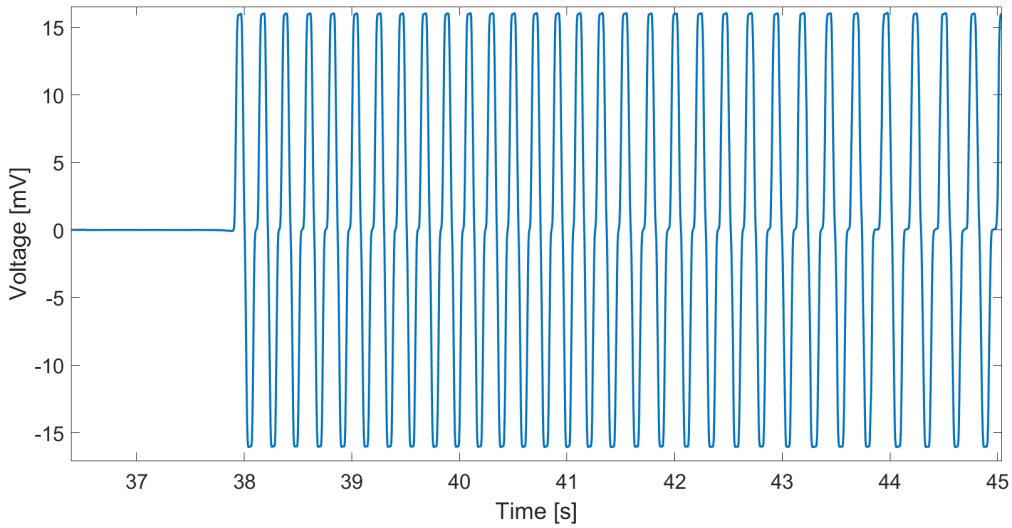

Fig. 5.4: Results of measurements where large air bubbles in anisole are passing the electrodes, showing large peaks in measured voltage.

Small Polystyrene particles are measured in anisole to further verify the system. The expected capacitance that is measured is in the range of 10-20aF, which is around

the expected change in capacitance for FCC particles. Whether these polystyrene particles can be detected while using anisole as medium, thus validates the FCC experiments. Typical data the lock-in architecture for the passing of a polystyrene particle, is shown in Fig. 5.5.

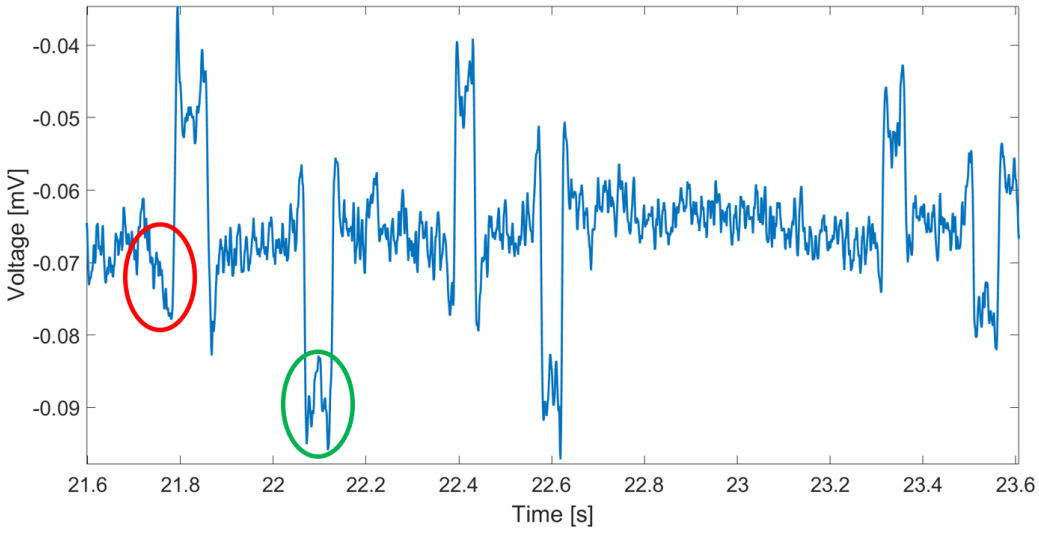

Fig. 5.5: Example of measurement data from the lock-in architecture, while measuring 3 polystyrene particles in anisole as medium. Highlighted are some unexpected features, in red the reverse peak and in green the shape of the peak.

As can be seen from this figure, the peaks are clearly visible and larger than the present noise. There are two features of the peak shape that are remarkable and highlighted in the figure. The first feature is the reverse peak as shown in red, which is observed before and after each large peak. The second feature is shown in green and is the shape of the peak. The peak height is, unlike expectations, not maximum whenever the particle is exactly in the middle. Instead the maximum are observed whenever the particle is near the edges of the electrodes.

The reason for the shape of this peak is expected to be the influence of the particle on the electric field lines of the sensor. The particle has a different dielectric constant from the medium and will therefore cause bending of the field lines. This is made visible in Fig. 5.5, where the difference in dielectric constant between particle and medium is increased to make the effect more visible. Some additional images are shown in App. D, for multiple positions. Furthermore, both the scenario where the particle has a lower and higher dielectric constant, compared to the medium, is shown. Due to lack of time, it was not investigated in more detail how this will exactly influence the peak shape.

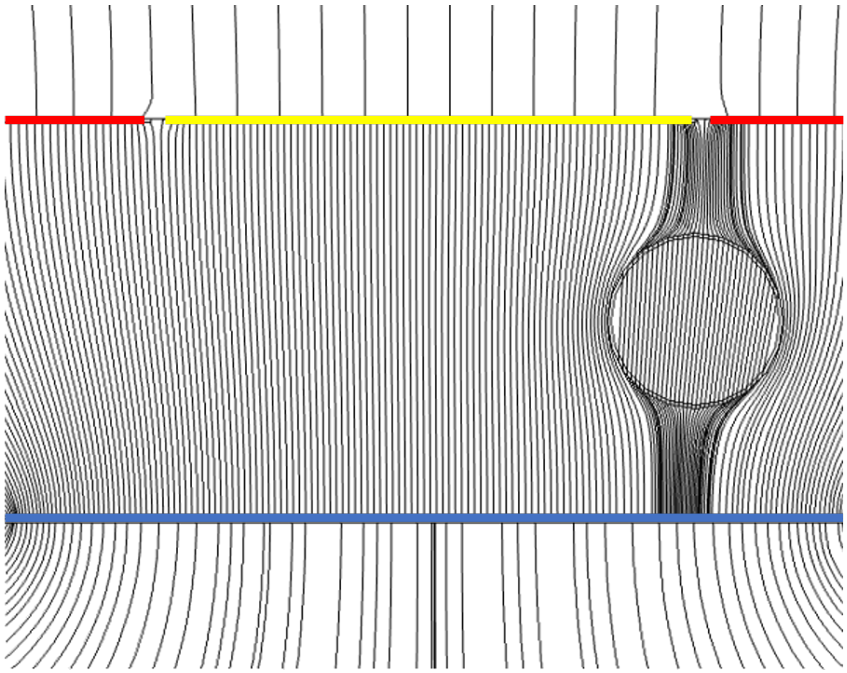

Fig. 5.6: Electric field line bending of particle due to differences in dielectric constants. Exaggerated by using a particle dielectric constant of 4.33 and a medium dielectric constant of 30. In the figures, the yellow line represent the top electrode, the blue line the bottom electrode and the red lines the ground electrodes.

From the measurement of the polystyrene particles, the height of the peaks gives an indication for the measured capacitance. The size of the particle will have influence on the measured capacitance. Therefore, the size is measured by video analysis. During the experiments, some videos are made to estimate the size of each measured particle. A capture of such a video is shown in Fig. 5.7. In this figure, the most important features are highlighted. These are: the channel wall, the electrode, the particle and the direction of flow. The video analysis is combined with the lock-in architecture data to obtain Fig. 5.8.

In this plot, the blue points represent measurement data of the polystyrene particles. The red points indicate the expected values due to simulations. There is some difference between simulation and measured data. This could be caused by differences between the expected and real dielectric constant of both anisole and polystyrene. As the dielectric constant is dependent on frequency, the values obtained from literature could be different from reality. Furthermore, this could be caused by errors in the size estimation of particle and by noise which is present in the system.

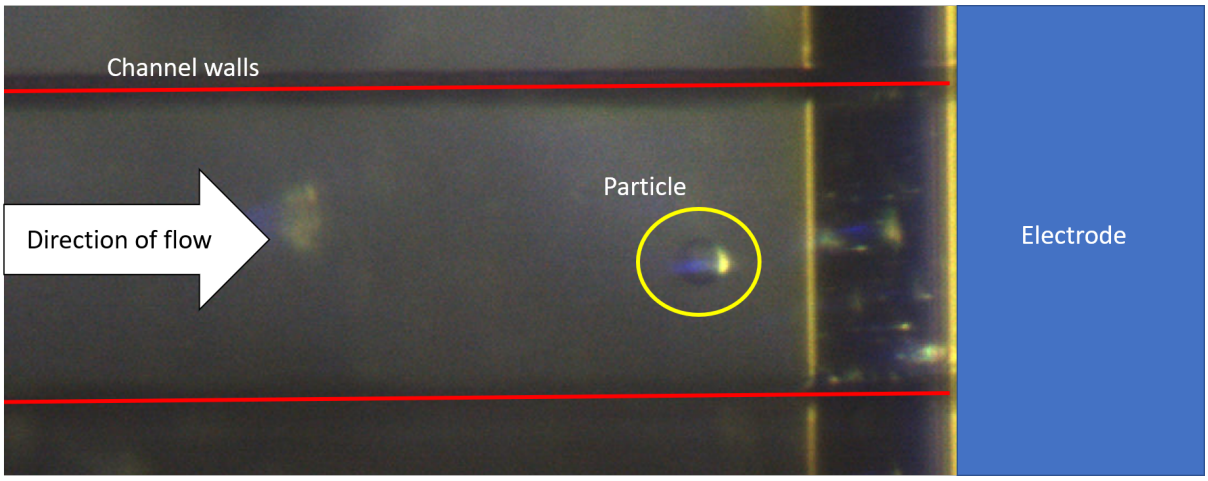

Fig. 5.7: Capture of video analysis to estimate the particle size. The most important features of this image are marked. A pixel in this image equals around 0.95 micron.

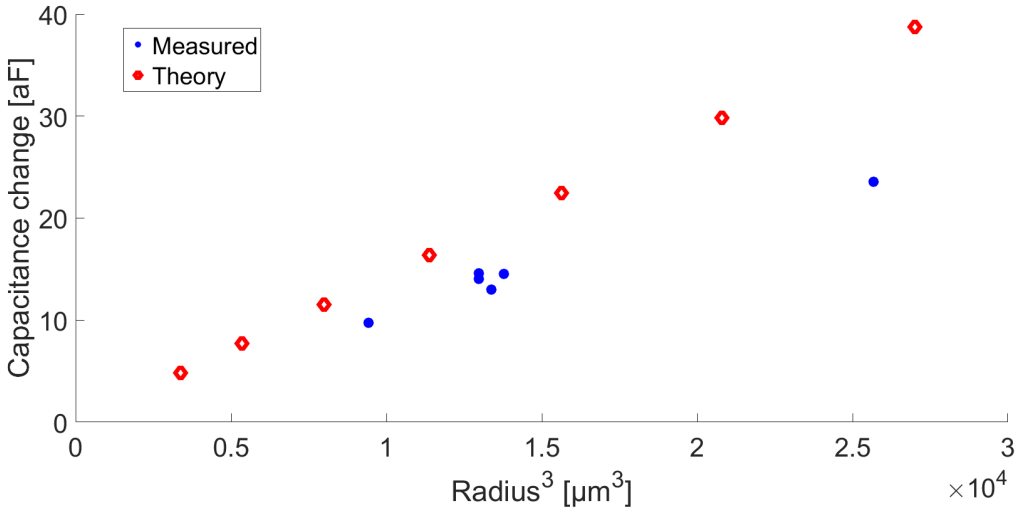

Fig. 5.8: In blue the results of measuring 6 polystyrene particles with anisole as medium is shown. The red dots represents the expected values due to simulations.

These same polystyrene particles are also measured in demineralized water. As this medium has a larger dielectric constant than anisole, 29.3 instead of 4.33, the peaks are expected to be larger compared to the previous experiments. The result of the polystyrene particle measurement in demineralized water is shown in Fig. 5.9. In this case, demineralized water is used as fluid. The potential applied to the system is lowered to 1V, to avoid electrochemical reactions to occur. Again the change in dielectric constant of the system can be clearly observed. However, the peaks are in the reverse order. This would imply that the demineralized water has a lower dielectric constant than water, which is not the case. It is a possibility that during this experiment the positive and negative input voltages are connected reversely.

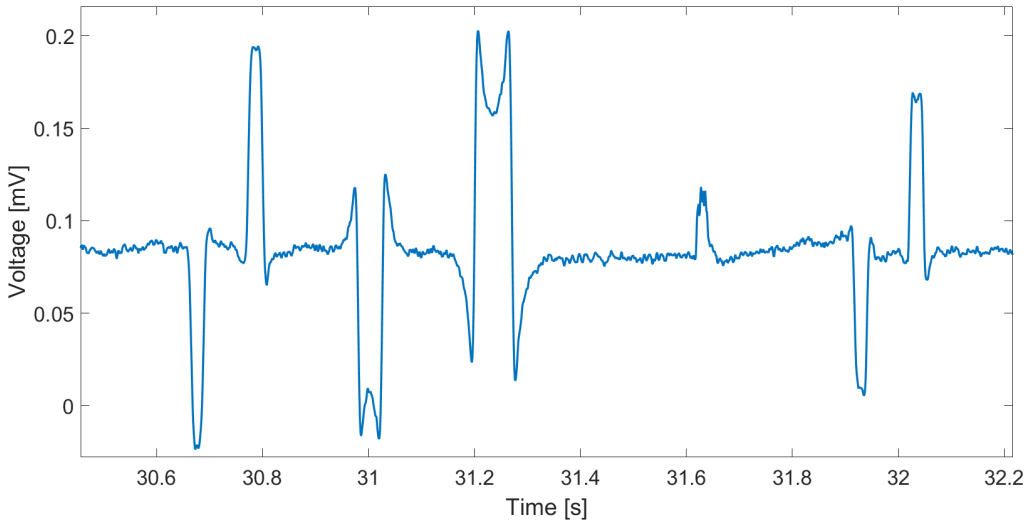

Fig. 5.9: Example of measurement data when detecting polystyrene particles with demineralized water as medium.

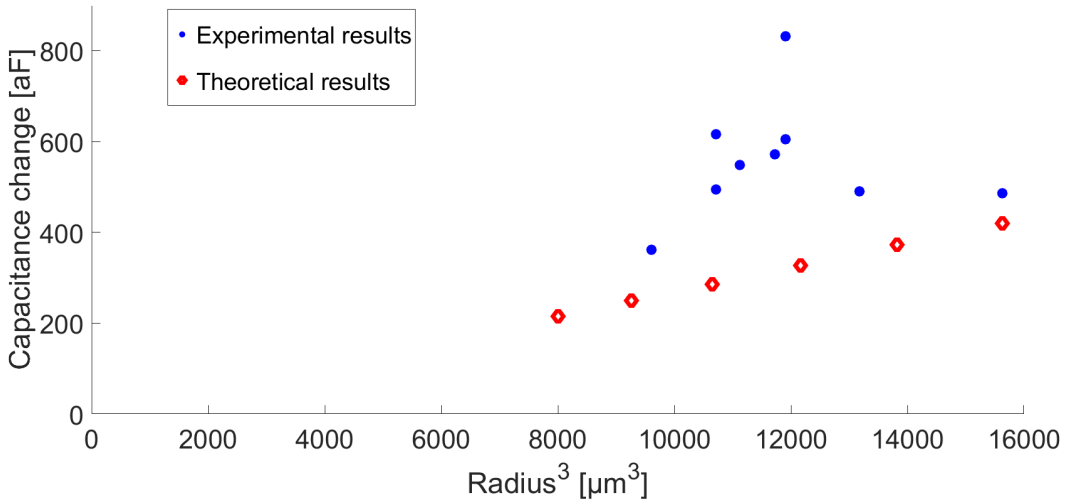

Fig. 5.10:

When plotting the data from these experiments, similar to the analysis as done with polystyrene in anisole, Fig. 5.10 is obtained. This shows capacitance changes which are larger than expected. Furthermore, there is a much larger spread in measured capacitance compared to Fig. 5.5. Some new experiments should be performed to investigate what is happening and whether some errors were made while performing this measurement. Due to time constraints, these experiments could not be performed within this research. As the experiments with polystyrene particles in anisole showed promising results, it is assumed that the system works as expected.

It thus seems that the system is working as expected and the next step is to measure FCC particles. As mentioned in Sec. 4.2.2, the used FCC particle are divided into two groups: fresh and deactivated. A sample of a measurement result is shown in Fig. 5.13. This shows that there is quite a large variation in peak height. The peak height is however also dependent on the size of the particles. Therefore, the particle size was observed by filming the particles during the experiments using the Point Grey Flycapture2. Video captures are shown in Fig. 5.11 and Fig. 5.12.

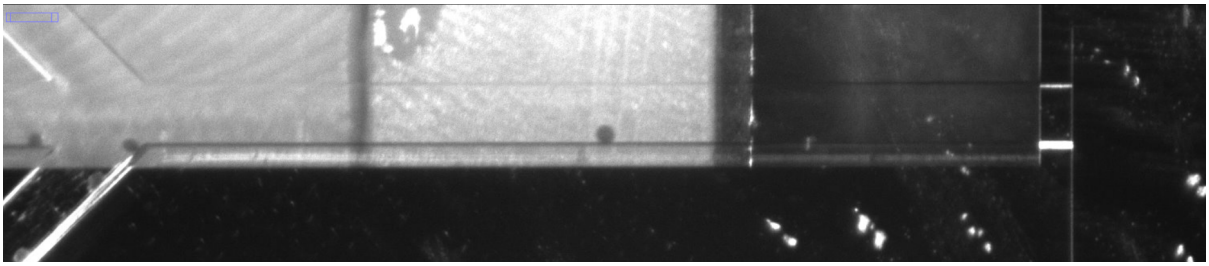

Fig. 5.11: Capture of video analysis of FCC showing the channel which includes a particle. In this figure each pixel represents a size of 3.5 micron.

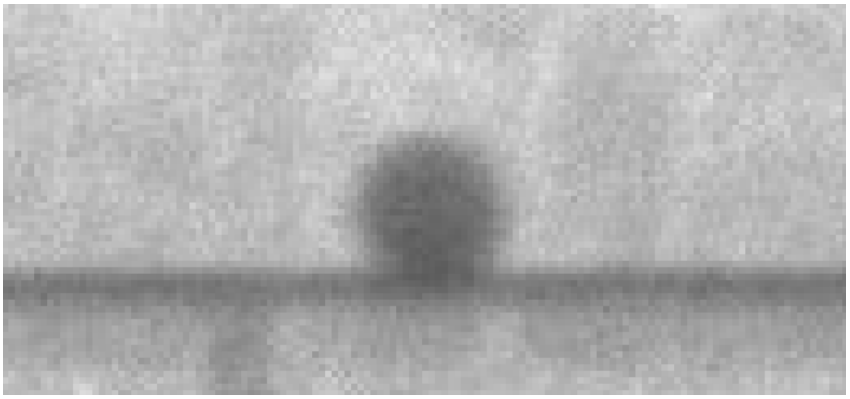

Fig. 5.12: Zoomed image of Fig. 5.11, where the particle is shown in more detail. Each pixel represents 3.5 micron.

As shown in Fig. 5.13, the peaks are clearly distinguishable from the surrounding noise. Around 40 particles are measured for each group. By video analysis, an estimate of the size of each particle was made. The results of this analysis is shown in Fig. 5.14. In this figure, each dot represents a single measured particle. The red and blue trend lines that are shown are obtained by fitting the data to the function of Eq. 5.1.

$$C_{meas} = a \cdot r^3 \tag{5.1}$$

Where r is the radius of the particle in [µm], C_{meas} the measured capacitance in [aF] and a is the fitted parameter according to the curve fitting tool in Matlab in [[aF/µm^3].

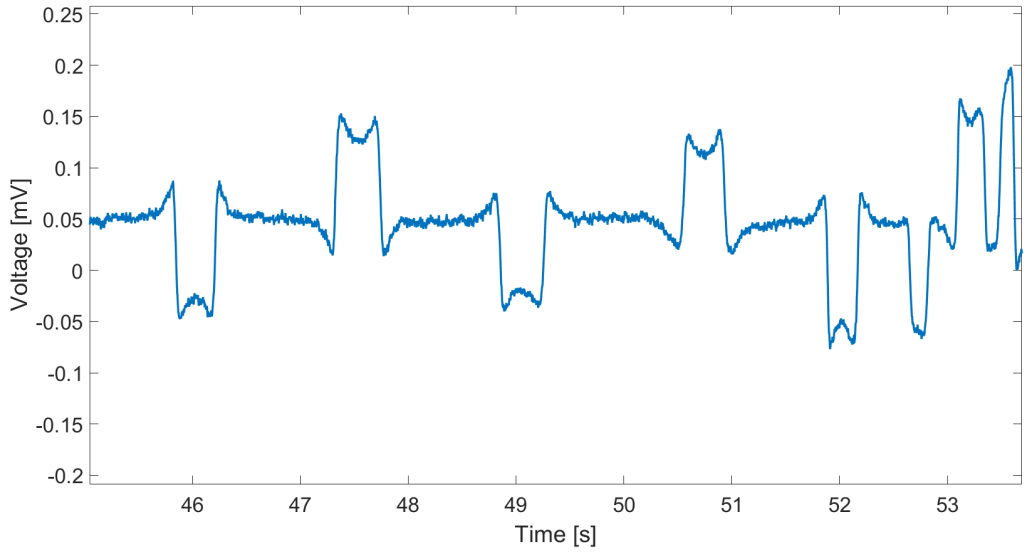

Fig. 5.13: Example of a measurement result, where FCC particles are passing the electrode. In the experiment, anisole is used as medium.

The fitted values of a for fresh and deactivated particles are shown in Eq. 5.2 and Eq. 5.3 respectively.

$$a_{fresh} = 1.094 \cdot 10^{-3} \tag{5.2}$$

$$a_{deactivated} = 1.414 \cdot 10^{-3} \tag{5.3}$$

The graph clearly shows that the measured capacitance is not only depending on the radius of the particle. The spread due to other effects is more significant than the changes in capacitance due to metal accumulation. The size estimation and voltage measurement will introduce errors due to the pixel size of the video capture and the noise present during measurement. The spread in measured capacitance is however much larger than the expected spread due to these influences. The cause of the large deviation is expected to be the heterogeneity of the FCC particles. The model, that was made in Chap. 2, assumed the average composition of the particle that was provided by the supplier. It is however expected that the composition is not identical for each particle and large variations in composition are possible. As the dielectric constant of the particle is depends on the exact composition, heterogeneity of the composition is thus likely to cause the observed spread in measured capacitance. Because of the large spread, the fitting that was made has a low coefficient of determination. Therefore, it is not possible to conclude from the capacitance measurement of a single particle what the particle activity is. However, the average of the measurements can still give some relevant information. As can be seen from the fitting curves, on average the deactivated particles have a larger capacitance. According to these curves, the difference between fresh and deactivated particles, with a radius of 40 micron, is

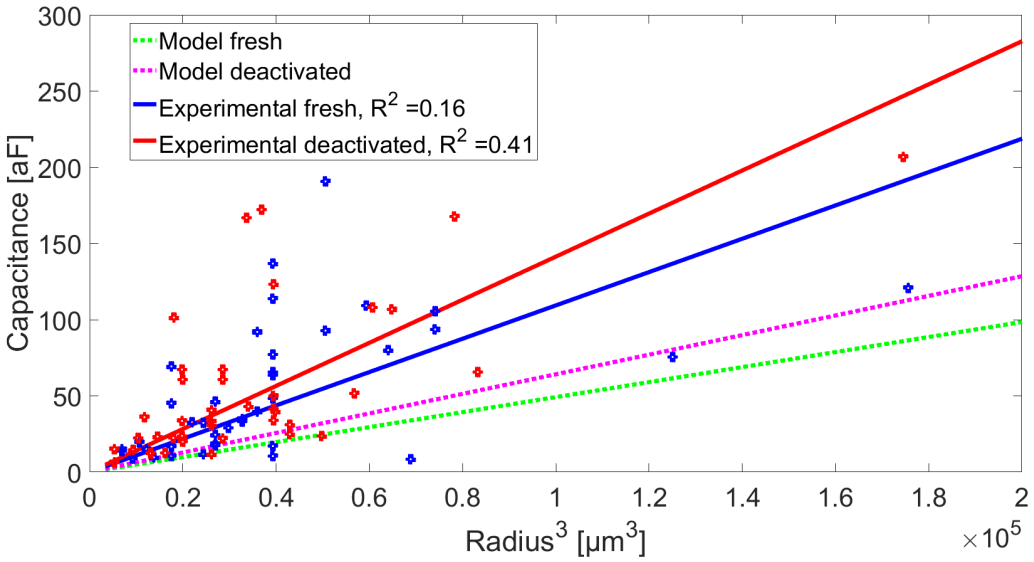

Fig. 5.14: Experimental result of both fresh and deactivated FCC particles. The peak height as measured by the system is plotted versus the particle diameter as estimated by video analysis. Several trend lines are added to this figure, using both the experimental data and the results from the Tao Sun model. For the experimental data, the coefficient of determination (R^2) is indicated.

20.5aF. This is larger than the expected difference obtained from modelling, which is around 10aF. Although more particles should be measured to confirm the difference between the averages of fresh and deactivated particles, the average impedance of FCC could potentially be used to identify groups of particles with reduced activity.

It is expected that the deviation between model and experiments is caused by the used dielectric constants in the model. The dielectric constant is dependent on the frequency and the exact form for which the molecule is present and will likely differ from the values found in literature. For example, Iron oxide can be present in three forms: Hematite, Maghemite and Magnetite, for which the dielectric constant can have values between 20.6 and 81 [34], [90]–[92]. In the model, the lowest dielectric constant is used to avoid overestimating the expected capacitance. Differences between experiments and the model are also caused by model simplifications and the low number of measurements that are performed. In the figure, measurement data of around 40 particles of each group is shown. Due to this low number of measurements, results of single particles will have a large impact on the final fitted curve. Therefore, more particles should be measured to give improve the averages that are obtained.

From the fitted lines, also an estimate can be made for the average dielectric constant of the particle. This is done using the Tao Sun model. The fresh and deactivated particles have an estimated average dielectric constant of 6.1 and 6.7 respectively. This is higher than the expected values according to Tab. 2.6. This difference is again expected to be caused by difference between the actual dielectric constant and the

expected one from literature. Furthermore, there are some inaccuracies in the model, like ignoring the contributions of Sodium, Potassium and difosforpentoxide for reasons mentioned in Sec. 2.2. The purpose of the model was to give an estimate for the expected dielectric constant and not to match reality, which was not possible due to the limited information about FCC particles.

Overall, the experiments show that the designed lock-in architecture is able to measure dielectric changes in FCC particles with sufficient accuracy. The heterogeneity in FCC particle composition avoids a direct relation between the activity and the measured capacitance of single particles. Nevertheless, a difference of 20.5aF can be observed for particles with a radius of 40 micron, when using the average results of 40 fresh and deactivated particle experiments.

Chapter 6

Conclusions

The research as presented in this thesis is performed to show the correlation between the activity and the impedance of FCC particles. Literature indicates that the FCC particle activity is related to accumulation of material, in specific the oxides of Fe, Ni and V. Several models are used to estimate the effect of this accumulation, on the impedance. The 2D electric network model estimates an average dielectric constant for fresh particles of 5.1. This is predicted to increase to 5.65 for the particle outer shell and to 5.26 for the inner volume. The change is expected to be largest for the outer shell as literature indicates that most material is accumulated in this region. Three models are used to estimate the system impedance of the microfluidic chip. These models are also used to optimize the measurement system. From the Tao Sun model is concluded that measuring the high frequency capacitance is optimum. Furthermore, the model shows that the dielectric constant of the medium should be close to the FCC particle dielectric constant. Although this will not result in the largest capacitance change due to metal accumulation, it will reduce the dependence of the measured impedance on the particle size significantly. The models show that when using anisole as medium, ageing of FCC will cause an increase in capacitance between 7 and 12aF for particles with a radius of 40 micron. To detect this small difference in capacitance, a lock-in architecture is used. The main advantages of this design are the high sensitivity and short measurement time. Furthermore, it is relatively easy to incorporate differential measuring into this design. The noise level when using this system is around 6.3aF when using anisole as medium. The system is verified for anisole as medium by measuring both bubbles and polystyrene particles, which show expected system behaviour. Experiments with fresh and deactivated FCC particles show that the capacitance variations for particles of the same category are more significant than the capacitance variations due to metal accumulation. Capacitance measurements of single particles can therefore not be used to classify them into either group. The averages of 40 fresh and deactivated FCC particles does show an increase in capacitance. Although more particles should be measured to verify this difference, the average impedance of FCC could potentially be used to identify groups of reduced activity.

Chapter 7

Recommendations

The research as presented in this thesis can still be improved. In this section, these improvements are discussed. These improvements are required to optimize the experimental set-up and to increase the understanding of the obtained results.

The size estimation of the particle should be improved. This can be done by using a improved set-up, where the size resolution is increased. This will still only give a 2-dimensional image of the particle, while the complete volume is wanted. A further improvement would be to measuring the resistance and capacitance simultaneously. The particle resistance will not change due to metal accumulation and is thus a good indication for the particle size. With this technique, the opacity is measured instead of the capacitance. This will reduce the errors made in the size estimation of the particle.

The shape of the peaks should be analysed in more detail to improve the understanding of the measurement results. This can be done by performing additional COMSOL simulations, which calculate the capacitance of the particle at multiple positions. The ground electrodes should be added in the calculations of the capacitance as this is expected to have an effect on the peak shape.

The bandwidth as used in the experiments should be optimized. Currently a bandwidth of 100Hz is used to be able to properly measure both fast and slow moving particles. By better control of the particle velocity, the bandwidth can be adjusted to this specific velocity. Reducing the measurement bandwidth will decrease the amount of noise in the system.

The difference in molecular content of FCC particles, which belong to the same activity group, should be investigated in detail. It is expected that the large spread in measured capacitance is caused by these content differences and that the particle information as provided by the supplier are averages. The differences in molecular content can be used in the models that were made. The models can then give an estimate for the expected spread in measured capacitance due to the heterogeneity in molecular content. This can then be compared to the measured values.

Furthermore, the device dimensions and the used medium can be optimized. The height of the microfluidic channel should be decreased to increase the sensitivity of the chip. To do this, it should first be checked what the minimum height of the channel

is before clogging becomes a problem. This height should be used to obtain maximum sensitivity. Furthermore, a medium with a dielectric constant even closer to the dielectric constant of fresh FCC particles should be used. This is expected to reduce the effect of the particle size on the measured impedance.

Chapter 8

Acknowledgements

Bibliography

[1] F. Meirer, S. Kalirai, D. Morris, S. Soparawalla, Y. Liu, G. Mesu, J. C. Andrews, and B. M. Weckhuysen, “Life and death of a single catalytic cracking particle,” *Science Advances*, vol. 1, no. 3, 2015.

[2] G. Yaluris, W. C. Cheng, M. Peters, L. T. McDowell, and L. Hunt, “Mechanism of fluid cracking catalysts deactivation by fe,” *Elsevier*, 2004.

[3] W. G. Appleby, J. W. Gibson, and G. M. Good, “Coke formation in catalytic cracking,” *Industrial and Engineering Chemistry Process Design and Development*, 1962.

[4] A. Mohamadalizadeh, J. Towfighi, and R. Karimzadeh, “Modeling of catalytic coke formation in thermal cracking reactors,” *Elsevier*, 2008.

[5] H. S. Cerqueira, G. Caeiro, L. Costa, and F. R. Ribeiro, “Deactivation of fcc catalysts,” *Elsevier*, 2008.

[6] E. T. C. Vogt and B. M. Weckhuysen, “Fluid catalytic cracking: recent developments on the grand old lady of zeolite catalysis,” *The Royal Society of Chemistry*, vol. 44, pp. 7342–7370, May 2015.

[7] M. Solsona, A. E. Nieuwelink, F. Meirer, L. Abelmann, M. Odijk, W. Olthuis, B. M. Weckhuysen, and A. Berg, “Magnetophoretic sorting of single catalyst particles,” *Angewandte Chemie*, 2018. [Online]. Available: https://onlinelibrary.wiley.com/doi/abs/10.1002/anie.201804942

[8] T. Sun, C. Bernabini, and H. Morgan, “Single-colloidal particle impedance spectroscopy: Complete equivalent circuit analysis of polyelectrolyte microcapsules,” *Langmuir*, pp. 3821–3828, 2009.

[9] P. Pickering, “Capacitive sensors: An attractive option for contactless sensing,” 2016. [Online]. Available: http://www.electronicdesign.com/analog/capacitive-sensors-attractive-option-contactless-sensing

[10] R. Nave, “Resonance,” 2018. [Online]. Available: http://hyperphysics.phy-astr.gsu.edu/hbase/electric/serres.html

[11] G. A. Ferrier, A. N. Hladio, D. Thomson, G. E. Bridges, M. Hedayatipoor, S. Olson, and M. R. Freeman, “Microfluidic electromanipulation with capacitive detection for the mechanical analysis of cells,” *Biomicrofluidics*, 2008.

[12] J. Tapson and J. R. Greene, “Improved capacitance measurement by means of resonance locking,” *Measurement Science and Technology*, 1994.

[13] Zurich Instruments, “Principles of lock-in detection and the state of the art,” 2016. [Online]. Available: https://www.zhinst.com/sites/default/files/li_primer/zi_whitepaper_principles_of_lock-in_detection.pdf

[14] S. Chen, D. Le, and V. Nguyen, “Inductive displacement sensors with a notch filter for an active magnetic bearing system,” *Sensors*, 2014.

[15] A. Balandin, “The mystery of the 1/f noise,” *Materials today*, 2013. [Online]. Available: https://www.materialstoday.com/carbon/news/the-mystery-of-the-1f-noise/

[16] N. Friedrich, “Revealed: Source of low-frequency 1/f noise,” *Microwaves and RF*, 2013. [Online]. Available: https://www.mwrf.com/semiconductors/revealed-source-low-frequency-1f-noise

[17] R. Kiely, “Understanding and eliminating 1/f noise,” *Analog Dialogue*, 2017. [Online]. Available: http://www.analog.com/en/analog-dialogue/articles/understanding-and-eliminating-1-f-noise.html

[18] A. Konczakowska and B. M. Wiliamowski, “Noise in semiconductor devices,” Fundamentals of Industrial Electronics, 2011. [Online]. Available: http://www.eng.auburn.edu/~wilambm/pap/2011/K10147_C011.pdf

[19] J. Wei, C. Yue, Z. L. Chen, Z. W. Liu, and P. M. Sarro, “A silicon mems structure for characterization of femto-farad-level capacitive sensors with lock-in architecture,” *Journal of micromechanics and microengineering*, 2010.

[20] All about circuits, “Bridge circuits,” 2018. [Online]. Available: https://www.allaboutcircuits.com/textbook/direct-current/chpt-8/bridge-circuits/

[21] Andeen-hagerling, “Ah 2700a.” [Online]. Available: https://www.elliotscientific.com/image/data/pdf/AH2700A_465.pdf

[22] S. Gawad, K. Cheung, U. Seger, A. Bertsch, and P. Renaud, “Dielectric spectroscopy in a micromachined flow cytometer: theoretical and practical considerations,” *Miniaturisation for chemistry, biology and bioengineering*, 2004.

[23] S. Burt, N. Finney, and J. Young, “Fringe field of parallel plate capacitor,” Santa Rosa Junior College Department of Engineering and Physics. [Online]. Available: http://srjcstaff.santarosa.edu/~yataiiya/UNDER_GRAD_RESEARCH/Fringe%20Field%20of%20Parallel%20Plate%20Capacitor.pdf

[24] K. P. P. Pillai, “Fringing field of finite parallel-plate capacitors,” *IEEE*, 1970. [Online]. Available: https://ieeexplore.ieee.org/stamp/stamp.jsp?tp=&arnumber=5248728

[25] Imperial college, “Noise,” Imperial college, 2008. [Online]. Available: http://cas.ee.ic.ac.uk/people/dario/files/E302/2-noise.pdf

[26] L. B. Kish, “Thermal noise engines,” Texas A and M University, Department of Electrical Engineering, 2010. [Online]. Available: https://arxiv.org/ftp/arxiv/papers/1009/1009.5942.pdf

[27] T. Gupta, *Copper interconnect technology*. Springer, 2009.

[28] Azom, “Silica - silicon dioxide sio2.” [Online]. Available: https://www.azom.com/article.aspx?ArticleID=1114

[29] Massachusetts Institute of Technology, “Material: Aluminum oxide,” Material Property Database. [Online]. Available: http://www.mit.edu/~6.777/matprops/alox.htm

[30] R. A. Bartels and P. A. Smith, “Pressure and temperature dependence of the static dielectric constants of kc1, nac1, lif, and mgo,” *PHYSICAL REVIEW B*, vol. 7, no. 8, pp. 3885–3892, 1973.

[31] Azom, “Magnesia - magnesium oxide (mgo) properties and applications.” [Online]. Available: https://www.azom.com/properties.aspx?ArticleID=54

[32] A. Wypych, I. Bobowska, M. Tracz, A. Opasinska, S. Kadlubowski, A. Kaliszewska, J. Grobelny, and P. Wojciechowski, “Dielectric properties and characterisation of titanium dioxide obtained by different chemistry methods,” *Journal of Nanomaterials*, 2014.

[33] Azom, “Titanium dioxide - titania (tio2).” [Online]. Available: https://www.azom.com/article.aspx?ArticleID=1179

[34] S. Onari, T. Arai, and K. Kudo, “Infrared lattice vibrations and dielectric dispersion in a-fe203,” *PHYSICAL REVIEW B*, 1977. [Online]. Available: https://journals.aps.org/prb/pdf/10.1103/PhysRevB.16.1717

[35] W. Telford, L. Geldart, and R. Sheriff, *Electrical Properties of Rocks and Minerals*. Cambridge University Press, 1990. [Online]. Available: http://crack.seismo.unr.edu/ftp/pub/louie/class/492/data/2011/GPH492_ALL_FILES_2011/AppliedGeophysics_Telford/AppliedGPH_ElectricalPropertiesOfRocksAndMinerals.pdf

[36] Mindat, “Hematite,” 2018. [Online]. Available: https://www.mindat.org/min-1856.html

[37] T. Yamamoto, H. Momida, T. Hamada, T. Uda, and T. Ohno, “First-principles study of dielectric properties of cerium oxide,” *Thin Solid Films*, 2005.

[38] H. Jin, N. Wang, L. Xu, and S. Hou, “Synthesis and conductivity of cerium oxide nanoparticles,” *Materials Letters*, 2010.

[39] Science Lab, “Material safety data sheet cerium (iv) oxide msds,” 2018. [Online]. Available: http://www.sciencelab.com/msds.php?msdsId=9923351

[40] J. H. McCulloch, *The Electrical Properties of Vanadium Pentoxide*. Oregon State University, 1968.

[41] National Center for Biotechnology Information, “Vanadium pentoxide,” 2018. [Online]. Available: https://pubchem.ncbi.nlm.nih.gov/compound/vanadium_pentoxide#section=Top

[42] R. A. Bartels, J. C. Koo, and M. L. Thomas, “The temperature and pressure dependence of the dielectric constants of cao and sro,” *Physica status solidi*, 1979.

[43] N. A. Surplice, “The electrical conductivity of calcium and strontium oxides,” *British Journal of Applied Physics*, 1966.

[44] National Center for Biotechnology Information, “Calcium oxide,” 2018. [Online]. Available: https://pubchem.ncbi.nlm.nih.gov/compound/Lime#section=Top

[45] K. V. Rao and A. Smakula, “Dielectric properties of cobalt oxide, nickel oxide, and their mixed crystals,” *Journal of applied physics*, 1964.

[46] Azom, “Zinc oxide (zno) semiconductors,” 2018. [Online]. Available: https://www.azom.com/article.aspx?ArticleID=8417

[47] T. K. Roy, D. Sanyal, D. Bhowmick, and A. Chakrabarti, “Temperature dependent resistivity study on zinc oxide and the role of defects,” *Materials Science in Semiconductor Processing*, 2013.

[48] M. W. Van der Helm, *Electrical and microfluidic technologies for organs-on-chips, mimicking blood-brain barrier and gut tissues*. University of Twente, 2018.

[49] LookChem, “Physical properties of anisole,” 2013. [Online]. Available: https://www.lookchem.com/topic/Lactic-acid/Dynamic-upstream-and-downstream/634.html

[50] A. A. Maryott and E. R. Smith, “Table of dielectric constants of pure liquids,” *United States department of commerce*, 1951. [Online]. Available: http://www.dtic.mil/dtic/tr/fulltext/u2/a278956.pdf

[51] E. Cheever, “An algorithm for modified nodal analysis,” Swarthmore University. [Online]. Available: https://www.swarthmore.edu/NatSci/echeeve1/Ref/mna/MNA3.html

[52] COMSOL Inc., “Comsol multiphysics 5.3,” 2017. [Online]. Available: https://www.comsol.com/

[53] Schott, “Ultra-thin borosilicate glass,” 2018. [Online]. Available: https://www.us.schott.com/advanced_optics/english/products/optical-materials/thin-glass/mempax/index.html

[54] R. Yang, “Ultra-violet lithography of thick photoresist for the applications in biomems and micro optics,” 2006. [Online]. Available: https://digitalcommons.lsu.edu/cgi/viewcontent.cgi?article=4467&context=gradschool_dissertations

[55] Krohne, “Services dielectric constants,” 2018. [Online]. Available: https://krohne.com/en/services/dielectric-constants/

[56] Elga, “Purelab flex: Pure and ultrapure laboratory water from a single system,” 2018. [Online]. Available: http://www.torontomicrofluidics.ca/cms/manuals/diwater.pdf

[57] D. C. Grahame, “The electrical double layer and the theory of electrocapillarity,” Chemical Reviews, 1947. [Online]. Available: https://pubs.acs.org/doi/pdf/10.1021/cr60130a002

[58] G. Luka, A. Ahmadi, H. Najjaran, E. Alocilja, M. DeRosa, K. Wolthers, A. Malki, H. Aziz, A. Althani, and M. Hoorfar, “Microfluidics integrated biosensors: A leading technology towards lab-on-a-chip and sensing applications,” *Sensors (Basel, Switzerland)*, 2015. [Online]. Available: https://www.ncbi.nlm.nih.gov/pmc/articles/PMC4721704/

[59] A. C. Sabuncu, J. Zhuang, J. F. Kolb, and A. Beskok, “Microfluidic impedance spectroscopy as a tool for quantitative biology and biotechnology,” *Biomicrofluidics 6.3*, 2012. [Online]. Available: https://www.ncbi.nlm.nih.gov/pmc/articles/PMC3407121/

[60] H. J. Lee, S. J. Bai, and Y. S. Song, “Microfluidic electrochemical impedance spectroscopy of carbon composite nanofluids,” *Scientific Reports - Nature*, 2017. [Online]. Available: https://www.nature.com/articles/s41598-017-00760-1

[61] M. P. Schmidt, A. Oseev, C. Engel, A. Brose, B. schmidth, and S. Hirsch, “Flexible free-standing su-8 microfluidic impedance spectroscopy sensor for 3-d molded interconnect devices application,” *Journal of sensors and sensor systems*, 2016. [Online]. Available: https://www.j-sens-sens-syst.net/5/55/2016/jsss-5-55-2016.pdf

[62] R. S. Subramanian, “Pipe flow calculations,” Department of Chemical and Biomolecular Engineering - Clarkson University, 2018. [Online]. Available: http://web2.clarkson.edu/projects/subramanian/ch330/notes/Pipe%20Flow%20Calculations.pdf

[63] MIT, “Reynolds number and pipe flow,” MIT - depeartment of mechanical engineering, 2002. [Online]. Available: https://ocw.mit.edu/courses/mechanical-engineering/2-000-how-and-why-machines-work-spring-2002/study-materials/TurbulentFlow.pdf

[64] M. H. Winer, A. Ahmadi, and K. C. Cheung, “Application of a three-dimensional (3d) particle tracking method to microfluidic particle focusing,” *Lab on a chip*, 2014. [Online]. Available: http://pubs.rsc.org/en/content/articlelanding/2014/lc/c3lc51352a/unauth#!divAbstract

[65] A. Talmon, “basic principles of flow of liquid and particles in a pipeline,” UT Delft, 2016. [Online]. Available: https://ocw.tudelft.nl/wp-content/uploads/B._oe4625_Chapter01.pdf

[66] G. Ahmadi, “Hydrodynamic forces,” Clarkson University, 2018. [Online]. Available: https://webspace.clarkson.edu/projects/fluidflow/public_html/courses/me537/1_2Drag.pdf

[67] M. E. Kurdzinski, B. Gol, A. C. Hee, P. Thurgood, J. Y. Zhu, P. Petersen, A. Mitchell, and K. Khoshmanesh, “Dynamics of high viscosity contrast confluent microfluidic flows,” *Scientific Reports*, 2017. [Online]. Available: https://www.nature.com/articles/s41598-017-06260-6

[68] Elveflow, “Microfluidic cell culture: How to do fast medium and drugs change in a microfluidic device?” 2018. [Online]. Available: https://www.elveflow.com/microfluidic-tutorials/cell-biology-imaging-reviews-and-tutorials/live-cell-perfusion/methods-and-techniques/microfluidic-cell-culture-medium-change/

[69] D. Spencer and H. Morgan, “Positional dependence of particles in microfludic impedance cytometry,” *Lab on a chip*, 2011.

[70] J. Niemann, “Understanding grounding, shielding, and guarding in high-impedance applications,” EDN network, 2013. [Online]. Available: https://www.edn.com/design/test-and-measurement/4407078/Understanding-grounding--shielding--and-guarding-in-high-impedance-applications

[71] R. A. Brookhuis, T. S. J. Lammerink, and R. J. Wiegerink, “Differential capacitive sensing circuit for a multi-electrode capacitive force sensor,”

Sensors and Actuators A: Physical, 2015. [Online]. Available: https://www.sciencedirect.com/science/article/pii/S0924424715301126

[72] J. S. Jaworski, M. Cembor, and M. Orlik, "Anisole as a solvent for organic electrochemistry," *Journal of electroanalytical chemistry*, 2005. [Online]. Available: https://ac.els-cdn.com/S0022072805000331/1-s2.0-S0022072805000331-main.pdf?_tid=2fe5365d-217e-4c3d-baa8-e6b1f16b5075&acdnat=1533121618_d413e3086d8bc89f8c8a96b36c3c997c

[73] National Center for Biotechnology Information, "Anisole," PubChem Compound Database, 2018. [Online]. Available: https://pubchem.ncbi.nlm.nih.gov/compound/anisole#section=Auto-Ignition

[74] Stanford research systems, "Model sr830 dsp lock - in amplifier," 2011. [Online]. Available: https://www.thinksrs.com/downloads/pdfs/manuals/SR830m.pdf

[75] Purelab flex, "Pure and ultrapure laboratory water from a single system," ELGA, 2010. [Online]. Available: http://www.torontomicrofluidics.ca/cms/manuals/diwater.pdf

[76] Sigma-Aldrich, "Anisole," 2018. [Online]. Available: https://www.sigmaaldrich.com/catalog/product/sial/296295?lang=en&region=NL

[77] Microspheres-nanospheres, "Plain polystyrene nanospheres and microspheres," 2018. [Online]. Available: http://www.microspheres-nanospheres.com/Microspheres/Organic/Polystyrene/PS%20Plain.htm

[78] G. R. Dyrkacz, L. Ruscic, and C. L. Marshall, "Appendix c: Constitutive relations," *Energy and Fuels*, 1996.

[79] Zurich Instruments, "Hf2is impedance spectroscope," 2018. [Online]. Available: https://www.zhinst.com/products/hf2is

[80] Cetoni, "Base module base 120," 2018. [Online]. Available: https://www.cetoni.de/en/products/base-module-base-120/

[81] Pointgrey, "Grasshopper 3," 2018. [Online]. Available: https://www.ptgrey.com/grasshopper3-usb3-vision-cameras

[82] Schott, "Kl 1600 led," 2018. [Online]. Available: https://www.us.schott.com/lightingimaging/english/microscopy/products/kl/1600led.html

[83] Micronit, "Sideconnect starter kit 15 mm x 30 mm," 2018. [Online]. Available: https://store.micronit.com/chipholders/sideconnect-starter-kit-15-mm-x-30-mm

[84] Texas instruments, "Opa 2107," 2018. [Online]. Available: http://www.ti.com/product/OPA2107

[85] Biologic, “Sp-300,” 2018. [Online]. Available: http://www.bio-logic.net/en/products/multichannel-conductivity/sp-300-potentiostat-galvanostat/

[86] Mathworks, “Matlab r2016b,” 2016. [Online]. Available: https://nl.mathworks.com/products/matlab.html

[87] W. Rasband, “Imagej,” 2018. [Online]. Available: https://imagej.nih.gov/ij/index.html

[88] Biologic, “Ec-lab software,” 2018. [Online]. Available: http://www.bio-logic.net/softwares/ec-lab-software/

[89] D. L. Sengupta and V. V. Liepa, “Appendix c: Constitutive relations,” *Applied electromagnetics and electromagnetic compatibility*, 2006. [Online]. Available: https://onlinelibrary.wiley.com/doi/pdf/10.1002/0471746231.app3

[90] J. L. Rosenholtz and D. T. Smith, “The dielectric constant of mineral powders,” *Mineralogical Society of America*, 1936. [Online]. Available: http://www.minsocam.org/ammin/AM21/AM21_115.pdf

[91] P. C. Fannin, C. N. Marin, I. Malaescu, and N. Stefu, “Microwave dielectric properties of magnetite colloidal particles in magnetic fluids,” *Journal of Physics: Condensed Matter*, 2007. [Online]. Available: http://iopscience.iop.org/article/10.1088/0953-8984/19/3/036104

[92] I. M. Mirza, K. Ali, A. K. Sarfraz, A. Ali, and A. Haq, “A study of dielectric, optical and magnetic characteristics of maghemite nanocrystallites,” *Materials Chemistry and Physics*, 2015. [Online]. Available: https://www.sciencedirect.com/science/article/pii/S025405841530300X

Appendix A

Simulation results Tao Sun model: particle between electrodes

A.1 Optimization of electrode length and width

In this appendix the simulation results are shown for the impedance of the system using the Tao Sun model [8]. The length and width of the system are varied while all other parameters remain constant. In the simulations FCC particles with a radius of 40 micron are used for four stages of metal loading. The channel height which is the spacing between the electrodes is equal to 230 micron. The used fluid is anisole with a dielectric constant of 4.33 and the resistivity is 10^{13} [$\Omega \cdot$ m] [49], [50].

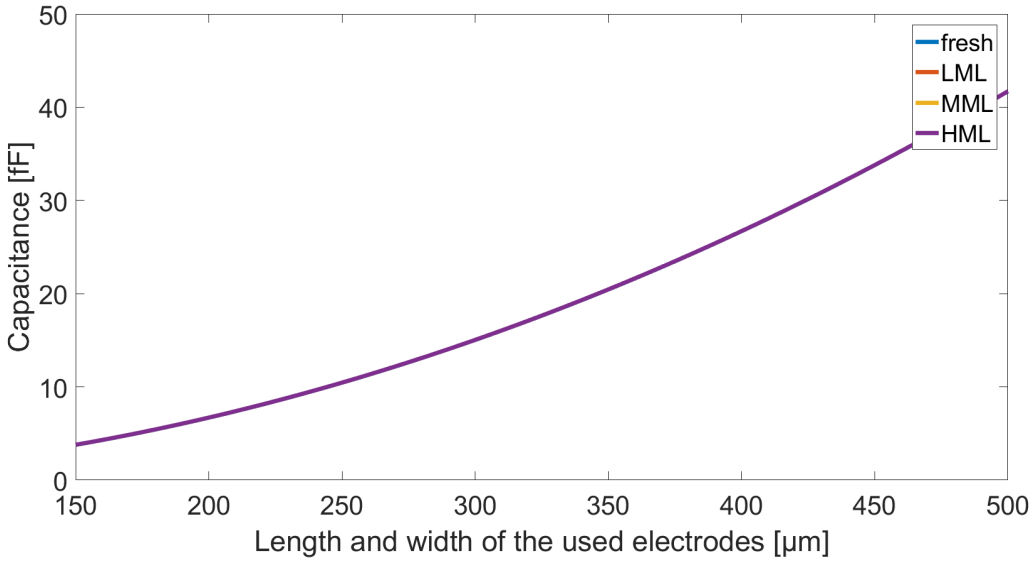

Fig. A.1: System capacitance versus the width and length of the electrodes. The impedance is plotted for the four stages of metal loading. However, as the impedance difference is small, the lines overlap.

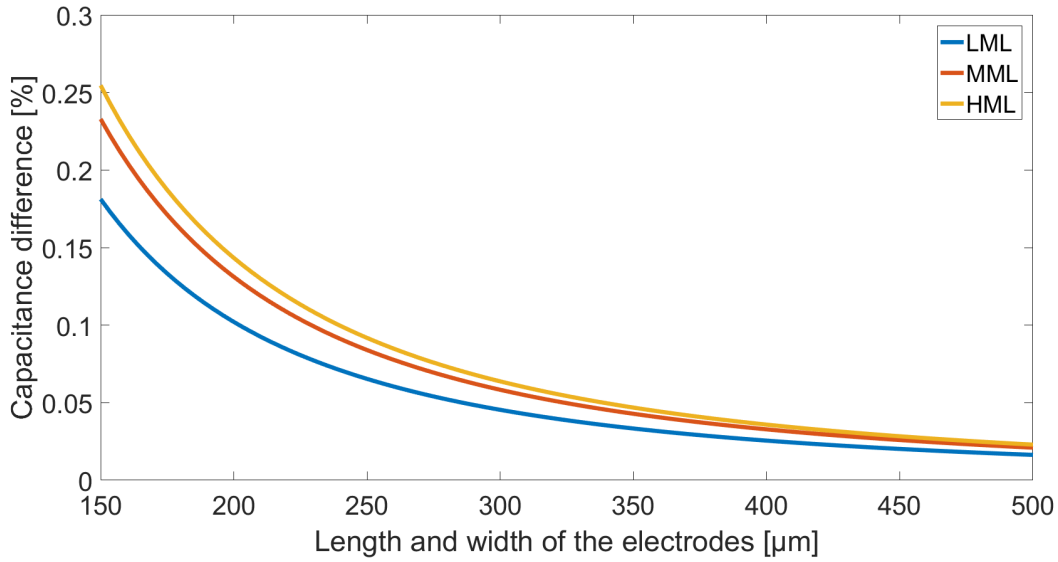

Fig. A.2: The relative change in capacitance between particles at which metal has accumulated (LML, MML or HML) and fresh particles without metal loading, versus the width and length of the electrodes.

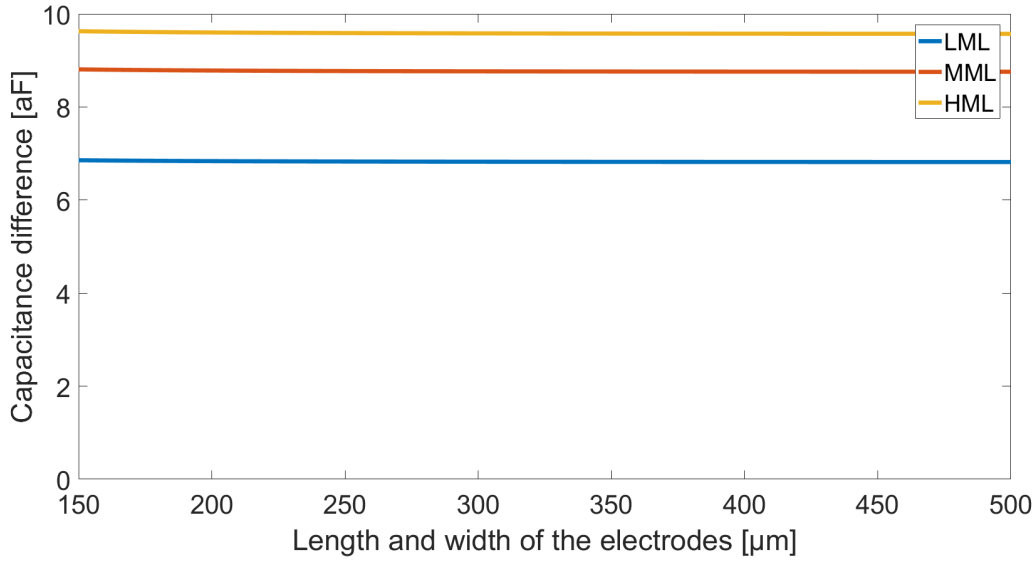

Fig. A.3: The absolute change in capacitance between particles at which metal has accumulated (LML, MML or HML) and fresh particles without metal loading, versus the width and length of the electrodes.

A.2 Optimization of electrode spacing

In this appendix the simulation results are shown for the impedance of the system using the Tao Sun model [8]. The electrode spacing of the system is varied while all other parameters remain constant. In the simulations FCC particles with a radius of 40 micron are used for four stages of metal loading. The channel length and width which is the spacing between the electrodes are equal to 300 micron. The used fluid is anisole with a dielectric constant of 4.33 and the resistivity is 10^{13} [$\Omega \cdot$ m] [49], [50].

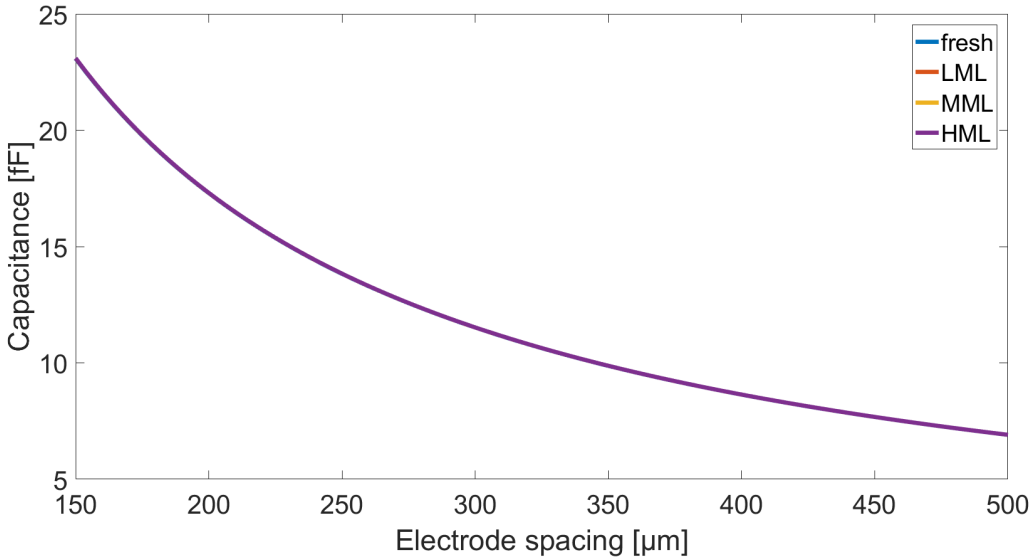

Fig. A.4: System capacitance versus the electrode spacing. The impedance is plotted for the four stages of metal loading. However, as the impedance difference is small, the lines overlap.

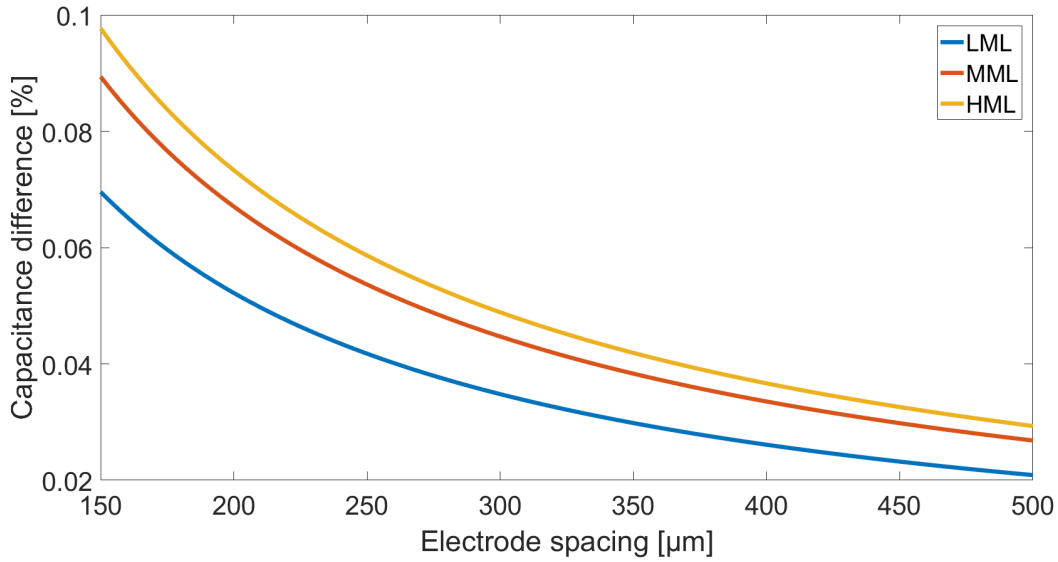

Fig. A.5: The relative change in capacitance between particles at which metal has accumulated (LML, MML or HML) and fresh particles without metal loading plotted, versus the electrode spacing.

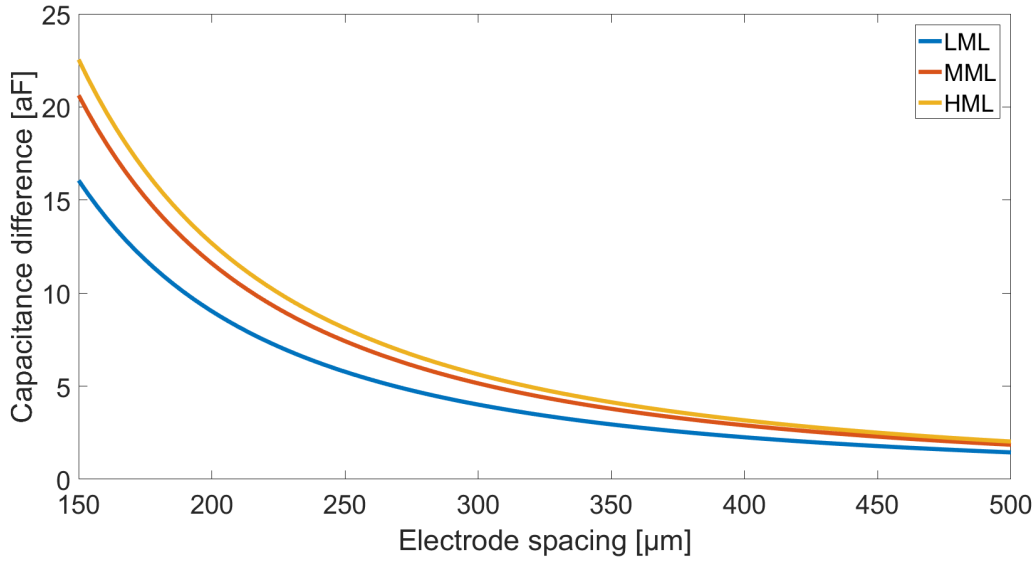

Fig. A.6: The absolute change in capacitance between particles at which metal has accumulated (LML, MML or HML) and fresh particles without metal loading, versus the electrode spacing.

A.3 Optimization of fluid dielectrics

In this appendix the simulation results are shown for the impedance of the system using the Tao Sun model [8]. The dielectric constant of the fluid is varied while all other parameters remain constant. In the simulations FCC particles with a radius of 40 micron are used for four stages of metal loading. The channel height which is the spacing between the electrodes is equal to 230 micron, the channel length and width is equal to 300 micron. The used fluid has a resistivity is 10^{13} [$\Omega \cdot$ m] [49].

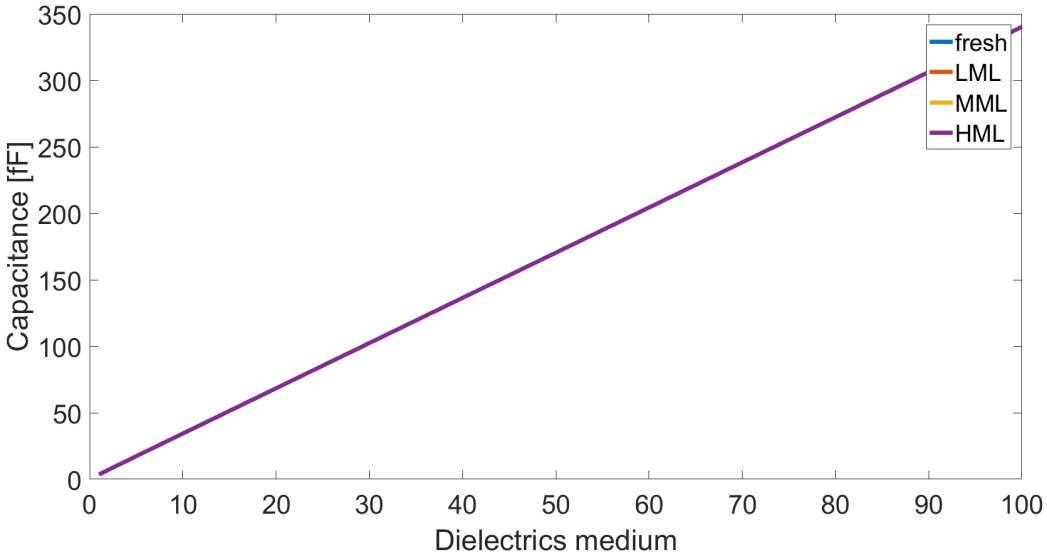

Fig. A.7: System capacitance versus the fluid dielectric constant. The impedance is plotted for the four stages of metal loading. However, as the impedance difference is small, the lines overlap

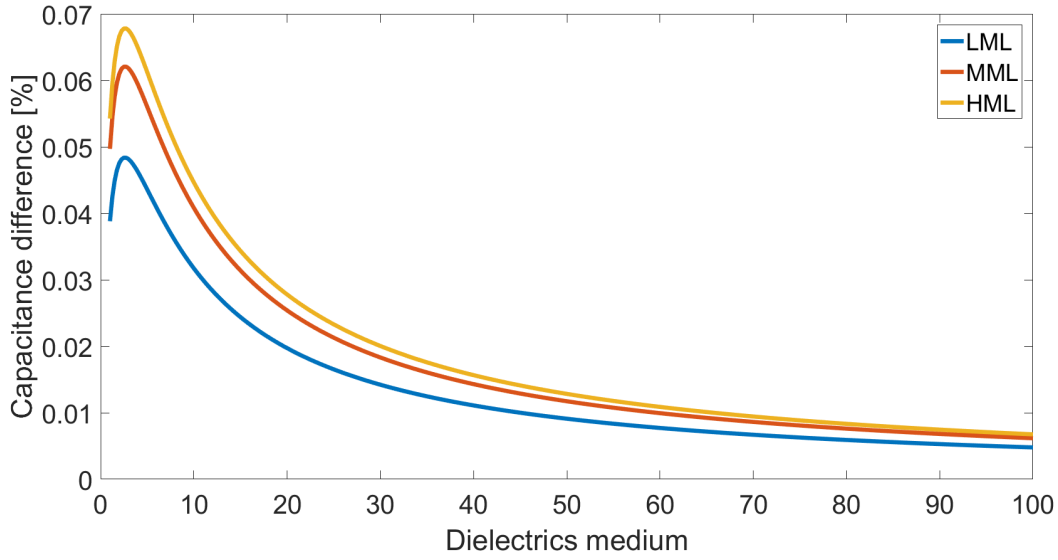

Fig. A.8: The relative change in capacitance between FCC particles at which metal has accumulated (LML, MML or HML) and fresh particles without metal loading plotted, versus the fluid dielectric constant

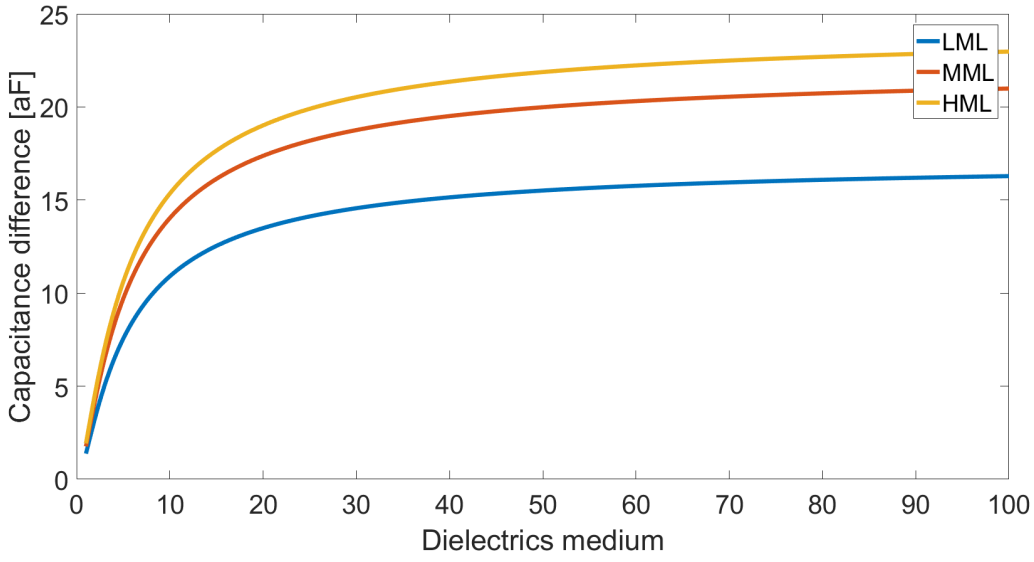

Fig. A.9: The absolute change in capacitance between particles at which metal has accumulated (LML, MML or HML) and fresh particles without metal loading, versus the fluid dielectric constant.

A.4 Particle size variation

In this appendix the simulation results are shown for the impedance of the system using the Tao Sun model [8]. The particle radius is varied between 30 and 50 micron while four different fluid dielectric constants are used. All other parameters remain constant. In this simulation only the effect on fresh particles is shown, the effect on particles with metal loading is similar to this. The channel height which is the spacing between the electrodes is equal to 230 micron, the channel length and width is equal to 300 micron. The used fluid is anisole with a dielectric constant of 4.33 and the resistivity is 10^{13} [$\Omega \cdot$ m] [49], [50]. Fig. A.11, A.12 and A.13 show how much the capacitance differs whenever the size of the particle is different from the expected value of 40 micron.

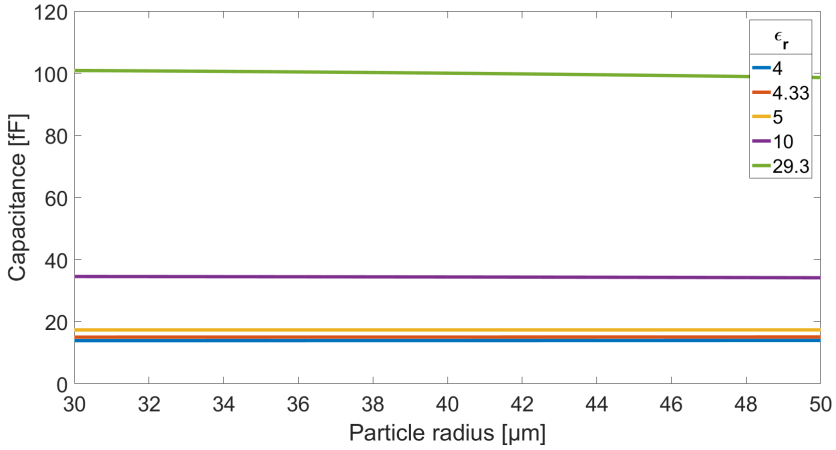

Fig. A.10: Capacitance of the system versus the radius of a fresh FCC particle, plotted for 4 different values for the dielectric constant

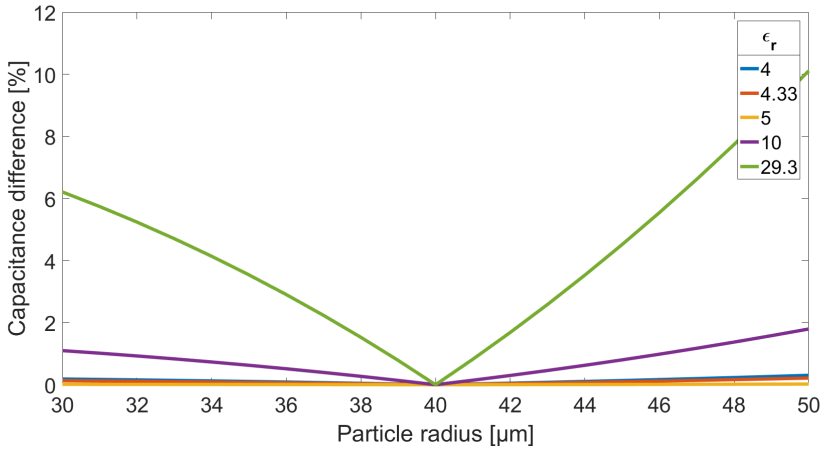

Fig. A.11: Difference (in percentage) between the capacitance of the system for a FCC particle with radius between 30 and 50 micron and a particle of 40 micron.

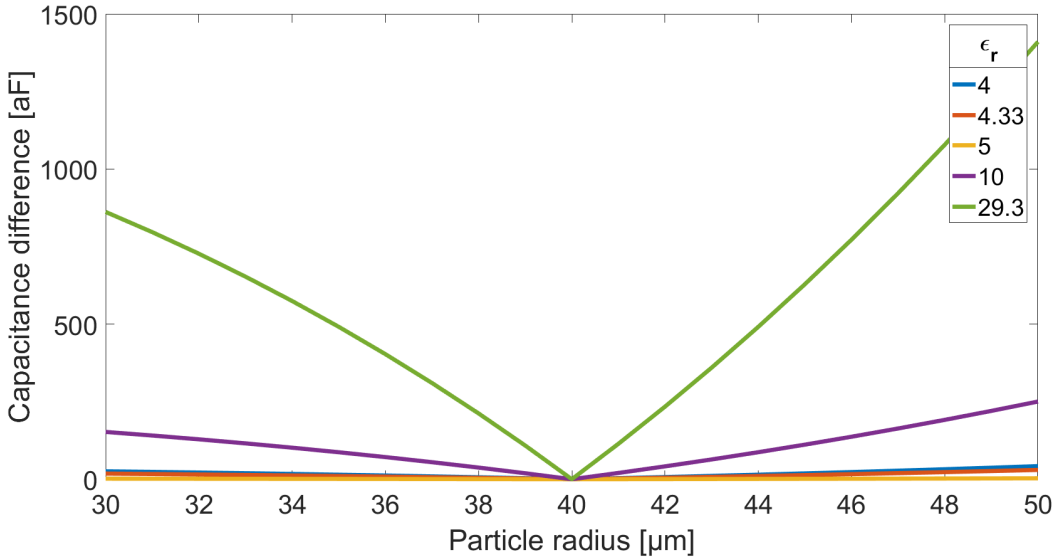

Fig. A.12: Difference (in Farad) between the capacitance of the system for a FCC particle with radius between 30 and 50 micron and a particle of 40 micron.

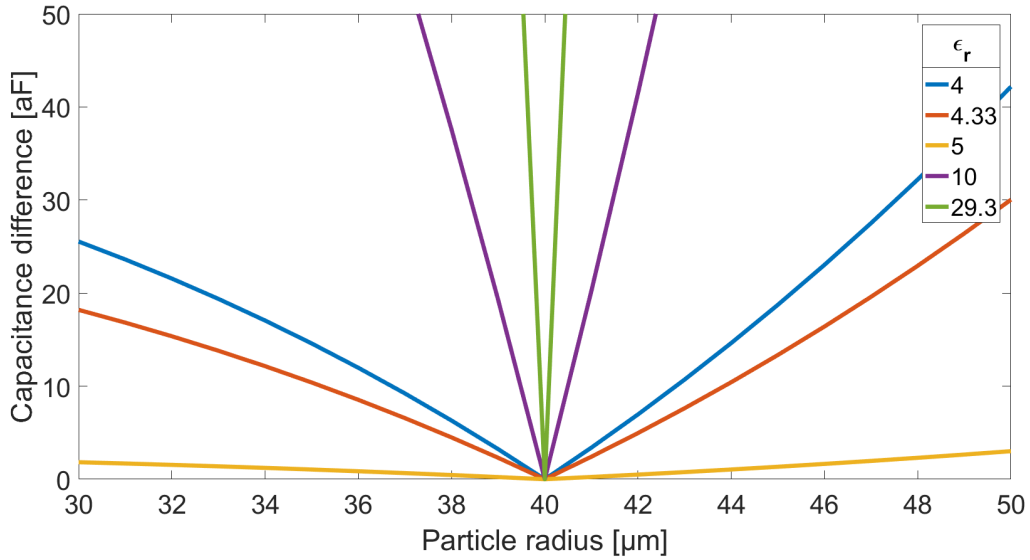

Fig. A.13: Zoomed: difference (in Farad) between the capacitance of the system for a FCC particle with radius between 30 and 50 micron and a particle of 40 micron.

Appendix B

Process flow

In this appendix the process flow for the manufacturing of the microfluidic chip is included.

Tab. B.1: General information process flow microfluidic chip.

Name of process flow	Glass microfluidic chip with electrodes
Platform	Fluidics
Creation date	2018-03-19
Personal information	
User name	Hendrix, J.M.
Chair	Bios
Function	Masterstudent
Project	FCC impedance sensing
Name of supervisor	Miguel Solsona
Process planning	
Process start	2018-03-19
Process end	2018-08-31

The standard cleaning process required between some steps consist of the following steps in WB16:

1. HNO3 beaker 1 (5 min)
2. HNO3 beaker 2 (5 min)
3. Quick dump rinse
4. Dry spinning

ILP: In-line Processing	MFP: Metal-free Processing	UCP: Ultra Clean Processing	Removal of Residues

WAFER A (5 bondpads/bottom)

Step	Level	Process/Basic flow		User comments
1		**Substrate Borofloat BF33** (#subs116)	NL-CLR-Cupboard • Type: Borofloat33 • C.T.E.: 3.25 X 10^{-6} K^{-1} • Tglass: 525°C • T anneal: 560°C • Tsoftening: 820 °C • Diameter: 100.0 mm ± 0.5 mm • Thickness: 1.1mm • Etch rate HF 25%: 1µm/min • Etch rate BHF (1:7): 20-25 nm/min • Etchrate HF 1%: 8.6 nm/min • Smooth side: second flat on the left side	Wafer A
1b		**Wafer cleaning with HNO3** • **WB 16 HNO3 beaker 1: 5 min** • **QDR** • **WB17 KOH dip** • **WB16 QDR** • **HNO3 beaker 1 (5min)** • **HNO3 beaker 2 (5min)** • **QDR** • **Dry Spinning standard program**		
litho1801: Lithography of Olin Oir 907-17 (positive resist - ILP)				
2	ILP	**Priming HMDS** (#litho600)	**OPTION 1 Liquid HMDS priming** **NL-CLR-WB21/22 Hotplate** Purpose: dehydration bake Settings: • Temperature: 120°C • Time: 5min After the dehydration bake, perform the liquid priming with minimum delay! **NL-CLR-WB21 Primus SB15 Spinner** Primer: HexaMethylDiSilazane (HMDS) Settings: • Spin mode: static • Spin speed: 4000rmp • Spin time: 30s **OPTION 2 Vapor HMDS priming**	

			NL-CLR-WB28 Lab-line Duo-Vac Oven Settings: • Temperature: 150°C • Pressure: 25 inHg • Dehydratation bake: 2 min • HMDS priming: 5 min CAUTION: let the substrates cool down before handling with your tweezer! **Spin the wafer first with adhesive layer(**Primer: HexaMethylDiSilazane (HMDS)**), no baking needed (only after olin), use wb21**
3	ILP	**Coating of Olin OiR 907-17** (#litho101)	NL-CLR-WB21 Coating: Primus spinner • Olin OiR 907-17 • Spin program: 4000 (4000rpm, 30sec)
4	ILP	**Prebake of Olin OiR 907-17** (#litho003)	NL-CLR-WB21 Prebake: Hotplate • Temperature: 95°C • Time: 90s
5	ILP	**Alignment & exposure of Olin OiR 907-17** (#litho301)	NL-CLR- EV620 Electronic Vision Group EV620 Mask Aligner • Hg-lamp: 12 mW/cm ^{2} • Exposure time: 4sec
6	ILP	**After exposure bake of Olin OiR resists** (#litho005)	NL-CLR-WB21 After exposure bake: Hotplate • Temperature: 120°C • Time: 60s
7	ILP	**Development of Olin OiR resists** (#litho200)	**NL-CLR-WB21** Development: OPD4262 • Beaker 1: 30sec • Beaker 2: 15-30sec
8	ILP	**Quick Dump Rinse (QDR)** (#rinse001)	**NL-CLR-Wetbenches** Purpose: removal of traces of chemical agents. Recipe 1 Quick dump rinsing (QDR) Recipe 2 Cascade rinsing for fragile wafers Rinse until message ´End of rinsing process´ is shown on the touchscreen of the QDR, else repeat the rinsing process.
9	ILP	**Substrate drying** (#dry001)	**NL-CLR-WBs (ILP)** Single substrate drying: 1. Use the single-wafer spinner Settings: 2500 rpm, 60 sec (including 45 sec nitrogen purge) 2. Use the nitrogen gun (fragile wafers or small samples)
10	ILP	**Postbake of Olin OiR resists** (#litho008)	NL-CLR-WB21 Postbake: Hotplate • Temperature: 120°C • Time: 10min

11	ILP	**Inspection by Optical Microscopy** (#metro101)	**NL-CLR-Nikon Microscope** Use the Nikon microscope for inspection.
		Etching of glass	
	ILP	**WB10** 6 minutes BHF solution QDR Spinning	
		film1502: Sputtering of Platinum (tcoathy)	
12	ILP	**Sputtering of Pt** (#film118)	NL-CLR-nr. 37 / tcoathy Pt Target (gun #: see mis logbook) • use Ar flow to adjust sputter pressure • base pressure: < 1.0 e-6mbar • sputter pressure: 6.6 e-3mbar • power: 200W depositionrate = 22-27 nm/min • 1 layer tantalum (10nm) • then layer of Platinum (100-150nm)
		litho1500: Lift-Off with postive resists (WB11)	
13	ILP	**Lift-Off** **(#**litho500)	NL-CLR-WB11 Purpose: removal of resist and excess metal from the surface of the substrate by ultrasonication in Acetone. Use the ultrasonic bath in WB11. • Beaker 1: Acetone • Time = 10 min **Single wafer processing:** Spray the wafer with Acetone for 30 sec and immediately spray with isopropanol (IPA) for 30 sec. **Batch wafer processing:** • Beaker 2: Acetone • Time = 10 min • Beaker 3: Isopropanol • Time = 10 min Approach 2: • First overnight in a closet basket of aceton • Spray the remainders with aceton • Put in a beaker of aceton • Put beaker in ultrasonic bath for 2 min • Spray with isopropanol

- Dry spinning

14 ILP **Substrate drying** (#dry001)

NL-CLR-WBs (ILP)

Single substrate drying:
1. Use the single-wafer spinner
   Settings: 2500 rpm, 60 sec (including 45 sec nitrogen purge)
2. Use the nitrogen gun (fragile wafers or small samples)

litho1832: Lithography SU-8 100 (negative resist - ILP)

15 ILP **Dehydration bake for SU-8** (#lith050)

NL-CLR-WB24
Dehydration bake on hotplate
• Temperature: 120°C
• Time: 10min

Do this same day as bonding

Not necessary, but cleaning the wafers might

16 ILP **Coating SU-8 100 (Delta20)** (#lith125)

NL-CLR-WB24
SüssMicroTec Spinner Delta 20
Resist: MicroChem NANO™ SU-8 100

SU-8 100 spin speed characteristics:

First cover the surrounding of the spinner with aluminum foil, to capture the removed SU-8

Make sure this foil does not tough the wafer, align the wafer with header thingy, then apply vacuum

See list on wb24 for thicknesses
Tried first wafer
First program 10 (Su-8 100)
First bake:

- 5 min 50 degrees
- 10 min 65 degrees
- 120 min 95 degrees
- **Cool down to at least 35 degrees**

Then program 7 (Su-8 50)
First bake:

- 5 min 50 degrees
- 5 min 65 degrees
- 20 min 95 degrees
- **Cool down to at least 35 degrees**

Clean equipment with aceton

Spin Program	Spin Speed (rpm)	Thickness (µm)
8	1000	380
9	1500	230
10	2000	200

			11	2500	150
			12	3000	120
			13	3500	100
			14	4000	85
17	ILP	**Prebake SU-8 100** (#lith126)	NL-CLR-WB24 Hotplate xx For spin programs 8 - 10: • 25°C • 10min @ 50°C • 30min @ 65°C • 210min @ 95°C • 5°C/5min ramp down to 25°C For spin programs 11- 14: • 25°C • 10min @ 50°C • 30min @ 65°C • 120min @ 95°C • 5°C/5min ramp down to 25°C		Look at times to previous point
18	ILP	**Alignment & Exposure SU-8 100** (#lith127)	NL-CLR-EV620 mask aligners Use contact mode		
19	ILP	**Post exposure bake SU-8 100** (#lith128)	NL-CLR-WB24/hotplates For spin programs 8 - 10: • 25°C • 10min @ 50°C • 10min @ 65°C • 20min @ 75°C • 5°C/5min ramp down to 25°C For spin programs 11- 14: • 25°C • 10min @ 50°C • 10min @ 65°C • 35min @ 75°C • 5°C/5min ramp down to 25°C		
20	ILP	**Development SU-8 100** (#lith129)	NL-CLR-WB24 • Developer: PGMEA (RER600, ARCH Chemicals) • Time: ~3:30min with spray-gun **• Rinse with RER600 (above spinner)** **• Rinse with IPA (above rest of wetbench)** • Spin dry • Check result and perform extra cycles if not complete		

Spin program	**Exposure time [s]**
8	120
9	75
10	67
11	60
12	45
13	37
14	37

WAFER B (4 bondpads/top)

Step	Level	Process/Basic flow		User comments
1		**Substrate Borofloat BF33** (#subs116)	NL-CLR-Cupboard • Type: Borofloat33 • C.T.E.: 3.25 X 10^{-6} K^{-1} • Tglass: 525°C • T anneal: 560°C • Tsoftening: 820 °C • Diameter: 100.0 mm ± 0.5 mm • Thickness: 1.1mm • Etch rate HF 25%: 1µm/min • Etch rate BHF (1:7): 20-25 nm/min • Etchrate HF 1%: 8.6 nm/min • Smooth side: second flat on the left side	Wafer A
1b		**Wafer cleaning with HNO3** • **WB 16 HNO3 beaker 1: 5 min** • **QDR** • **WB17 KOH dip** • **WB16 QDR** • **HNO3 beaker 1 (5min)** • **HNO3 beaker 2 (5min)** • **QDR** • **Dry Spinning standard program**		
litho1801: Lithography of Olin Oir 907-17 (positive resist - ILP)				
2	ILP	**Priming HMDS** (#litho600)	**OPTION 1 Liquid HMDS priming** **NL-CLR-WB21/22 Hotplate** Purpose: dehydration bake Settings: • Temperature: 120°C • Time: 5min After the dehydration bake, perform the liquid priming with minimum delay! **NL-CLR-WB21 Primus SB15 Spinner** Primer: HexaMethylDiSilazane (HMDS) Settings: • Spin mode: static • Spin speed: 4000rmp • Spin time: 30s **OPTION 2 Vapor HMDS priming** **NL-CLR-WB28 Lab-line Duo-Vac Oven** Settings:	

			• Temperature: 150°C • Pressure: 25 inHg • Dehydratation bake: 2 min • HMDS priming: 5 min CAUTION: let the substrates cool down before handling with your tweezer! **Spin the wafer first with adhesive layer(**Primer: HexaMethylDiSilazane (HMDS)**), no baking needed, use wb21**
3	ILP	**Coating of Olin OiR 907-17** (#litho101)	NL-CLR-WB21 Coating: Primus spinner • Olin OiR 907-17 • Spin program: 4000 (4000rpm, 30sec)
4	ILP	**Prebake of Olin OiR 907-17** (#litho003)	NL-CLR-WB21 Prebake: Hotplate • Temperature: 95°C • Time: 90s
5	ILP	**Alignment & exposure of Olin OiR 907-17** (#litho301)	NL-CLR- EV620 Electronic Vision Group EV620 Mask Aligner • Hg-lamp: 12 mW/cm ^{2} • Exposure time: 4sec
6	ILP	**After exposure bake of Olin OiR resists** (#litho005)	NL-CLR-WB21 After exposure bake: Hotplate • Temperature: 120°C • Time: 60s
7	ILP	**Development of Olin OiR resists** (#litho200)	**NL-CLR-WB21** Development: OPD4262 • Beaker 1: 30sec • Beaker 2: 15-30sec
8	ILP	**Quick Dump Rinse (QDR)** (#rinse001)	**NL-CLR-Wetbenches** Purpose: removal of traces of chemical agents. Recipe 1 Quick dump rinsing (QDR) Recipe 2 Cascade rinsing for fragile wafers Rinse until message ´End of rinsing process´ is shown on the touchscreen of the QDR, else repeat the rinsing process.
9	ILP	**Substrate drying** (#dry001)	**NL-CLR-WBs (ILP)** Single substrate drying: 1. Use the single-wafer spinner Settings: 2500 rpm, 60 sec (including 45 sec nitrogen purge) 2. Use the nitrogen gun (fragile wafers or small samples)
10	ILP	**Postbake of Olin OiR resists** (#litho008)	NL-CLR-WB21 Postbake: Hotplate • Temperature: 120°C • Time: 10min

11	ILP	**Inspection by Optical Microscopy** (#metro101)	**NL-CLR-Nikon Microscope** Use the Nikon microscope for inspection.
		Etching of glass	
	ILP	**WB10** 6 minutes BHF solution QDR Spinning	
		film1502: Sputtering of Platinum (tcoathy)	
12	ILP	**Sputtering of Pt** (#film118)	NL-CLR-nr. 37 / tcoathy Pt Target (gun #: see mis logbook) • use Ar flow to adjust sputter pressure • base pressure: < 1.0 e-6mbar • sputter pressure: 6.6 e-3mbar • power: 200W depositionrate = 22-27 nm/min • 1 layer tantalum (10nm) • then layer of Platinum (100-150nm)
		litho1500: Lift-Off with postive resists (WB11)	
13	ILP	**Lift-Off** **(#**litho500)	NL-CLR-WB11 Purpose: removal of resist and excess metal from the surface of the substrate by ultrasonication in Acetone. Use the ultrasonic bath in WB11. • Beaker 1: Acetone • Time = 10 min **Single wafer processing:** Spray the wafer with Acetone for 30 sec and immediately spray with isopropanol (IPA) for 30 sec. **Batch wafer processing:** • Beaker 2: Acetone • Time = 10 min • Beaker 3: Isopropanol • Time = 10 min Approach 2: • First overnight in a closet basket of aceton • Spray the remainders with aceton • Put in a beaker of aceton • Put beaker in ultrasonic bath for 2 min • Spray with isopropanol

			• Dry spinning
14	ILP	**Substrate drying** (#dry001)	**NL-CLR-WBs (ILP)** Single substrate drying: 1. Use the single-wafer spinner Settings: 2500 rpm, 60 sec (including 45 sec nitrogen purge) 2. Use the nitrogen gun (fragile wafers or small samples)

WAFER A + B

Direct Bonding:

program.: Man An Bond - Crosshair - Flags before Wec
Reduce the 'Wec' to almost zero, otherwise the wafers may stick already during the loading. If necessary, allow focussing again.

- carefully unload the wafers stack and put it on a black flat surface (in the Bios cabinet; shelf Jan)
- if the prebond is not perfect: rub with a synthetic tweezer, to remove residual air. This airgap shows like a white or colored area; the prebonded area is transparent.
- a tiny droplet of water may help to support the prebond, but first try without

align on either 1-3 or 3-3 (top and bottom wafer alignment) (below the big 4)

Bonding:
oven:
program:

- 120 degrees
- 4000N
- ~20 min

Dicing:
Use the transparent dicing foil (100 µm thick) for glass dicing. The blue one is only 70 µm thick and this result in a sharp edge at the bottom of the diced edge.

- laminate the wafer onto the transparent dicing foil by rolling out a piece of foil over the wafer
- Use the TC300 blade (300 µm thick)
- Each chip is 2 cm by 1.5 cm

Appendix C

Mask layout

The combined layout of the three masks is shown in Fig. C.1. The layout of the individual layers is shown in Fig. C.2, C.3 and C.4.

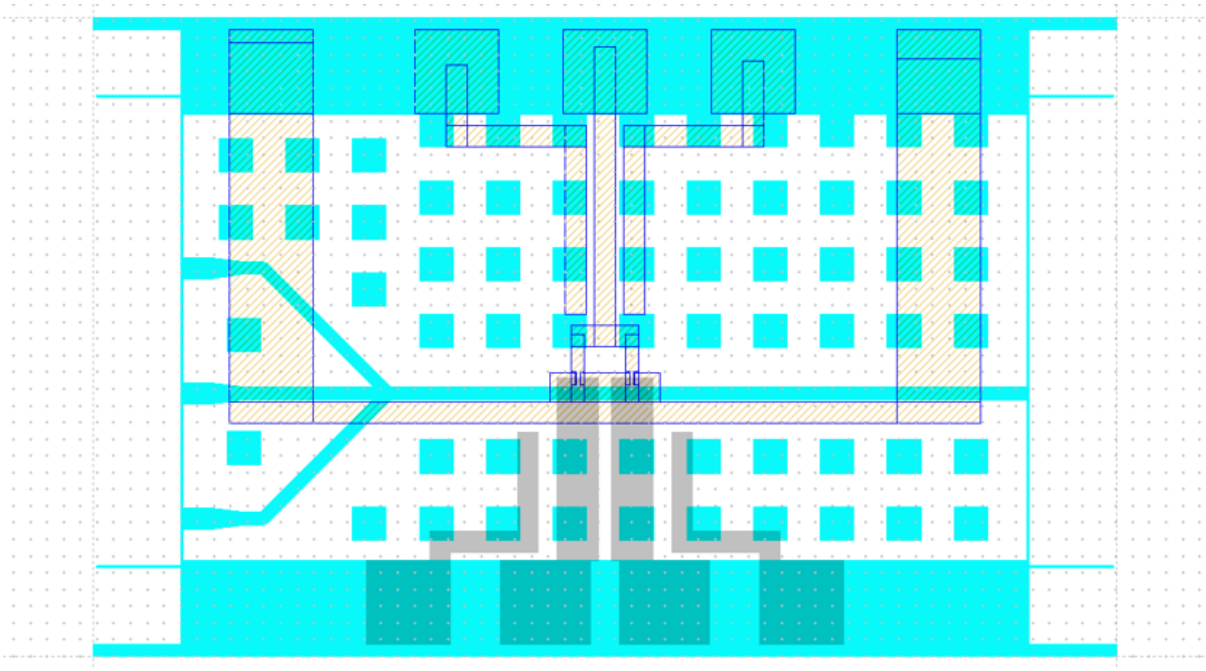

Fig. C.1: Combined layout of the three masks that are used. Showing in cyan the SU-8 channel layer, in grey the bottom electrodes and in yellow the top electrodes.

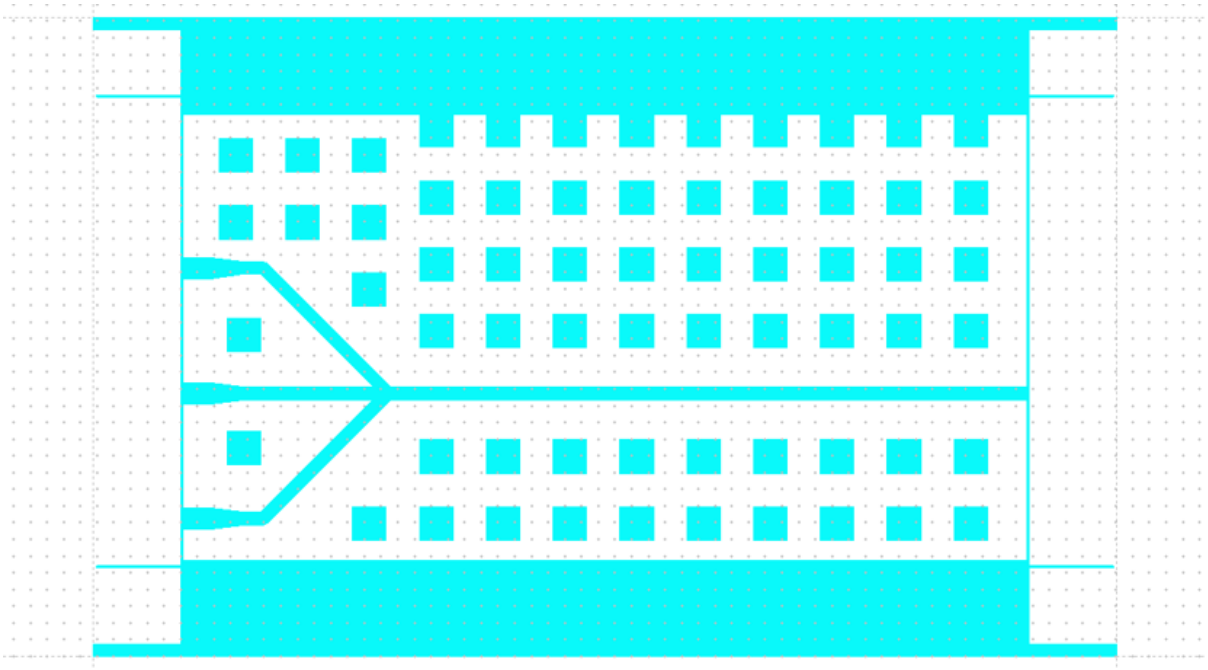

Fig. C.2: Mask layout of the SU-8 layer showing the channel structure and including blocks required to avoid thermal cracking

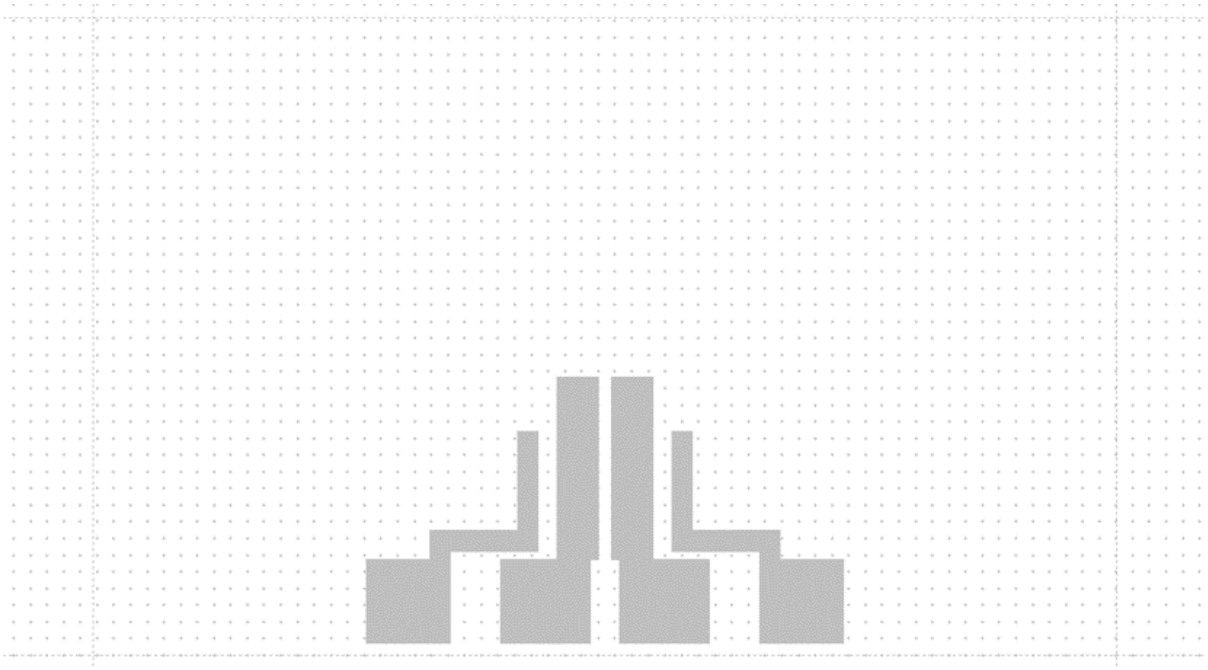

Fig. C.3: Mask layout of the bottom wafer electrodes, showing the two inputs which are driven by out-of-phase signals and two shielding electrodes.

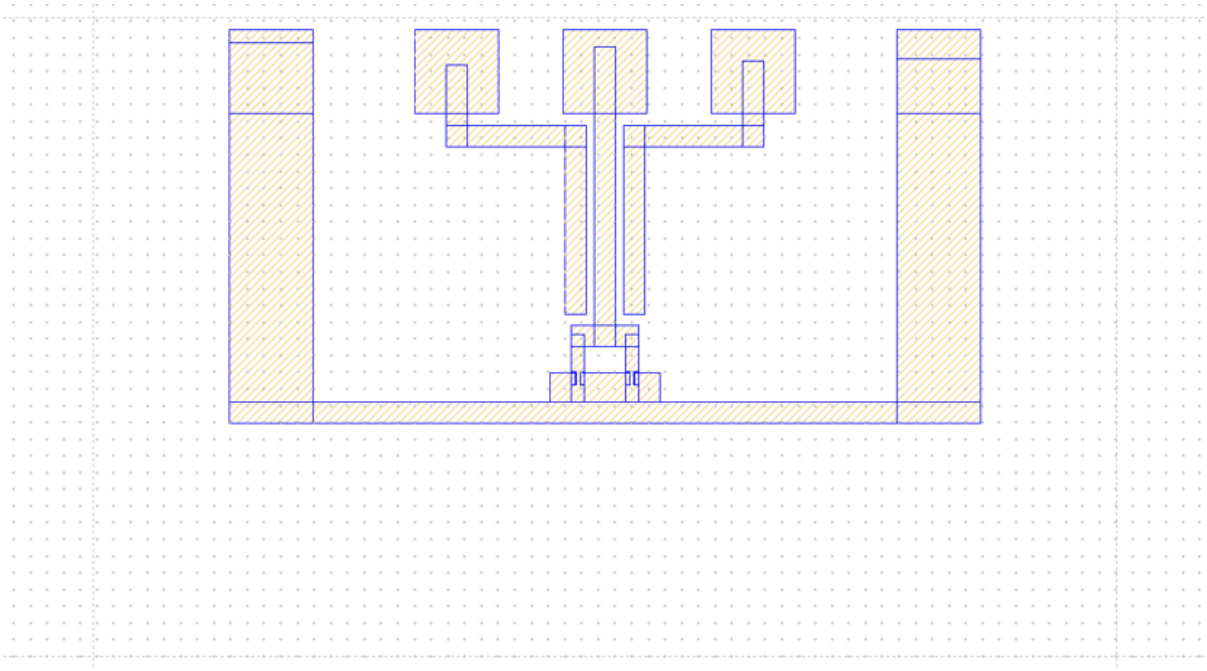

Fig. C.4: Mask layout of the top wafer electrodes, showing the single ouput electrode and some shielding electrodes.

Appendix D

Particle influence on electric field lines

In this appendix the influence of the difference in dielectric constant of the particle and medium on the electric field lines in between the electrodes is visualized. Situations are shown for four different positions and two scenarios: where the particle has a higher dielectric constant than the medium and vice versa. The particle has a higher dielectric constant compared to the medium in Fig. D.1 and the particle has a lower dielectric constant compared to the medium in Fig. D.2. The figures show exaggerations of the change in field-lines from reality as this will visualize more clearly what is happening.

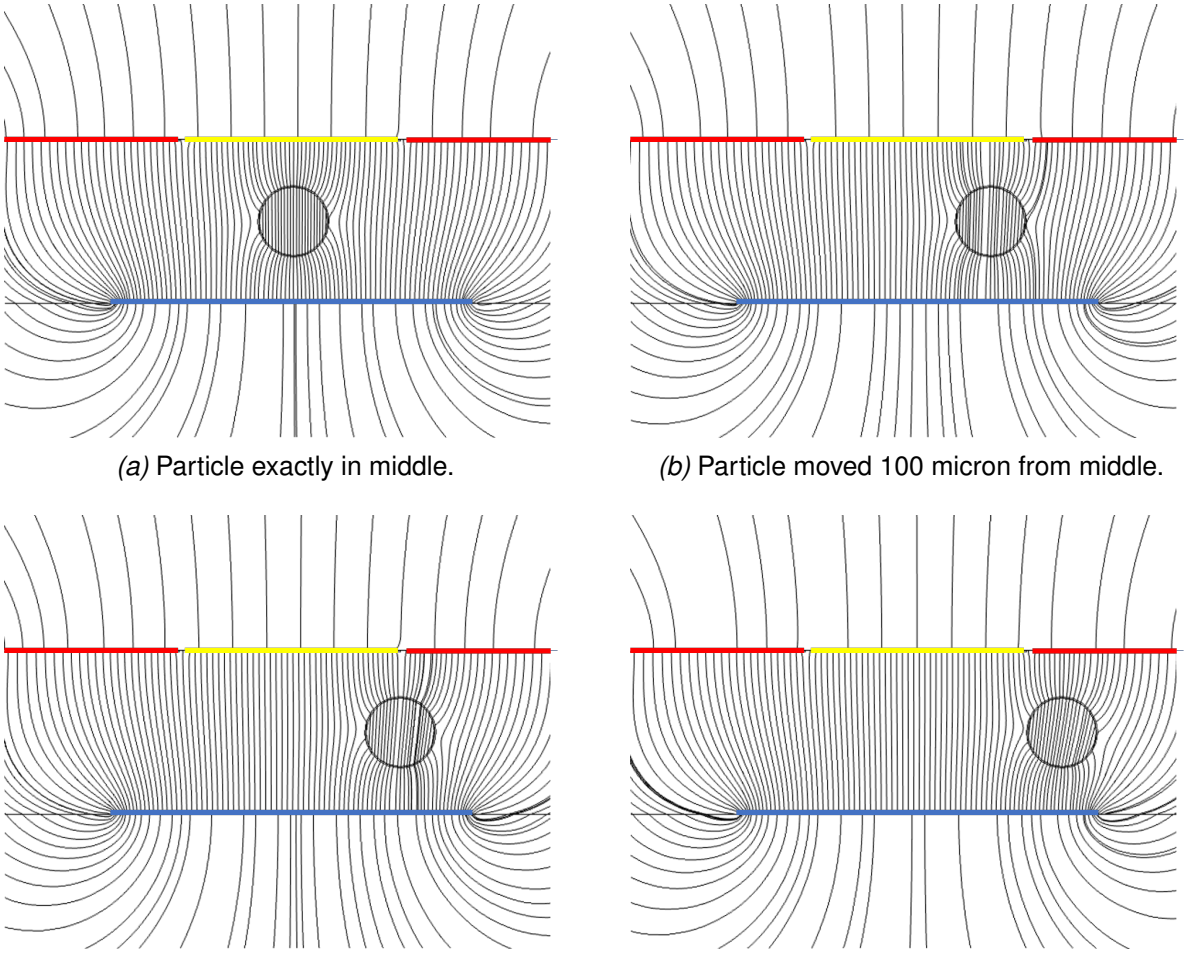

(a) Particle exactly in middle.

(b) Particle moved 100 micron from middle.

(c) Particle moved 150 micron from middle.

(d) Particle moved 200 micron from middle.

Fig. D.1: Influence of particle on the electric field lines within the channel. In this image the difference between the dielectric constant of the particle and medium is exaggerated by using a particle dielectric constant of 30 and the medium dielectric constant of 4.33. In the figures, the yellow line represent the top electrode, the blue line the bottom electrode and the red lines the ground electrodes.

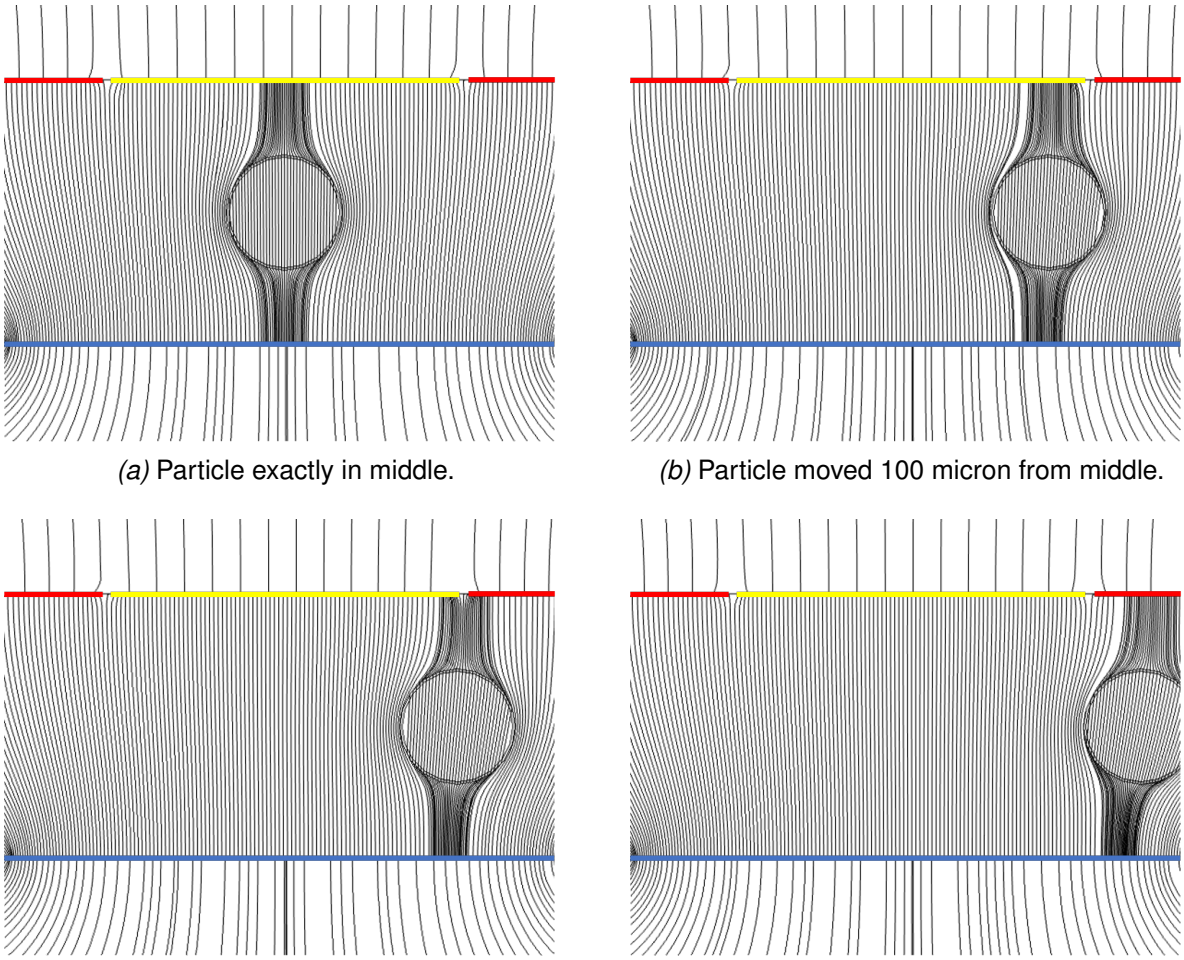

(a) Particle exactly in middle.

(b) Particle moved 100 micron from middle.

(c) Particle moved 150 micron from middle.

(d) Particle moved 200 micron from middle.

Fig. D.2: Influence of particle on the electric field lines within the channel. In this image the difference between the dielectric constant of the particle and medium is exaggerated by using a particle dielectric constant of 4.33 and the medium dielectric constant of 30. In the figures, the yellow line represent the top electrode, the blue line the bottom electrode and the red lines the ground electrodes.